

Analytic Gaussian Covariance Matrices for Galaxy N -Point Correlation Functions

Jiamin Hou^{1*}, Robert N. Cahn², Oliver H. E. Philcox^{3,4}, and Zachary Slepian^{1,2}

¹*Department of Astronomy, University of Florida, 211 Bryant Space Science Center, Gainesville, FL 32611, USA*

²*Lawrence Berkeley National Laboratory, 1 Cyclotron Road, Berkeley, CA 94720, USA*

³*Department of Astrophysical Sciences, Princeton University, Princeton, NJ 08540, USA*

⁴*School of Natural Sciences, Institute for Advanced Study, 1 Einstein Drive, Princeton, NJ 08540, USA*

Accepted XXX. Received YYY; in original form ZZZ

ABSTRACT

We derive analytic covariance matrices for the N -Point Correlation Functions (NPCFs) of galaxies in the Gaussian limit. Our results are given for arbitrary N and projected onto the isotropic basis functions of Cahn & Slepian (2020), recently shown to facilitate efficient NPCF estimation. A numerical implementation of the 4PCF covariance is compared to the sample covariance obtained from a set of lognormal simulations, QUIJOTE dark matter halo catalogues, and MULTIDARK-PATCHY galaxy mocks, with the latter including realistic survey geometry. The analytic formalism gives reasonable predictions for the covariances estimated from mock simulations with a periodic-box geometry. Furthermore, fitting for an effective volume and number density by maximizing a likelihood based on Kullback-Leibler divergence is shown to partially compensate for the effects of a non-uniform window function.

1 INTRODUCTION

Large-scale structure (LSS) is a powerful observable with which to elucidate cosmic evolution. To characterize its spatial distribution, various summary statistics have been proposed, of which the most prominent are the two-point statistics, *i.e.* the 2-Point Correlation Function (2PCF) and its Fourier-space counterpart, the power spectrum (e.g., BOSS Collaboration et al. 2017; eBOSS Collaboration et al. 2021).

Although two-point statistics fully capture information in the early Universe, assuming a standard inflationary model with adiabatic perturbations, gravitational evolution induces non-linearities in the LSS at late times, spreading information into higher-order statistics. Furthermore, different mechanisms during inflation can generate distinctive non-Gaussian signatures (Kofman 1991; Linde & Mukhanov 1997; Komatsu et al. 2003; Chen et al. 2007; Chen 2010). These two effects justify pushing beyond the power spectrum or 2PCF. Examples include the 3-Point Correlation Function (3PCF; Peebles 1978; Fry & Gaztanaga 1993; Slepian & Eisenstein 2015a,b; Slepian et al. 2017; Portillo et al. 2018), the bispectrum (Scoccimarro et al. 1998; Scoccimarro 2000; Pearson & Samushia 2018), skew spectra (Dizgah et al. 2020; Schmittfull & Dizgah 2021), the marked density field (Philcox et al. 2020a; Massara et al. 2021), and the integrated bispectrum and trispectrum (Sefusatti & Scoccimarro 2005; Chiang et al. 2014). Methods such as BAO reconstruction (Eisenstein et al. 2007; Padmanabhan et al. 2009; White 2015; Schmittfull et al. 2015, 2017), forward-modeling of the galaxy density field (Jasche & Wandelt 2013; Seljak et al. 2017; Jasche & Lavaux 2019; Schmidt et al. 2019), and machine learning techniques have also been proposed as alternative but complementary approaches to summary statistics. Previous work has demonstrated that combining two- and higher-point statistics can break the degeneracy between linear bias and the amplitude of matter fluctuations, tighten constraints on standard Λ CDM parameters (Agarwal et al. 2021; Gil-Marín et al. 2017; Sugiyama et al. 2020b; Gualdi et al. 2021), and provide further insights into the neutrino mass (Ruggeri et al. 2018; de Belsunce & Senatore 2019; Chudaykin & Ivanov 2019; Hahn et al. 2020; Kamalinejad & Slepian 2020; Aviles et al. 2021) and modified gravity (Bartolo et al. 2013; Alam et al. 2020). Gravitational evolution imprints a useful shape on the N -point statistics; Samushia et al. (2021) showed that for $N = 3$ this shape can potentially provide complementary information to BAO reconstruction when it is used as standard ruler.

To infer cosmological parameters from the N -Point Correlation Functions (NPCFs) using Bayes theorem with a Gaussian likelihood, a covariance matrix is required. Usually, this is obtained by sampling independent realizations of the statistic from simulations. However this approach introduces sampling variance, which then propagates into the parameter estimates (Dodelson & Schneider 2013; Percival et al. 2014; Taylor & Joachimi 2014; Sellentin & Heavens 2016). To reduce this variance, the number of mock catalogues must be much larger than the dimension of the NPCFs; if the statistic contains many bins, the computational cost of this poses a significant challenge.

An alternative approach is to compute the covariances analytically. This has been intensively studied especially for two- and three-point statistics (Grieb et al. 2016; Li et al. 2019; Scoccimarro et al. 1999; Slepian & Eisenstein 2015a, 2018; O’Connell et al. 2016; Barreira 2019; O’Connell & Eisenstein 2019; Philcox & Eisenstein 2019; Philcox et al. 2020b; Wadekar et al. 2020; Sugiyama et al. 2020a). Recent work in Philcox et al. (2021a) developed an efficient algorithm to measure the NPCF for arbitrary N ; given the high dimensionality of the NPCFS for large N , this poses a further challenge for covariance estimation. Thus far, few studies have considered the covariance of the NPCFs with $N > 3$. To address this, we here derive an analytic expression for the NPCF covariance at arbitrary N . In order to efficiently characterise the NPCF we work with the isotropic basis functions developed in Cahn & Slepian (2020); these have rotational symmetry in 3D, and may be related to the quantum-mechanical angular momentum basis states.

An important assumption in our modeling is that the two-point statistics are the dominant contribution to the covariance, *i.e.* we ignore contributions from three- and higher-point statistics. To test this assumption, we will use simulations that include non-Gaussian effects. For the majority of this paper, we will assume the two-point statistics to be isotropic, such that the spatial distribution of the galaxy pairs is independent of the line of sight (l.o.s). In practice, a galaxy’s peculiar velocity, induced by its local gravitational environment, can give rise to redshift space distortions (RSD) and thus break isotropy. Although the main tests in this paper will be focused on the isotropic case, we will show in the Appendix an analytic expression that includes the effects of RSD, by expanding the anisotropic two-point statistics in multipoles with respect to the l.o.s. Finally, we will compare the results of our formalism to the covariance estimated from mock catalogues with a realistic survey geometry.

In §2 we briefly review the isotropic basis and its properties, before the NPCF estimator is defined in §3. In §4 we present our formalism for the theoretical covariance in the Gaussian Random Field (GRF) limit, starting with the basic elements as building blocks for constructing the Gaussian covariance, then presenting the general formalism for the NPCF covariance, and ending with explicit expressions for the case of $N = 4$. In §5 we compare our numerical implementation of the Gaussian NPCF covariance to a set of lognormal mocks, a set of halo catalogues from N-body simulations using QUIJOTE simulations and PATCHY mocks, where the latter include realistic survey geometry. We summarize our results in §6. Appendices A, B, and D provide intermediate derivation steps as well as consistency checks, Appendix C discusses the covariance contribution from the disconnected piece of the NPCF estimators, and Appendix E presents the derivation of the covariance including RSD. The code for computing the covariance of the connected 4PCFs is publicly available.¹

2 REVIEW OF THE ISOTROPIC BASIS FUNCTIONS

In this section we will provide a summary of the isotropic basis functions, including a number of important properties that will be needed later for the derivation of the theoretical covariance. Further details are presented in Cahn & Slepian (2020).

2.1 Construction of the basis function \mathcal{P}_Λ

In our notation, the isotropic functions \mathcal{P}_Λ are sums of products of n spherical harmonics $Y_{\ell m}$ multiplied by a product of Clebsch-Gordan coefficients, denoted by \mathcal{C}_M^Λ . They are constructed so as to be invariant under simultaneous rotation of all n coordinates:

$$\mathcal{P}_\Lambda(\hat{\mathbf{R}}) = \sum_{m_1 \dots m_n} \mathcal{C}_M^\Lambda Y_{\ell_1 m_1}(\hat{\mathbf{r}}_1) \cdots Y_{\ell_n m_n}(\hat{\mathbf{r}}_n), \quad (1)$$

where $\hat{\mathbf{R}}$ stands for a collection of unit vectors $\hat{\mathbf{r}}_1, \dots, \hat{\mathbf{r}}_n$. Each unit vector $\hat{\mathbf{r}}_i$ is associated with a rotation generator \mathbf{L}_i , *i.e.* the angular momentum operator. The isotropic \mathcal{P}_Λ function is an eigenfunction of each operator \mathbf{L}_i^2 with eigenvalue $\ell_i(\ell_i + 1)$ and of the operator $(\sum_{i=1}^n \mathbf{L}_i)^2$ with eigenvalue zero (see also the discussion in Philcox & Slepian 2021 for a generalization of this to D dimensions). We denote the orbital angular momenta by ℓ_i , with m_i being its projection onto the z -axis.² For $n > 3$ the combination of a given set of orbital angular momenta, ℓ_1, \dots, ℓ_n , is not unique: we need to specify intermediate orbital angular momenta. These are constructed from the primary orbital angular momenta, for example, $(\mathbf{L}_1 + \mathbf{L}_2)^2$ with eigenvalue $\ell_{12}(\ell_{12} + 1)$, and analogously for $(\mathbf{L}_1 + \mathbf{L}_2 + \mathbf{L}_3)^2$, *et cetera*. For brevity, we will hereafter call the ℓ_i ‘primary’ angular momenta and the $\ell_{12}, \ell_{123}, \dots$, ‘intermediate’ angular momenta. Further, we use Λ to indicate the collection of angular momenta $\{\ell_1, \ell_2, (\ell_{12}), \ell_3, (\ell_{123}), \dots, \ell_n\}$, with intermediate angular momenta in the brackets, and M to represent the collection of azimuthal angular momentum components $\{m_1, m_2, \dots, m_n\}$, with each $m_i = \{-\ell_i, \dots, \ell_i\}$, $m_{12} = \{-\ell_{12}, \dots, \ell_{12}\}$ and $\sum_i^{N-1} m_i = 0$. In our convention, the primary angular momenta ℓ_1, ℓ_2, \dots follow the ordering of the unit vectors: ℓ_1 corresponds to $\hat{\mathbf{r}}_1$, ℓ_2 corresponds to $\hat{\mathbf{r}}_2$, etc.

¹ See https://github.com/Moctobers/npcf_cov.git

² We adopt the language of quantum mechanics to describe the spherical harmonics.

The C_M^Λ coefficient can be expressed using Wigner 3- j symbols:

$$\begin{aligned} C_M^\Lambda &= \mathcal{E}(\Lambda) \sqrt{2\ell_{12} + 1} \times \cdots \times \sqrt{2\ell_{12\dots n-2} + 1} \\ &\times \sum_{m_{12\dots}} (-1)^\kappa \begin{pmatrix} \ell_1 & \ell_2 & \ell_{12} \\ m_1 & m_2 & -m_{12} \end{pmatrix} \begin{pmatrix} \ell_{12} & \ell_3 & \ell_{123} \\ m_{12} & m_3 & -m_{123} \end{pmatrix} \cdots \\ &\times \begin{pmatrix} \ell_{12\dots n-2} & \ell_{n-1} & \ell_n \\ m_{12\dots n-2} & m_{n-1} & m_n \end{pmatrix} \end{aligned} \quad (2)$$

where $\mathcal{E}(\Lambda) = (-1)^{\sum_i \ell_i}$ and $\kappa = \ell_{12} - m_{12} + \ell_{123} - m_{123} + \cdots + \ell_{12\dots n-2} - m_{12\dots n-2}$. If the sum of the angular momenta is even, then $\mathcal{E}(\Lambda) = 1$ and \mathcal{P}_Λ is real. Otherwise, $\mathcal{E}(\Lambda) = -1$ and \mathcal{P}_Λ is imaginary. For $n = 2$ and $n = 3$, C_M^Λ becomes:

$$C_{mm'}^{\ell\ell'} = \frac{(-1)^{\ell-m}}{\sqrt{2\ell+1}} \delta_{\ell,\ell'}^K \delta_{m,-m'}^K, \quad (3)$$

$$C_{m_1 m_2 m_3}^{\ell_1 \ell_2 \ell_3} = (-1)^{\ell_1 + \ell_2 + \ell_3} \begin{pmatrix} \ell_1 & \ell_2 & \ell_3 \\ m_1 & m_2 & m_3 \end{pmatrix}, \quad (4)$$

with $\delta_{\ell_i \ell'_i}^K$ being the Kronecker delta. The result in the second line is non-zero only when ℓ_1, ℓ_2 , and ℓ_3 satisfy the triangular inequality, $|\ell_1 - \ell_2| \leq \ell_3 \leq \ell_1 + \ell_2$. Furthermore, if any of the angular momenta are zero, the second line reduces to the first (DLMF DLMF, eq. 34.3.1).

The form of the C_M^Λ coefficient is chosen to ensure orthonormality of the isotropic basis functions. The orthonormality relation is:

$$\int d\hat{\mathbf{R}} \mathcal{P}_\Lambda(\hat{\mathbf{R}}) \mathcal{P}_{\Lambda'}^*(\hat{\mathbf{R}}) = \delta_{\ell_1 \ell'_1}^K \delta_{\ell_2 \ell'_2}^K \times \cdots \times \delta_{\ell_{12} \ell'_{12}}^K \times \cdots \times \delta_{\ell_n \ell'_n}^K. \quad (5)$$

Using this, we can expand an arbitrary isotropic function in this basis

$$\zeta(\mathbf{R}) = \sum_{\Lambda} \zeta_{\Lambda}(R) \mathcal{P}_{\Lambda}(\hat{\mathbf{R}}), \quad (6)$$

with $R \equiv \{r_1, r_2, \dots, r_n\}$ and $\mathbf{R} \equiv \{\mathbf{r}_1, \mathbf{r}_2, \dots, \mathbf{r}_n\}$. By invoking the orthonormality relation Eq. (5) we can obtain the expansion coefficient

$$\zeta_{\Lambda}(R) = \int d\hat{\mathbf{R}} \zeta(\mathbf{R}) \mathcal{P}_{\Lambda}^*(\hat{\mathbf{R}}). \quad (7)$$

In our context, $\zeta(\mathbf{R})$ is the N -point correlation function. If we expand the function in the basis \mathcal{P}_Λ , parity-even correlators will have real coefficients, but parity-odd correlators will have purely imaginary coefficients.

2.2 Useful properties

We define some useful quantities derived from the isotropic basis that will be of use later. Consider a product of n spherical harmonics. If we represent integration over the rotations, \mathcal{R} , by $d\mathcal{R}$ with $\int d\mathcal{R} = 1$ then, as shown in the previous work (Cahn & Slepian 2020), averaging over the rotation group projects out the isotropic components:

$$\int d\mathcal{R} \prod_{j=1}^n Y_{\ell_j m_j}(\mathcal{R} \hat{\mathbf{r}}_j) = \sum_{\Lambda} C_M^\Lambda \mathcal{P}_{\Lambda}(\hat{\mathbf{R}}). \quad (8)$$

The result is non-zero only if $\sum_j m_j = 0$ and the ℓ_i satisfy a generalized triangular inequality, namely that they can be combined to make a state of zero total angular momentum. The sum over Λ includes all possibilities that can be constructed from the given primary ℓ_j .

A useful consequence is the identity

$$\int d\mathcal{R} \prod_{j=1}^n \sum_{m_j} Y_{\ell_j m_j}(\mathcal{R} \hat{\mathbf{r}}_j) Y_{\ell_j m_j}^*(\hat{\mathbf{k}}_j) = \sum_{\Lambda} \sum_{m_j} C_M^\Lambda Y_{\ell_j m_j}^*(\hat{\mathbf{k}}_j) \mathcal{P}_{\Lambda}(\hat{\mathbf{R}}) = \sum_{\Lambda} \mathcal{P}_{\Lambda}(\hat{\mathbf{R}}) \mathcal{P}_{\Lambda}^*(\hat{\mathbf{K}}), \quad (9)$$

where $\hat{\mathbf{K}} = \{\hat{\mathbf{k}}_1, \dots, \hat{\mathbf{k}}_n\}$, and the sum is over all Λ that can be constructed from the primary ℓ_j .

The rotational average of a product of n spherical harmonics with a common argument is determined in a similar fashion:

$$\begin{aligned} \int d\mathcal{R} \prod_{j=1}^n Y_{\ell_j m_j}(\mathcal{R} \hat{\mathbf{r}}) &= (4\pi)^{-n/2} \prod_{j=1}^n \sqrt{2\ell_j + 1} \sum_{\Lambda} C_M^\Lambda C_{\mathbf{0}}^\Lambda \\ &= (4\pi)^{-n/2} \sum_{\Lambda} \mathcal{D}_{\Lambda}^P C_{\mathbf{0}}^\Lambda C_M^\Lambda, \end{aligned} \quad (10)$$

where M stands for all the m_j and the subscript $\mathbf{0} \equiv \{0, 0, \dots\}$, and the sum is over all Λ consistent with the given ℓ_i (by the

introduction of intermediate ℓ_{12} , etc.). We have defined the following coefficient involving the primary angular momenta:

$$\mathcal{D}_\Lambda^{\text{P}} = \prod_{j=1}^n \sqrt{2\ell_j + 1}. \quad (11)$$

The superscript P stands for ‘‘primary’’. Since we will use it often, we write out $\mathcal{D}_\Lambda^{\text{P}}$ for $n = 3$ explicitly:

$$\mathcal{D}_{\ell_i \ell'_i \ell''_i}^{\text{P}} = \sqrt{(2\ell_i + 1)(2\ell'_i + 1)(2\ell''_i + 1)}. \quad (12)$$

When calculating the covariance matrix, we will encounter pairs of galaxy n -tuplets involving directional vectors $\{\mathbf{r}_i\}$ and $\{\mathbf{r}'_i\}$ with origins separated by a vector \mathbf{s} . Hence it is practical to consider a product of n isotropic \mathcal{P} functions of three arguments

$$\prod_{i=1}^n \mathcal{P}_{\ell_i \ell'_i \ell''_i}(\hat{\mathbf{r}}_i, \hat{\mathbf{r}}'_i, \hat{\mathbf{s}}) = \prod_{i=1}^n \sum_{m_i, m'_i, m''_i} \mathcal{C}_{m_i m'_i m''_i}^{\ell_i \ell'_i \ell''_i} Y_{\ell_i m_i}(\hat{\mathbf{r}}_i) Y_{\ell'_i m'_i}(\hat{\mathbf{r}}'_i) Y_{\ell''_i m''_i}(\hat{\mathbf{s}}). \quad (13)$$

Since the isotropic basis does not encode the absolute orientation of each galaxy n -tuple, we can average over orientation of the $\hat{\mathbf{r}}_i$, $\hat{\mathbf{r}}'_i$, and $\hat{\mathbf{s}}$ via Eq. (8) with the relative orientations of directional vectors within each galaxy n -tuplets fixed. Following this, we find

$$\begin{aligned} \int d\mathcal{R} d\mathcal{R}' d\mathcal{S} \prod_{i=1}^n \mathcal{P}_{\ell_i \ell'_i \ell''_i}(\hat{\mathbf{r}}_i, \hat{\mathbf{r}}'_i, \hat{\mathbf{s}}) \\ = (4\pi)^{-n/2} \sum_{\Lambda \Lambda' \Lambda''} \mathcal{Q}^{\Lambda \Lambda' \Lambda''} \mathcal{D}_{\Lambda''}^{\text{P}} \mathcal{C}_0^{\Lambda''} \mathcal{P}_\Lambda(\hat{\mathbf{R}}) \mathcal{P}_{\Lambda'}(\hat{\mathbf{R}}'). \end{aligned} \quad (14)$$

where the Λ , Λ' , and Λ'' are formed from the primary components ℓ_i , ℓ'_i , and ℓ''_i respectively. We introduce the quantity

$$\mathcal{Q}^{\Lambda \Lambda' \Lambda''} = \prod_{i=1}^n \sum_{m_i, m'_i, m''_i} \mathcal{C}_{m_i m'_i m''_i}^{\ell_i \ell'_i \ell''_i} \mathcal{C}_M^\Lambda \mathcal{C}_{M'}^{\Lambda'} \mathcal{C}_{M''}^{\Lambda''}, \quad (15)$$

where the subscripts M, M', M'' stand for collections of $\{m_i\}$, $\{m'_i\}$, and $\{m''_i\}$. Since $\mathcal{C}_{m_i m'_i m''_i}^{\ell_i \ell'_i \ell''_i}$ has a mixture of angular momenta we write out its components explicitly.

Our goal in this work is to study the covariance matrix, which by definition involves products of spherical harmonics. For this reason, it is of use to explore products of isotropic functions and their corresponding identities. Since the \mathcal{P}_Λ is a complete basis, it is possible to write products of two isotropic basis function with the same argument as a sum of isotropic basis function weighted by a coupling coefficient

$$\mathcal{P}_\Lambda(\hat{\mathbf{R}}) \mathcal{P}_{\Lambda'}(\hat{\mathbf{R}}) = \sum_{\Lambda''} \mathcal{E}(\Lambda'') \mathcal{G}^{\Lambda \Lambda' \Lambda''} \mathcal{P}_{\Lambda''}(\hat{\mathbf{R}}), \quad (16)$$

where the phase in the coefficient arises due to the conjugation property of the isotropic function $\mathcal{P}_{\Lambda''}^*(\hat{\mathbf{R}}) = \mathcal{E}(\Lambda'') \mathcal{P}_{\Lambda''}(\hat{\mathbf{R}})$ and we define $\mathcal{G}^{\Lambda \Lambda' \Lambda''}$ as the generalized Gaunt integral (Cahn & Slepian 2020):

$$\begin{aligned} \mathcal{G}^{\Lambda \Lambda' \Lambda''} &\equiv \int d\hat{\mathbf{R}} \mathcal{P}_\Lambda(\hat{\mathbf{R}}) \mathcal{P}_{\Lambda'}(\hat{\mathbf{R}}) \mathcal{P}_{\Lambda''}(\hat{\mathbf{R}}) \\ &= (4\pi)^{-n/2} \left[\prod_{i=1}^n \mathcal{D}_{\ell_i \ell'_i \ell''_i}^{\text{P}} \mathcal{C}_{000}^{\ell_i \ell'_i \ell''_i} \right] \mathcal{Q}^{\Lambda \Lambda' \Lambda''}. \end{aligned} \quad (17)$$

From its definition we see that $\mathcal{G}^{\Lambda \Lambda' \Lambda''}$ is symmetric in $\Lambda, \Lambda', \Lambda''$; we include its explicit evaluation for $n = 2, 3$ and 4 in Appendix A.

The isotropic function is expressed with arguments $\hat{\mathbf{r}}_1, \dots, \hat{\mathbf{r}}_n$ with the canonical ordering $i = 1, \dots, n$ (index sorted from small to large in \mathbf{r}_i). When we later consider the covariance, the contraction of the overdensity fields may be permuted such that the canonical ordering of the indices is no longer guaranteed. The isotropic functions with permuted arguments can be expanded in terms of the canonically ordered ones (since these latter form a complete basis) as:

$$\mathcal{P}_\Lambda(\hat{\mathbf{R}}_G) = \sum_{\Lambda'} \mathcal{B}_{\Lambda, \Lambda'}^{G^{-1}} \mathcal{P}_{\Lambda'}(\hat{\mathbf{R}}'), \quad (18)$$

where G denotes the permutation of the set $\{1, 2, \dots, n\}$. The reordering coefficient of the inverse permutation, $\mathcal{B}_{\Lambda, \Lambda'}^{G^{-1}}$, can be obtained by applying the orthogonality relation

$$\begin{aligned} \mathcal{B}_{\Lambda, \Lambda'}^{G^{-1}} &\equiv \int d\hat{\mathbf{R}} \mathcal{P}_\Lambda(\hat{\mathbf{R}}_G) \mathcal{P}_{\Lambda'}^*(\hat{\mathbf{R}}') \\ &= \sum_M \mathcal{C}_{m_1 m_2 m_{12} \dots m_n}^{\ell_1 \ell_2 \ell_{12} \dots \ell_n} \mathcal{C}_{m_{G_1} m_{G_2} m'_{12} \dots m_{G_n}}^{\ell_{G_1} \ell_{G_2} \ell'_{12} \dots \ell_{G_n}} \prod_{i=1}^n \delta_{\ell'_i \ell_{G_i-1}}^{\text{K}}, \end{aligned} \quad (19)$$

where G^{-1} denotes the inverse permutation of G . Here, products of Kronecker deltas ensure that Λ and Λ' have the same primary angular momenta; however, they may still differ in intermediate angular momenta.

3 N -POINT CORRELATION FUNCTIONS

The N -point correlation function (NPCF) is defined as

$$\zeta(\mathbf{r}_1, \mathbf{r}_2, \dots, \mathbf{r}_{N-1}) \equiv \langle \delta(\mathbf{x}) \delta(\mathbf{x} + \mathbf{r}_1) \delta(\mathbf{x} + \mathbf{r}_2) \cdots \delta(\mathbf{x} + \mathbf{r}_{N-1}) \rangle, \quad (20)$$

where the galaxy overdensity is given by $\delta(\mathbf{x}) = n(\mathbf{x})/\bar{n} - 1$, with $n(\mathbf{x})$ the galaxy number density with mean \bar{n} and $\langle \delta \rangle = 0$. The angle bracket denotes the ensemble average of the overdensity field.

The expectation value in Eq. (20) can be expanded as a sum of combinations of overdensity fields at different spatial positions. In the $N = 4$ case, the full 4PCF reads

$$\begin{aligned} \zeta(\mathbf{r}_1, \mathbf{r}_2, \mathbf{r}_3) &= \xi(\mathbf{r}_1)\xi(\mathbf{r}_2 - \mathbf{r}_3) + \xi(\mathbf{r}_2)\xi(\mathbf{r}_1 - \mathbf{r}_3) + \xi(\mathbf{r}_3)\xi(\mathbf{r}_1 - \mathbf{r}_2) + \zeta^c(\mathbf{r}_1, \mathbf{r}_2, \mathbf{r}_3) \\ &\equiv \zeta^{\text{dc}}(\mathbf{r}_1, \mathbf{r}_2, \mathbf{r}_3) + \zeta^c(\mathbf{r}_1, \mathbf{r}_2, \mathbf{r}_3), \end{aligned} \quad (21)$$

which consists of two parts. The *connected* four-point function $\zeta^c(\mathbf{r}_1, \mathbf{r}_2, \mathbf{r}_3)$ captures the non-Gaussian part of the signal. We denote the other terms, composed of the products of two-point correlation functions, as the *disconnected* part, $\zeta^{\text{dc}}(\mathbf{r}_1, \mathbf{r}_2, \mathbf{r}_3)$. For $N = 4$ the disconnected terms coincides with the 2PCF that sourced by Gaussian statistics. For $N > 4$ however, the disconnected piece can also receive non-Gaussian contributions, such as 2PCF+3PCF for the 5PCF. Our interest here is the non-Gaussianity induced by the higher order statistics. For this purpose, we employ a connected-only estimator that subtracts all the disconnected pieces at the estimator level (for details regarding the connected-only estimator, see our companion paper Philcox et al. 2021b).

In the limit of large volumes, V , we can replace the ensemble average by a spatial integral by invoking ergodicity. This motivates the general NPCF estimator

$$\hat{\zeta}(\mathbf{r}_1, \mathbf{r}_2, \dots, \mathbf{r}_{N-1}) = \int \frac{d\mathbf{x}}{V} \delta(\mathbf{x}) \delta(\mathbf{x} + \mathbf{r}_1) \delta(\mathbf{x} + \mathbf{r}_2) \cdots \delta(\mathbf{x} + \mathbf{r}_{N-1}), \quad (22)$$

which is unbiased. Using orthonormality to project this onto the isotropic basis \mathcal{P}_Λ (using $n = N - 1$) for given primary angular momenta $\Lambda \equiv \{\ell_1, \ell_2, (\ell_{12}), \dots, \ell_{N-1}\}$ as in Eq. (7), we obtain the estimator

$$\hat{\zeta}_\Lambda(r_1, r_2, \dots, r_{N-1}) = \int \frac{d^3\mathbf{x}}{V} \delta(\mathbf{x}) \prod_{i=1}^{N-1} \int d\hat{\mathbf{r}}_i \delta(\mathbf{x} + \mathbf{r}_i) \mathcal{P}_\Lambda^*(\hat{\mathbf{r}}_1, \hat{\mathbf{r}}_2, \dots, \hat{\mathbf{r}}_{N-1}). \quad (23)$$

Explicitly, for the 4PCF, we find:

$$\hat{\zeta}_\Lambda(r_1, r_2, r_3) = \int \frac{d^3\mathbf{x}}{V} \delta(\mathbf{x}) \int d\hat{\mathbf{r}}_1 d\hat{\mathbf{r}}_2 d\hat{\mathbf{r}}_3 \delta(\mathbf{x} + \mathbf{r}_1) \delta(\mathbf{x} + \mathbf{r}_2) \delta(\mathbf{x} + \mathbf{r}_3) \mathcal{P}_{\ell_1 \ell_2 \ell_3}^*(\hat{\mathbf{r}}_1, \hat{\mathbf{r}}_2, \hat{\mathbf{r}}_3). \quad (24)$$

Throughout this paper we make two important assumptions. First, we work in the Gaussian limit for the covariance calculation. Even though the gravitationally-induced higher-order statistics entering the covariance in principle do not vanish, we assume they are suppressed compared to the two-point statistics. This assumption greatly simplifies the derivation below as we will only need to consider the contractions between two overdensity fields, and thus may express results entirely in terms of the 2PCF or the power spectrum. This assumption will be addressed below by comparing the Gaussian covariance to that obtained from N -body simulations. Second, we assume the 2PCF, and likewise the power spectrum, are isotropic. The majority of the paper is based on this assumption, however, §5 includes a comparison between the theoretical isotropic Gaussian covariance numerical simulations including RSD, which breaks rotational invariance.

We use the following conventions for Fourier transforms:

$$\tilde{\delta}(\mathbf{k}) = \int d^3\mathbf{r} e^{-i\mathbf{k}\cdot\mathbf{r}} \delta(\mathbf{r}), \quad \delta(\mathbf{r}) = \int_{\mathbf{k}} e^{i\mathbf{k}\cdot\mathbf{r}} \tilde{\delta}(\mathbf{k}), \quad (25)$$

where we define $\int_{\mathbf{k}} \equiv (2\pi)^{-3} \int d^3\mathbf{k}$. The 2PCF $\xi(\mathbf{r})$ and power spectrum $P(\mathbf{k})$ are related by

$$\langle \delta(\mathbf{r}_i) \delta(\mathbf{r}_j) \rangle = \xi(|\mathbf{r}_i - \mathbf{r}_j|) = \int_{\mathbf{k}} P(\mathbf{k}) e^{i\mathbf{k}\cdot(\mathbf{r}_i - \mathbf{r}_j)}. \quad (26)$$

Hereafter, we assume isotropy, and thus assume $P(\mathbf{k}) \equiv P(k)$, with $k = |\mathbf{k}|$, and $\xi(\mathbf{r}) \equiv \xi(r)$. In Appendix E we will discuss how to go beyond the assumption of an isotropic power spectrum.

4 DERIVATION OF THE GAUSSIAN NPCF COVARIANCE MATRICES

The covariance matrix for the NPCF is defined as

$$\begin{aligned}
\text{Cov}(\hat{\zeta}(\mathbf{R}), \hat{\zeta}(\mathbf{R}')) &\equiv \langle \hat{\zeta}(\mathbf{R}) \hat{\zeta}^*(\mathbf{R}') \rangle - \langle \hat{\zeta}(\mathbf{R}) \rangle \langle \hat{\zeta}^*(\mathbf{R}') \rangle \\
&= \int \frac{d^3 \mathbf{x}}{V} \frac{d^3 \mathbf{x}'}{V} \left\langle \prod_{i=0}^{N-1} \delta(\mathbf{x} + \mathbf{r}_i) \delta(\mathbf{x}' + \mathbf{r}'_i) \right\rangle - \langle \hat{\zeta}(\mathbf{R}) \rangle \langle \hat{\zeta}^*(\mathbf{R}') \rangle \\
&= \int \frac{d^3 \mathbf{s}}{V} \left\langle \prod_{i=0}^{N-1} \delta(\mathbf{x} + \mathbf{r}_i) \delta(\mathbf{x} + \mathbf{r}'_i + \mathbf{s}) \right\rangle - \langle \hat{\zeta}(\mathbf{R}) \rangle \langle \hat{\zeta}^*(\mathbf{R}') \rangle,
\end{aligned} \tag{27}$$

where $\hat{\zeta}(\mathbf{R})$ is the NPCF estimator with coordinates $\mathbf{R} = \{\mathbf{r}_1, \mathbf{r}_2, \dots, \mathbf{r}_{N-1}\}$, with an analogous definition for \mathbf{R}' . Going from the second to the third line we have defined the separation vector between the primary galaxies of the two N -plets as $\mathbf{s} \equiv \mathbf{x}' - \mathbf{x}$, and dropped the spatial integral over \mathbf{x} , assuming statistical homogeneity.³ We label the vertices containing \mathbf{r}_0 and \mathbf{r}'_0 as *primary vertices* (with $\mathbf{r}_0 = \mathbf{r}'_0 = \mathbf{0}$) and label the $(N-1)$ points with separations $\mathbf{r}_1, \mathbf{r}_2, \dots, \mathbf{r}_{N-1}$ relative to the primary as *endpoints*. In the Gaussian limit we only need to calculate contractions between pairs of overdensity fields. The NPCF covariance has $2N$ overdensity fields and thus forms N pairs of contractions.

Whereas the definition of the covariance matrix given in Eq. (27) (evaluated under the assumption of Gaussianity) includes all possible contractions of $2N$ density fields, in this section we consider only pairs that are contractions between unprimed and primed families, *i.e.* between \mathbf{r}_i and \mathbf{r}'_j . We term these contractions (and the corresponding covariance matrix contribution) “fully-coupled”, as they fully couple the unprimed and primed families. Any self-contraction (*i.e.* that involving contraction of two density fields within the same family, *i.e.* between \mathbf{r}_i and \mathbf{r}_j with $i \neq j$) arises from the disconnected contributions to the NPCF. We term any covariance contribution that includes at least one self-contraction “partially-coupled”. All such contributions vanish in the covariance of the connected-only estimator (Philcox et al. 2021b). This fact allows us to focus on the fully-coupled covariance terms.⁴

Below, we derive a general expression for the fully-coupled NPCF covariance matrix under the assumption that the density fields are Gaussian distributed. In order to offer a more intuitive understanding of the coupling structure, we also present a diagrammatic approach to the calculation.

4.1 Basic elements for the covariance

We first consider the coupling between two endpoints: specifically, $\delta(\mathbf{x} + \mathbf{r}_i)$ from the unprimed family and $\delta(\mathbf{x} + \mathbf{s} + \mathbf{r}'_j)$ from the primed family, with i and j between 0 and $N-1$. Such a contraction is represented by the tripolar structure in Fig. 1. The primary vertices, \mathbf{r}_0 and \mathbf{r}'_0 , are indexed as a convenience for keeping track of the permutations of unprimed and primed density fields; we will need such permutations later in the calculation. However, once we have computed our desired contractions in the isotropic basis, we may evaluate the result at $\mathbf{r}_0 = 0$ and $\mathbf{r}'_0 = 0$, since we place the primary vertices at \mathbf{x} and \mathbf{x}' respectively. We display this approach in Fig. 1.

Expanding the contraction $\langle \delta(\mathbf{x} + \mathbf{r}_i) \delta(\mathbf{x} + \mathbf{s} + \mathbf{r}'_j) \rangle$ in the isotropic basis, we find

$$\begin{aligned}
\langle \delta(\mathbf{x} + \mathbf{r}_i) \delta(\mathbf{x} + \mathbf{s} + \mathbf{r}'_j) \rangle &\equiv \xi(|\mathbf{r}'_j + \mathbf{s} - \mathbf{r}_i|) \\
&= (4\pi)^{3/2} \sum_{\ell_i \ell'_j L} i^{-\ell_i + \ell'_j + L} f_{\ell_i \ell'_j L}(r_i, r'_j, s) \mathcal{D}_{\ell_i \ell'_j L}^{\text{P}} \mathcal{C}_{000}^{\ell_i \ell'_j L} \mathcal{P}_{\ell_i \ell'_j L}(\hat{\mathbf{r}}_i, \hat{\mathbf{r}}'_j, \hat{\mathbf{s}}).
\end{aligned} \tag{28}$$

A detailed derivation of this is in Appendix B. The highlighted radial part corresponds to Fig. 1 **diagram (4)**. To simplify what follows, we introduce the f -integral:

$$f_{\ell_1 \ell_2 \ell_3}(r_1, r_2, r_3) \equiv \int \frac{k^2 dk}{2\pi^2} P(k) j_{\ell_1}(kr_1) j_{\ell_2}(kr_2) j_{\ell_3}(kr_3), \tag{29}$$

following equation (64) in Slepian & Eisenstein (2015a). In practice, this is computed in radial bins, wherein we average each spherical Bessel function (sBF) over r_i with weight r_i^2 (cf. Eq. D2).⁵

We now consider the forms of equation (28) when i and j assume different values. There are three distinct cases. First, we have a primary-to-primary coupling (the highlighted radial part corresponds to Fig. 1, **diagram (1)**):

$$\langle \delta(\mathbf{x} + \mathbf{r}_0) \delta(\mathbf{x} + \mathbf{s} + \mathbf{r}'_0) \rangle |_{r_0=r'_0=0} = \xi(|\mathbf{r}'_0 + \mathbf{s} - \mathbf{r}_0|) |_{r_0=r'_0=0} = (4\pi)^{3/2} f_{000}(0, 0, s) \mathcal{P}_{000}(0, 0, \hat{\mathbf{s}}), \tag{30}$$

³ Strictly, we first need to apply a Poisson average to discrete tracers, giving rise to the shot noise term. Here we use abbreviated notation and replace $P(k) \rightarrow P(k) + \bar{n}^{-1}$, for number density \bar{n}^{-1} , when we later compare our analytic results to those from the simulations.

⁴ With the introduction of the connected-only estimator implies that the disconnected terms can be isolated and that calculation of their associated partially-coupled covariance is not strictly needed, we provide its derivation in Appendix C1 for completeness.

⁵ Importantly, the bin average commutes with the integral and can be done prior to the k integration, which avoids performing the integral over fine radial bins.

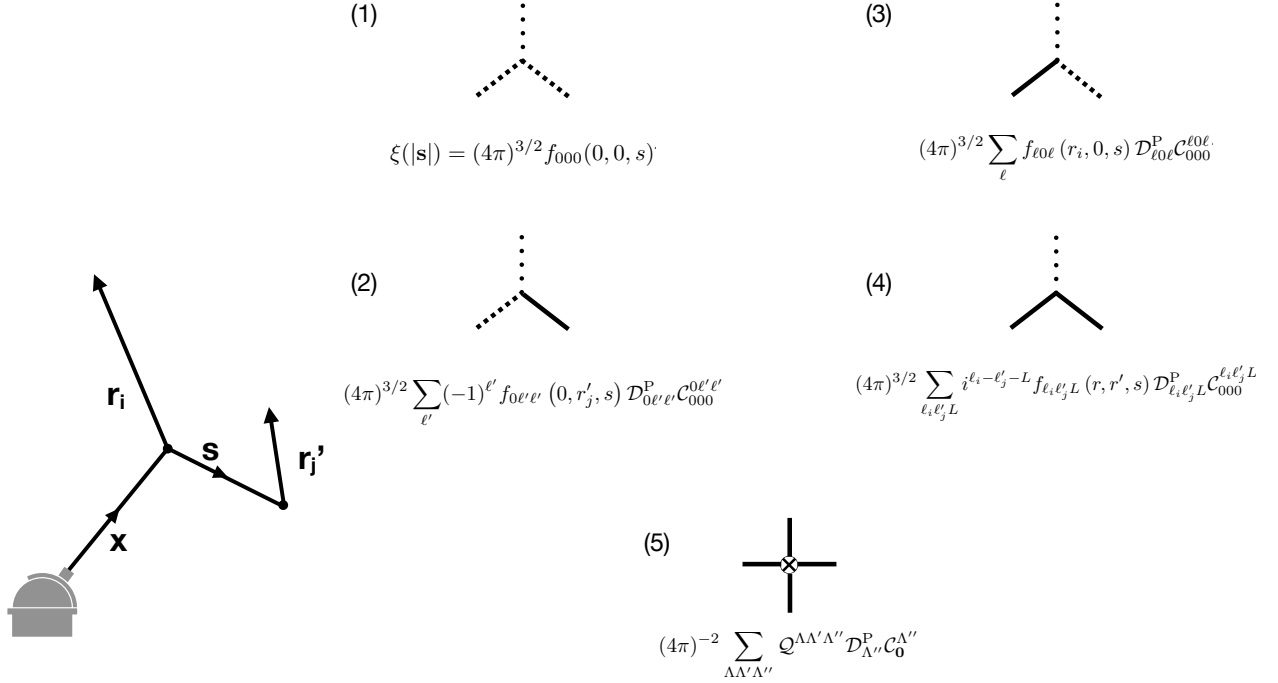


Figure 1. A diagrammatic representation of the basic elements used as building blocks for the fully-coupled (*i.e.* connected) covariance. Coupling between the overdensity fields across the unprimed and primed family (corresponding to density fields from the first and second NPCFs in Eq. 27) is represented by a tripolar structure (**diagrams (1)-(4)**, cf. Eqs. 28-31). Each tripolar structure depends on three vectors: \mathbf{r}_i , \mathbf{r}'_j , and \mathbf{s} . We use dotted lines to represent the separation vector \mathbf{s} . Dashed lines depict primary vertices for \mathbf{r}_0 or \mathbf{r}'_0 and solid lines are for endpoints with i or j non-zero. **Diagram (5)** is the coupling kernel arising from the rotational average over the unit vectors \mathbf{r} , \mathbf{r}' , and \mathbf{s} (cf. second line in Eq. 34). In the $N = 4$ case the coupling kernel has four legs. The lower left diagram (with the cartoon telescope) shows our coordinate convention. \mathbf{x} denotes the absolute coordinate; \mathbf{r}_i and \mathbf{r}'_j are the relative coordinates for respectively the unprimed and primed families. \mathbf{s} is the separation vector between the two families.

Second, we have a primary-to-endpoint coupling. These couplings can be obtained by taking one of \mathbf{r}_0 or \mathbf{r}'_0 and their associated angular momenta to zero. In the first line below, the primary is unprimed and the endpoint is primed. In the second line, we give the alternate choice, easily obtained by symmetry. Below, the highlighted radial parts correspond to Fig. 1, **diagrams (2) and (3)**. We have:

$$\langle \delta(\mathbf{x} + \mathbf{r}_0) \delta(\mathbf{x} + \mathbf{r}'_j) \rangle |_{\mathbf{r}_0=0} = \xi(|\mathbf{r}'_j + \mathbf{s} - \mathbf{r}_0|) |_{\mathbf{r}_0=0} = (4\pi)^{3/2} \sum_{\ell'} (-1)^{\ell'} f_{0\ell'\ell'}(0, r'_j, \mathbf{s}) \mathcal{D}_{0\ell'\ell'}^P \mathcal{C}_{000}^{0\ell'\ell'} \mathcal{P}_{0\ell'\ell'}(0, \hat{\mathbf{r}}'_j, \hat{\mathbf{s}}) \quad (31)$$

$$\langle \delta(\mathbf{x} + \mathbf{r}_i) \delta(\mathbf{x} + \mathbf{r}'_0 + \mathbf{s}) \rangle |_{\mathbf{r}'_0=0} = \xi(|\mathbf{s} + \mathbf{r}'_0 - \mathbf{r}_i|) |_{\mathbf{r}'_0=0} = (4\pi)^{3/2} \sum_{\ell} f_{\ell 0\ell}(r_i, 0, \mathbf{s}) \mathcal{D}_{\ell 0\ell}^P \mathcal{C}_{000}^{\ell 0\ell} \mathcal{P}_{\ell 0\ell}(\hat{\mathbf{r}}_i, 0, \hat{\mathbf{s}}). \quad (32)$$

Finally, we have an endpoint-to-endpoint coupling, which is already given by Eq. (28).

4.2 Fully-coupled Gaussian covariance

4.2.1 General formalism for fully-coupled Gaussian NPCF covariance

The covariance defined in Eq. (27) can be expanded into the isotropic basis. Using Eq. (28), each pair contraction can be written as a Fourier transform of the power spectrum, which can be expressed as products of the basic elements with tripolar

structure defined in §4.1:

$$\begin{aligned}
\text{Cov}(\hat{\zeta}(\mathbf{R}), \hat{\zeta}(\mathbf{R}')) &= \sum_{\Lambda, \Lambda'} \mathcal{E}(\Lambda') \text{Cov}_{\Lambda, \Lambda'}(R, R') \mathcal{P}_{\Lambda}(\hat{\mathbf{R}}) \mathcal{P}_{\Lambda'}(\hat{\mathbf{R}}') \\
&= \int \frac{d^3 \mathbf{s}}{V} \sum_G \prod_{i=0}^{N-1} \langle \delta(\mathbf{x} + \mathbf{r}_{Gi}) \delta(\mathbf{x} + \mathbf{r}'_i + \mathbf{s}) \rangle |_{r_{G0}=r'_0=0} \\
&= \int \frac{d^3 \mathbf{s}}{V} (4\pi)^{3N/2} \sum_G \prod_{i=0}^{N-1} \sum_{\ell_{Gi} \ell'_i L_i} i^{-\ell_{Gi} + \ell'_i + L_i} f_{\ell_{Gi} \ell'_i L_i}(r_{Gi}, r'_i, \mathbf{s}) \\
&\quad \times \mathcal{D}_{\ell_{Gi} \ell'_i L_i}^{\text{P}} \mathcal{C}_{000}^{\ell_{Gi} \ell'_i L_i} \mathcal{P}_{\ell_{Gi} \ell'_i L_i}(\hat{\mathbf{r}}_{Gi}, \hat{\mathbf{r}}'_i, \hat{\mathbf{s}}) |_{r_{G0}=r'_0=0},
\end{aligned} \tag{33}$$

where we define $\text{Cov}_{\Lambda, \Lambda'}(\zeta(R), \zeta(R')) \equiv \text{Cov}_{\Lambda, \Lambda'}(R, R')$ and use the conjugation property $\mathcal{P}_{\Lambda'}^*(\hat{\mathbf{R}}') = \mathcal{E}(\Lambda') \mathcal{P}_{\Lambda'}(\hat{\mathbf{R}}')$. We denote the permutation by G , with a total of $N!$ permutation terms. Since the basis is isotropic, we can apply Eq. (14) and rotationally average over $d\mathcal{R}$, $d\mathcal{R}'$, and $d\mathcal{S}$ (with the normalization $\int d\mathcal{S} = (4\pi)^{-1} \int d\hat{\mathbf{s}}$):

$$\begin{aligned}
&\sum_{\Lambda, \Lambda'} \mathcal{E}(\Lambda') \text{Cov}_{\Lambda, \Lambda'}(R, R') \mathcal{P}_{\Lambda}(\hat{\mathbf{R}}) \mathcal{P}_{\Lambda'}(\hat{\mathbf{R}}') \\
&= \int \frac{s^2 ds}{V} 4\pi (4\pi)^{3N/2} \sum_G \sum_{\mathcal{L}_G \mathcal{L}' \Lambda''} \prod_{i=0}^{N-1} i^{-\ell_{Gi} + \ell'_i + L_i} f_{\ell_{Gi} \ell'_i L_i}(r_{Gi}, r'_i, \mathbf{s}) \mathcal{D}_{\ell_{Gi} \ell'_i L_i}^{\text{P}} \mathcal{C}_{000}^{\ell_{Gi} \ell'_i L_i} \\
&\quad \times (4\pi)^{-N/2} \mathcal{Q}^{\mathcal{L}_G \mathcal{L}' \Lambda''} \mathcal{D}_{\Lambda''}^{\text{P}} \mathcal{C}_0^{\Lambda''} \mathcal{P}_{\mathcal{L}_G}(\hat{\mathbf{R}}_G^{(N)}) \mathcal{P}_{\mathcal{L}'}(\hat{\mathbf{R}}'^{(N)}) |_{r_{G0}=r'_0=0} \\
&= \int \frac{s^2 ds}{V} 4\pi (4\pi)^{3N/2} \sum_G \sum_{\mathcal{L}_G \mathcal{L}' \Lambda''} \prod_{i=0}^{N-1} i^{-\ell_{Gi} + \ell'_i + L_i} f_{\ell_{Gi} \ell'_i L_i}(r_{Gi}, r'_i, \mathbf{s}) \\
&\quad \times \mathcal{G}^{\mathcal{L}_G \mathcal{L}' \Lambda''} \mathcal{D}_{\Lambda''}^{\text{P}} \mathcal{C}_0^{\Lambda''} \mathcal{P}_{\mathcal{L}_G}(\hat{\mathbf{R}}_G^{(N)}) \mathcal{P}_{\mathcal{L}'}(\hat{\mathbf{R}}'^{(N)}) |_{r_{G0}=r'_0=0}
\end{aligned} \tag{34}$$

where we denote $\mathcal{L}_G \equiv \{\ell_{G0}, \ell_{G1}, \dots, \ell_{G(N-1)}\}$, $\mathcal{L}' \equiv \{\ell'_0, \ell'_1, \dots, \ell'_{N-1}\}$ as the angular momenta associated with the \mathbf{R} and \mathbf{R}' vectors, $\Lambda'' \equiv \{L_0, L_1, \dots, L_{N-1}\}$ as the angular momentum associated with the separation vector \mathbf{s} , and $M'' = \{M_0, M_1, \dots, M_N\}$. The highlighted coefficients give rise to the coupling kernel in Fig. 1, **diagram (5)**. Notice that the isotropic basis used herein has N coordinates (instead of $N - 1$, as in the NPCF definition of Eq. 23), given that we evaluate the function at $\mathbf{r}_0 = 0$, $\mathbf{r}'_0 = 0$ with corresponding angular momentum $\ell_{G0} = 0$ and $\ell'_0 = 0$. Later, we will project the covariance onto the $(N - 1)$ basis; for clarity we distinguish the two with the superscript (N) . Since both $\mathcal{P}_{\mathcal{L}_G}(\hat{\mathbf{R}}_G^{(N)})$ and $\mathcal{P}_{\mathcal{L}'}(\hat{\mathbf{R}}'^{(N)})$ contain a factor $Y_{00}(\hat{\mathbf{r}}_0) = (4\pi)^{-1/2}$, we find a total prefactor $(4\pi)^{-1}$. This cancels with our normalization convention for the rotational average. The non-canonically ordered isotropic function, $\mathcal{P}_{\mathcal{L}_G}(\hat{\mathbf{R}}_G^{(N)})$, can be rewritten using the reordering coefficient defined in Eq. (19):

$$\mathcal{P}_{\mathcal{L}_G}(\hat{\mathbf{R}}_G^{(N)}) = \sum_J \mathcal{B}_{\mathcal{L}_G, J}^{G-1} \mathcal{P}_J(\hat{\mathbf{R}}^{(N)}). \tag{35}$$

Finally, we project the covariance onto the isotropic basis $\mathcal{P}_{\Lambda}^*(\hat{\mathbf{R}})$ and $\mathcal{P}_{\Lambda'}^*(\hat{\mathbf{R}}')$, and perform an angular average over \mathbf{r} and \mathbf{r}' . Orthogonality forces $J \rightarrow \Lambda$ and $\mathcal{L}' \rightarrow \Lambda'$, giving the general form for the NPCF covariance:

$$\begin{aligned}
&\text{Cov}_{\Lambda, \Lambda'}(R, R') \\
&= (4\pi)^{3N/2} \int \frac{s^2 ds}{V} \sum_G \sum_{\Lambda'', \mathcal{L}_G} (-1)^{[-\Sigma(\Lambda) - \Sigma(\Lambda') + \Sigma(\Lambda'')]/2} \mathcal{B}_{\mathcal{L}_G, \Lambda}^{G-1} \mathcal{G}^{\mathcal{L}_G \Lambda''} \mathcal{D}_{\Lambda''}^{\text{P}} \mathcal{C}_0^{\Lambda''} \prod_{i=0}^{N-1} f_{\ell_{Gi} \ell'_i L_i}(r_{Gi}, r'_i, \mathbf{s}) |_{r_{G0}=r'_0=0},
\end{aligned} \tag{36}$$

where $\Sigma(\Lambda) = \sum_i \ell_i$, $\Sigma(\Lambda') = \sum_i \ell'_i$, and $\Sigma(\Lambda'') = \sum_i L_i$.

4.2.2 Fully-coupled Gaussian 4PCF covariance

Henceforth, we will focus on the fully-coupled covariance of the 4PCF. To derive this, we can use the general form given in Eq. (36); however, as an explicit verification, we construct the 4PCF covariance in a different manner. Noticing that contractions with the primary vertices lead to basis functions involving zero angular momenta, we split the fully-coupled covariance into two different cases: those involving a mutual coupling of the primary vertices $\delta(\mathbf{r}_0)$ and $\delta(\mathbf{r}'_0 + \mathbf{s})$ (upper panel of Fig. 2) and those where the primary vertices couple to the endpoints of the opposite family (lower panel of Fig. 2). In this decomposition, the fully-coupled covariance can be written

$$\text{Cov}_{\Lambda, \Lambda'}^{(\text{fc})}(R, R') = \text{Cov}_{\Lambda, \Lambda'}^{(\text{fc}), \text{I}}(R, R') + \text{Cov}_{\Lambda, \Lambda'}^{(\text{fc}), \text{II}}(R, R'); \tag{37}$$

next, we will discuss these two cases.

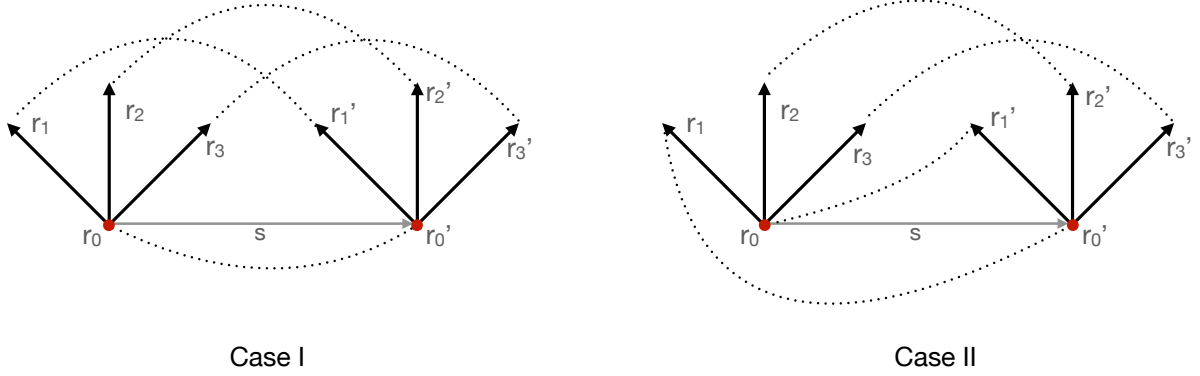


Figure 2. Schematic for the fully-coupled 4PCF covariance (*i.e.* the covariance of the connected 4PCF). We split the covariance into two cases. In **Case I**, the primary vertices (red dots, labelled by \mathbf{r}_0 and \mathbf{r}'_0) from the primed and unprimed families are mutually coupled and all the endpoints (labelled by \mathbf{r}_i and \mathbf{r}'_i) are coupled. In **Case II**, the primary vertices each are coupled to an endpoint from the opposite family.

Case I In this scenario the contraction of the eight density fields leads to the term

$$\begin{aligned}
 I_1(\mathbf{R}, \mathbf{R}'; \mathbf{s}) &\equiv \langle \delta(\mathbf{x} + \mathbf{r}_0) \delta(\mathbf{x} + \mathbf{s} + \mathbf{r}'_0) \rangle |_{\mathbf{r}_0 = \mathbf{r}'_0 = 0} \\
 &\quad \times \langle \delta(\mathbf{x}' + \mathbf{r}_i) \delta(\mathbf{x}' + \mathbf{s} + \mathbf{r}'_i) \rangle \langle \delta(\mathbf{x}'' + \mathbf{r}_j) \delta(\mathbf{x}'' + \mathbf{s} + \mathbf{r}'_j) \rangle \langle \delta(\mathbf{x}''' + \mathbf{r}_k) \delta(\mathbf{x}''' + \mathbf{s} + \mathbf{r}'_k) \rangle \\
 &= \sum_G \xi(|\mathbf{s} + \mathbf{r}'_0 - \mathbf{r}_0|) \xi(|\mathbf{s} + \mathbf{r}'_1 - \mathbf{r}_{G1}|) \xi(|\mathbf{s} + \mathbf{r}'_2 - \mathbf{r}_{G2}|) \xi(|\mathbf{s} + \mathbf{r}'_3 - \mathbf{r}_{G3}|) |_{\mathbf{r}_0 = \mathbf{r}'_0 = 0},
 \end{aligned}$$

defining the shorthand I_1 in the first line. Here, $\{i, j, k\}$ denotes a permutation of the set $\{1, 2, 3\}$, which does not include the primary vertices at \mathbf{r}_0 and \mathbf{r}'_0 . There are $3! = 6$ options by which to contract the remaining three density fields from the primed and unprimed families. In the second line we introduce the notation G to denote a permutation, with $\{i, j, k\} = \{G1, G2, G3\}$. The six permutations are given explicitly in Table 1. Using the basic elements constructed in Eq. (28), we can express the product of the four 2PCFs as

$$I_1(\mathbf{R}, \mathbf{R}'; \mathbf{s}) = \sum_G \prod_{i=0}^3 (4\pi)^{3/2} \sum_{\ell_{G_i} \ell'_{i'} L_i} i^{-\ell_{G_i} + \ell'_{i'} + L_i} f_{\ell_{G_i} \ell'_{i'} L_i}(r_{G_i}, r'_{i'}, s) \mathcal{D}_{\ell_{G_i} \ell'_{i'} L_i}^P C_{000}^{\ell_{G_i} \ell'_{i'} L_i} \mathcal{P}_{\ell_{G_i} \ell'_{i'} L_i}(\hat{\mathbf{r}}_{G_i}, \hat{\mathbf{r}}'_{i'}, \hat{\mathbf{s}}) |_{\mathbf{r}_0 = \mathbf{r}'_0 = 0}; \quad (38)$$

here we denote the collection of angular momenta as $\mathcal{L}_G = \{0, \ell_{G1}, \ell_{G2}, \ell_{G3}\}$, $\mathcal{L}' = \{0, \ell'_{1'}, \ell'_{2'}, \ell'_{3'}\}$ and $\Lambda'' = \{0, L_1, L_2, L_3\}$. In principle, these should all involve intermediate angular momenta, however, the angular momentum associated with primary vertex is set to be zero, thus the intermediate momenta are uniquely defined.

Performing a rotational average of $d\mathcal{R}$, $d\mathcal{R}'$, and $d\mathcal{S}$ over $\hat{\mathbf{r}}_{G_i}$, $\hat{\mathbf{r}}'_{i'}$, and $\hat{\mathbf{s}}$, leads to the quantity $\mathcal{Q}^{\Lambda_G \Lambda' \Lambda''}$ and a prefactor $(4\pi)^{-2}$ for $N = 4$. When combined with the coefficients $\mathcal{D}_{\ell_{G_i} \ell'_{i'} L_i}^P$ and $C_{000}^{\ell_{G_i} \ell'_{i'} L_i}$ for $i = 0, \dots, 3$ (cf. Eq. (14) and Eq. (17)), we obtain the generalized Gaunt integral. The Gaunt integral for $N = 4$ involves a product of two 9- j symbols and intermediate angular momenta given in Eq. (A3). However, one of the 9- j symbol can be reduced due to the presence zero angular momenta, and the fully determined intermediate angular momenta: $\ell_{12} = \ell_{G1}$, $\ell'_{12} = \ell'_{1'}$, and $\ell_{12} = \ell_{G1}$. The Gaunt integral in this case reads

$$\begin{aligned}
 \mathcal{G}^{\Lambda_G \Lambda' \Lambda''} &= (4\pi)^{-2} \mathcal{D}_{\ell_{G1} \ell'_{1'} L_1}^P \prod_{i=0}^3 \mathcal{D}_{\ell_{G_i} \ell'_{i'} \Lambda_i}^P C_{000}^{\ell_{G_i} \ell'_{i'} L_i} \begin{Bmatrix} 0 & \ell_{G1} & \ell_{G1} \\ 0 & \ell'_{1'} & \ell'_{1'} \\ 0 & L_1 & L_1 \end{Bmatrix} \begin{Bmatrix} \ell_{G1} & \ell_{G2} & \ell_{G3} \\ \ell'_{1'} & \ell'_{2'} & \ell'_{3'} \\ L_1 & L_2 & L_3 \end{Bmatrix} \\
 &= (4\pi)^{-2} \prod_{i=0}^3 \mathcal{D}_{\ell_{G_i} \ell'_{i'} \Lambda_i}^P C_{000}^{\ell_{G_i} \ell'_{i'} L_i} \begin{Bmatrix} \ell_{G1} & \ell_{G2} & \ell_{G3} \\ \ell'_{1'} & \ell'_{2'} & \ell'_{3'} \\ L_1 & L_2 & L_3 \end{Bmatrix}, \quad (39)
 \end{aligned}$$

where $\mathcal{D}_{\ell_{G1} \ell'_{1'} L_1}^P$ in the first line is cancelled by the first 9- j symbol, leaving only one 9- j symbol in the second line. Here

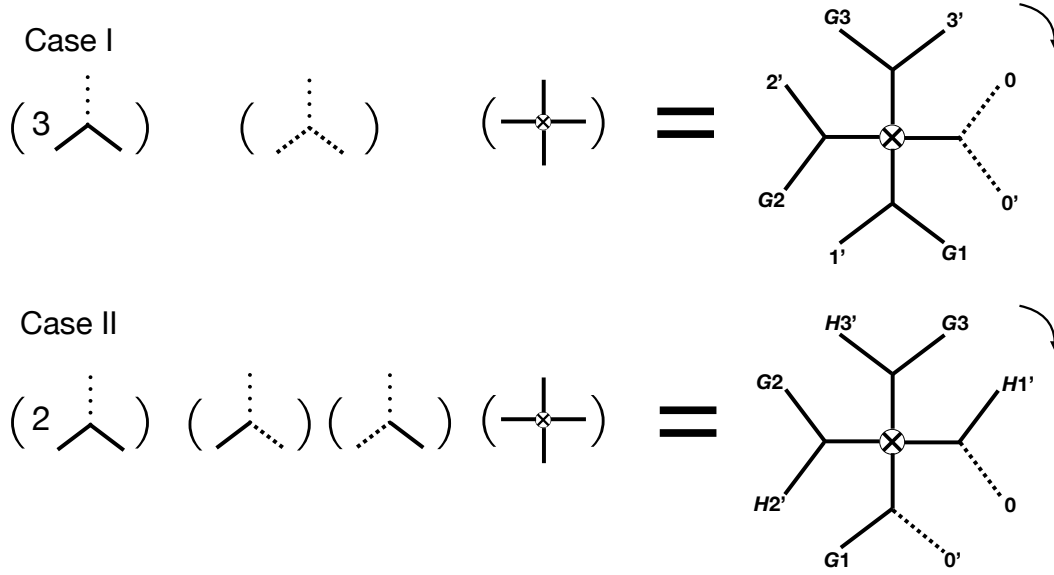


Figure 3. A diagrammatic representation of a fully-coupled covariance matrix with **Case I** shown in the **upper panel** and **Case II** in the **lower panel** (as in Fig. 2). Each case can be broken down into two elementary structures: (a) a tripolar structure arising from the contraction between overdensity fields from the primed and unprimed families, and (b) a coupling kernel given by the rotational average over \mathbf{r} , \mathbf{r}' , and \mathbf{s} . Moreover, since the covariance involves two primary vertices (one from the primed and the other from the unprimed family), there are two dashed lines either connected to each other or connected to a solid line. All the three pieces are multiplied, summed over the angular momenta, and integrated over s . In this figure we use G_i and H_i to denote permutations. For $N = 4$, the phase $(-1)^{\Sigma(\Lambda)(1-\mathcal{E}_G)/2}$ or $(-1)^{\Sigma(\Lambda')(1-\mathcal{E}_H)/2}$ can be directly read off from the plot as one goes around clockwise: an even permutation in the ordering of angular momenta corresponds to a positive Levi-Civita symbol and always gives a positive phase, while an odd permutation can flip the sign of the phase for parity-odd correlators. **Diagrams (2) and (3)** in Fig. 1 can be distinguished from each other by reading the diagram clockwise (*i.e.* one cannot change one into the other by a 2D rotation in the page). The following steps are used to build the “snowflake” diagrams on the right hand sides of the equation: (1) take the tripolar structures and multiply them with the coupling kernel, (2) perform an integral over the radial part s of the separation vectors.

we introduce a Levi-Civita symbol, defined by $\mathcal{E}_G = 1$ if $\{G1, G2, G3\}$ is an even permutation of $\{1, 2, 3\}$ and -1 otherwise. The values of \mathcal{E}_G for each permutation G are given in Table 1. Practically, this leads to a prefactor of $(-1)^{\ell_1 + \ell_2 + \ell_3}$ if the permutation is odd, and unity otherwise. For the even-parity Λ this phase does not play a role, but it is of importance for odd parity Λ .

Using Eq. (18), we can restore the canonical ordering in $\hat{\mathbf{R}}_G = \{\hat{\mathbf{r}}_{G1}, \hat{\mathbf{r}}_{G2}, \hat{\mathbf{r}}_{G3}\}$. For the 4PCF covariance, the reordering coefficient $\mathcal{B}_{\mathcal{L}_G, J}^{G-1}$ for $(N-1) = 3$ involves only a phase and the product three of Kronecker deltas:

$$\mathcal{B}_{\mathcal{L}_G, J}^{G-1} = (-1)^{\Sigma(\Lambda)(1-\mathcal{E}_G)/2} \prod_{i=1}^3 \delta_{ji}^K \delta_{G_i-1}. \quad (40)$$

Performing angular averages over $\hat{\mathbf{R}}$ and $\hat{\mathbf{R}}'$ allows us to set $J \rightarrow \Lambda$ and pick out the coefficients of the isotropic basis $\mathcal{P}_\Lambda(\hat{\mathbf{R}})$ and $\mathcal{P}_{\Lambda'}(\hat{\mathbf{R}}')$. Altogether, we arrive at the final form for Case I:

$$\begin{aligned} \text{Cov}_{\Lambda, \Lambda'}^{(\text{fc}), \text{I}}(R, R') &= (4\pi)^4 \sum_G (-1)^{\Sigma(\Lambda)(1-\mathcal{E}_G)/2} \sum_{L_1 L_2 L_3} \mathcal{D}_{L_1 L_2 L_3}^{\text{P}} C_{000}^{L_1 L_2 L_3} \begin{Bmatrix} \ell_{G1} & \ell_{G2} & \ell_{G3} \\ \ell'_1 & \ell'_2 & \ell'_3 \\ L_1 & L_2 & L_3 \end{Bmatrix} \\ &\times \prod_{i=1}^3 \left[(-1)^{(-\ell_{G_i} - \ell'_i + L_i)/2} \mathcal{D}_{\ell_i \ell'_i L_i}^{\text{P}} C_{000}^{\ell_{G_i} \ell'_i L_i} \int \frac{s^2 ds}{V} \xi(s) f_{\ell_{G_i} \ell'_i L_i}(r_{G_i}, r'_i, s) \right]. \end{aligned} \quad (41)$$

For illustration, we consider the limit where the correlation function $\xi(\mathbf{s})$ becomes a Dirac delta function, and the power spectrum consequently becomes unity. This limit enables a direct evaluation of both Eq. (38) and its representation Eq. (41), providing a useful cross-check of our calculation.

From Eq. (38), we see that $\xi(\mathbf{s}) \rightarrow \delta_{\text{D}}^{[3]}(\mathbf{s})$ implies that $\mathbf{s} \rightarrow \mathbf{0}$. Consequently, we have that $\mathbf{r}'_1 \rightarrow \mathbf{r}_{G1}$, $\mathbf{r}'_2 \rightarrow \mathbf{r}_{G2}$, $\mathbf{r}'_3 \rightarrow \mathbf{r}_{G3}$. We now consider the representation in terms of f -integrals. For the first, taking $P(k) \rightarrow 1$ gives

$$f_{000}(0, 0, s) = \int \frac{k^2 dk}{2\pi^2} j_0(ks) = \frac{1}{4\pi s^2} \delta_{\text{D}}^{[1]}(s). \quad (42)$$

This is simply a representation of the 3D Dirac delta function with spherical symmetry, expected since $f_{000}(0, 0, s) = \xi(s)$.

G1	G2	G3	\mathcal{E}_G
1	2	3	1
1	3	2	-1
2	3	1	1
2	1	3	-1
3	1	2	1
3	2	1	-1

Table 1. Explicit forms of the six permutations appearing in the Case I covariance terms. These arise from the various options for contracting density fields in Eq. (38). Each term involves a contraction between \mathbf{r}_{Gi} and \mathbf{r}'_i . We additionally give the Levi-Civita permutation factor \mathcal{E}_G for each.

G1	G2	G3	H1	H2	H3	\mathcal{E}_G	\mathcal{E}_H
1	2	3	1	2	3	1	1
1	2	3	1	3	2	1	-1
1	2	3	2	1	3	1	1
1	2	3	2	3	1	1	-1
1	2	3	3	1	2	1	1
1	2	3	3	2	1	1	-1
2	3	1	1	2	3	1	1
2	3	1	1	3	2	1	-1
2	3	1	2	1	3	1	1
2	3	1	2	3	1	1	-1
2	3	1	3	1	2	1	1
2	3	1	3	2	1	1	-1
3	1	2	1	2	3	1	1
3	1	2	1	3	2	1	-1
3	1	2	2	1	3	1	1
3	1	2	2	3	1	1	-1
3	1	2	3	1	2	1	1
3	1	2	3	2	1	1	-1

Table 2. Explicit forms of the 18 permutations appearing in the Case II covariance terms. These arise from the various options for contracting density fields in Eq. (44), in particular the contraction of $\mathbf{r} + \mathbf{r}_{G1}$ with \mathbf{r}'_0 , \mathbf{r} with $\mathbf{r}'_0 + \mathbf{r}'_{H1}$, $\mathbf{r}_0 + \mathbf{r}_{G2}$ with $\mathbf{r}'_0 + \mathbf{r}'_{H2}$ and $\mathbf{r}_0 + \mathbf{r}_{G3}$ with $\mathbf{r}'_0 + \mathbf{r}'_{H3}$ (noting the symmetry of the final two terms). We additionally give the permutation factors \mathcal{E}_G and \mathcal{E}_H for each.

The other f -integrals can be similarly evaluated in the limit $s \rightarrow 0$ (and again, $P(k) = 1$). We have

$$\lim_{s \rightarrow 0} f_{\ell_{Gi}\ell'_i L}(r_{Gi}, r'_i, s) = \lim_{s \rightarrow 0} \int \frac{k^2 dk}{2\pi^2} j_{\ell_{Gi}}(kr_{Gi}) j_{\ell'_i}(kr'_i) j_L(ks) = \int \frac{k^2 dk}{2\pi^2} j_{\ell_{Gi}}(kr_{Gi}) j_{\ell'_i}(kr'_i) = \frac{1}{4\pi r_{Gi} r'_i} \delta_D^{[1]}(r_{Gi} - r'_i) \delta_{\ell_{Gi}\ell'_i}^K. \quad (43)$$

For the first equality, we have noted that, as $s \rightarrow 0$, only j_0 is non-zero, meaning $L \rightarrow 0$ and hence $\ell \rightarrow \ell'$ due to the 3- j symbol in equation (41). We recognize this integral as a Dirac delta function, as before.

As shown in Fig. 4, this result implies that, in the limit of uniform power spectra, the covariance for two tetrahedra is non-vanishing only when (1) they have zero separation length and one of their vertices is coincident and (2) their sides are the same lengths; *i.e.* when one tetrahedron can be perfectly rotated in 3D to overlap with the other.

Case II Here, we consider sets of contractions that involve couplings between primary vertices and endpoints across the two families. Each is of the form

$$\begin{aligned} I_{II}(\mathbf{R}, \mathbf{R}'; \mathbf{s}) &\equiv \langle \delta(\mathbf{x} + \mathbf{r}_i) \delta(\mathbf{x} + \mathbf{s} + \mathbf{r}'_0) \rangle \langle \delta(\mathbf{x}' + \mathbf{r}_0) \delta(\mathbf{x}' + \mathbf{s} + \mathbf{r}'_{i'}) \rangle \Big|_{r_0=r'_0=0} \\ &\quad \times \langle \delta(\mathbf{x}'' + \mathbf{r}_j) \delta(\mathbf{x}'' + \mathbf{s} + \mathbf{r}'_{j'}) \rangle \langle \delta(\mathbf{x}''' + \mathbf{r}_k) \delta(\mathbf{x}''' + \mathbf{s} + \mathbf{r}'_{k'}) \rangle \\ &= \sum_{G,H} \xi(\mathbf{s} - \mathbf{r}_{G1}) \xi(\mathbf{s} + \mathbf{r}'_{H1}) \xi(\mathbf{s} - \mathbf{r}_{G2} + \mathbf{r}'_{H2}) \xi(\mathbf{s} - \mathbf{r}_{G3} + \mathbf{r}'_{H3}), \end{aligned} \quad (44)$$

where $\{i, j, k\}$ and $\{i', j', k'\}$ are permutations of the set $\{1, 2, 3\}$. We write the two sets of the permutations as $\{i, j, k\} = \{G1, G2, G3\}$, $\{i', j', k'\} = \{H1, H2, H3\}$, where one set follows a cyclic permutation, due to the explicit contraction with the primary vertex. Given the symmetry among the pair ordering, *i.e.* $\{j, j'\} \leftrightarrow \{k, k'\}$, we can always fix the permutation of one set of endpoints and let the other set explore all permutations. Here we choose G to follow cyclic permutation (giving rise to a factor of three), with H being a standard permutation including six terms. In total, there are 18 permutations in this scenario. For clarity, we write them explicitly in Table 2. As before, the primary vertices at \mathbf{r}_0 and \mathbf{r}'_0 are not permuted.

Including the basic covariance elements, we can write:

$$\begin{aligned}
I_{\text{II}}(\mathbf{R}, \mathbf{R}'; \mathbf{s}) &= \sum_{G,H} (4\pi)^{3/2} \sum_{\ell_{G_1 L_1}} f_{\ell_{G_1 0 \ell_{G_1}}}(r_{G_1}, 0, s) \mathcal{D}_{\ell_{G_1 0 \ell_{G_1}}}^{\text{P}} \mathcal{C}_{000}^{\ell_{G_1 0 \ell_{G_1}}} \mathcal{P}_{\ell_{G_1 0 \ell_{G_1}}}(\hat{\mathbf{r}}_{G_1}, 0, \hat{\mathbf{s}}) \\
&\times (4\pi)^{3/2} \sum_{\ell'_{H_1 L_1}} (-1)^{\ell'_{H_1}} f_{0 \ell'_{H_1} \ell'_{H_1}}(0, r'_{H_1}, s) \mathcal{D}_{0 \ell'_{H_1} \ell'_{H_1}}^{\text{P}} \mathcal{C}_{000}^{0 \ell'_{H_1} \ell'_{H_1}} \mathcal{P}_{0 \ell'_{H_1} \ell'_{H_1}}(0, \hat{\mathbf{r}}'_{H_1}, \hat{\mathbf{s}}) \\
&\times \prod_{i=2}^3 (4\pi)^{3/2} \sum_{\ell_{G_i} \ell'_{H_i} L_i} i^{-\ell_{G_i} + \ell'_{H_i} + L_i} f_{\ell_{G_i} \ell'_{H_i} L_i}(r_{G_i}, r'_{H_i}, s) \mathcal{D}_{\ell_{G_i} \ell'_{H_i} L_i}^{\text{D}} \mathcal{C}_{000}^{\ell_{G_i} \ell'_{H_i} L_i} \mathcal{P}_{\ell_{G_i} \ell'_{H_i} L_i}(\hat{\mathbf{r}}_{G_i}, \hat{\mathbf{r}}'_{H_i}, \hat{\mathbf{s}}), \quad (45)
\end{aligned}$$

where the collection of angular momenta is $\mathcal{L}_G = \{\ell_{G_1}, 0, \ell_{G_2}, \ell_{G_3}\}$, $\mathcal{L}'_H = \{0, \ell'_{H_1}, \ell'_{H_2}, \ell'_{H_3}\}$, and $\Lambda'' = \{\ell_{G_1}, \ell'_{H_1}, L_2, L_3\}$.

To restore the canonical ordering for $\hat{\mathbf{R}}_G = \{\hat{\mathbf{r}}_{G_1}, \hat{\mathbf{r}}_{G_2}, \hat{\mathbf{r}}_{G_3}\}$ and $\hat{\mathbf{R}}'_H = \{\hat{\mathbf{r}}'_{H_1}, \hat{\mathbf{r}}'_{H_2}, \hat{\mathbf{r}}'_{H_3}\}$, we use again the reordering coefficients, in the form

$$\mathcal{B}_{\mathcal{L}_G, J}^{G^{-1}} = (-1)^{\Sigma(\Lambda)(1-\varepsilon_G)/2} \prod_{i=1}^3 \delta_{j_i \ell_{G_i-1}}^{\text{K}}, \quad \mathcal{B}_{\mathcal{L}'_H, J'}^{H^{-1}} = (-1)^{\Sigma(\Lambda')(1-\varepsilon_H)/2} \prod_{i=1}^3 \delta_{j'_i \ell'_{H_i-1}}^{\text{K}}. \quad (46)$$

Since we restrict G to cyclic permutations, $\mathcal{B}_{\mathcal{L}_G, J}^{G^{-1}}$ is merely a Kronecker delta with a trivial phase. Additionally, the phase factor $\Sigma(\Lambda')$ does not play a role for even parity Λ , but is of importance for odd-parity Λ .

As before, we proceed by performing a rotational average over $d\mathcal{R}$, $d\mathcal{R}'$, and $d\mathcal{S}$, which leads to a generalized Gaunt integral, involving two 9- j symbols, and a sum over intermediate angular momenta. As before, the presence of zero angular momenta simplifies the intermediate coefficients, such that $\ell_{12} = \ell_{G_1}$, $\ell'_{12} = \ell'_{H_1}$, and consequently, $\ell'_{12} \equiv L_1$. We do not need to consider permutation of the angular momenta L because their allowed range is fixed once the unprimed ℓ_i and the primed angular momenta ℓ'_i are explicitly given (due to the triangular inequality). With these considerations, the generalized Gaunt integral for $N = 4$ can be simplified as:

$$\begin{aligned}
\mathcal{G}^{\mathcal{L}_G \mathcal{L}'_H \Lambda''} &= (4\pi)^{-2} (\mathcal{D}_{\ell_{G_1} \ell'_{H_1} 0}^{\text{P}})^2 \prod_{i=1}^3 \left[\mathcal{D}_{\ell_{G_i} \ell'_{H_i} L_i}^{\text{P}} \right] \mathcal{C}_{000}^{\ell_{G_1} 0 \ell_{G_1}} \mathcal{C}_{000}^{0 \ell'_{H_1} \ell'_{H_1}} \mathcal{C}_{000}^{\ell_{G_2} \ell'_{H_2} L_2} \mathcal{C}_{000}^{\ell_{G_3} \ell'_{H_3} L_3} \\
&\times \begin{Bmatrix} \ell_{G_1} & 0 & \ell_{G_1} \\ 0 & \ell'_{H_1} & \ell'_{H_1} \\ \ell_{G_1} & \ell'_{H_1} & L_1 \end{Bmatrix} \begin{Bmatrix} \ell_{G_1} & \ell_{G_2} & \ell_{G_3} \\ \ell'_{H_1} & \ell'_{H_2} & \ell'_{H_3} \\ L_1 & L_2 & L_3 \end{Bmatrix} \\
&= (4\pi)^{-2} (-1)^{\ell_{G_1} + \ell'_{H_1}} \mathcal{D}_{\ell_{G_2} \ell'_{H_2} L_2}^{\text{P}} \mathcal{D}_{\ell_{G_3} \ell'_{H_3} L_3}^{\text{P}} \mathcal{C}_{000}^{\ell_{G_2} \ell'_{H_2} L_2} \mathcal{C}_{000}^{\ell_{G_3} \ell'_{H_3} L_3} \begin{Bmatrix} \ell_{G_1} & \ell_{G_2} & \ell_{G_3} \\ \ell'_{H_1} & \ell'_{H_2} & \ell'_{H_3} \\ L_1 & L_2 & L_3 \end{Bmatrix}, \quad (47)
\end{aligned}$$

where the first 9- j symbol yields a factor of $(\mathcal{D}_{\ell_{G_1} \ell'_{H_1} 0}^{\text{P}})^{-2}$. The two 3- j symbols involving zero angular momentum get cancelled with $\mathcal{D}_{\ell_{G_1} \ell'_{H_1} 0}^{\text{P}}$, giving rise to an overall phase factor.

From the definition of the coefficients we find

$$\mathcal{D}_{\Lambda''}^{\text{P}} \mathcal{C}_0^{\Lambda''} = (-1)^{L_1} \sqrt{(2\ell_{G_1} + 1)(2\ell'_{H_1} + 1)(2\ell''_1 + 1)(2\ell''_2 + 1)(2\ell''_3 + 1)} \times \mathcal{C}_{000}^{\ell_{G_1} \ell'_{H_1} L_1} \mathcal{C}_{000}^{L_1 L_2 L_3}. \quad (48)$$

We proceed by combining Eqs. (46-48), inserting these expressions into the definition of the covariance, and projecting out the coefficients proportional to $\mathcal{P}_{\Lambda}(\hat{\mathbf{R}})$ and $\mathcal{P}_{\Lambda'}(\hat{\mathbf{R}}')$. Noting that $\ell_{G_1} + \ell'_{H_1} + L_1$ must be an even integer (else $\mathcal{C}_{000}^{\ell_{G_1} \ell'_{H_1} L_1}$ is zero), this factor can be dropped from the overall phase. Altogether we arrive at the final form for Case II:

$$\begin{aligned}
\text{Cov}_{\Lambda, \Lambda'}^{(\text{fc}), \text{II}}(R, R') &= (4\pi)^4 \sum_{G,H} (-1)^{\Sigma(\Lambda')(1-\varepsilon_H)/2} \sum_{L_1 L_2 L_3} \mathcal{D}_{L_1 L_2 L_3}^{\text{P}} \mathcal{C}_{000}^{L_1 L_2 L_3} \begin{Bmatrix} \ell_{G_1} & \ell_{G_2} & \ell_{G_3} \\ \ell'_{H_1} & \ell'_{H_2} & \ell'_{H_3} \\ L_1 & L_2 & L_3 \end{Bmatrix} \\
&\times \prod_{i=1}^3 \left[(-1)^{(-\ell_{G_i} - \ell'_{H_i} + L_i)/2} \mathcal{D}_{\ell_{G_i} \ell'_{H_i} L_i}^{\text{P}} \mathcal{C}_{000}^{\ell_{G_i} \ell'_{H_i} L_i} \right] \\
&\times \int \frac{s^2 ds}{V} f_{\ell_{G_1} 0 \ell_{G_1}}(r_{G_1}, 0, s) f_{0 \ell'_{H_1} \ell'_{H_1}}(0, r'_{H_1}, s) f_{\ell_{G_2} \ell'_{H_2} L_2}(r_{G_2}, r'_{H_2}, s) f_{\ell_{G_3} \ell'_{H_3} L_3}(r_{G_3}, r'_{H_3}, s). \quad (49)
\end{aligned}$$

As before, if we take the limit that the 2PCF is a Dirac delta function, $\xi(\mathbf{s} - \mathbf{r}_{G_1}) \rightarrow \delta_{\text{D}}^{[3]}(\mathbf{s} - \mathbf{r}_{G_1})$ implies the limit $\mathbf{s} \rightarrow \mathbf{r}_{G_1}$. Recalling $P(k) = 1$, the f -integral associated with the second correlation function becomes

$$\lim_{\mathbf{s} \rightarrow \mathbf{r}_{G_1}} f_{0 \ell'_{H_1} \ell'_{H_1}}(0, r'_{H_1}, s) = \lim_{\mathbf{s} \rightarrow \mathbf{r}_{G_1}} \int \frac{k^2 dk}{2\pi^2} j_{\ell}(kr_{G_1}) j_{\ell}(kr'_{H_1}) = \frac{1}{4\pi r_{G_1} r'_{H_1}} \delta_{\text{D}}^{[1]}(r_{G_1} - r'_{H_1}). \quad (50)$$

In addition, we have $\mathbf{s} \rightarrow \mathbf{r}_{G_i} - \mathbf{r}'_{H_i}$ for $i = 2, 3$. In this case, the resulting integral of three spherical Bessel functions can be simplified using Eq. (3.21) of Mehrem et al. (1991), which we do not duplicate here. However, the former work shows the result

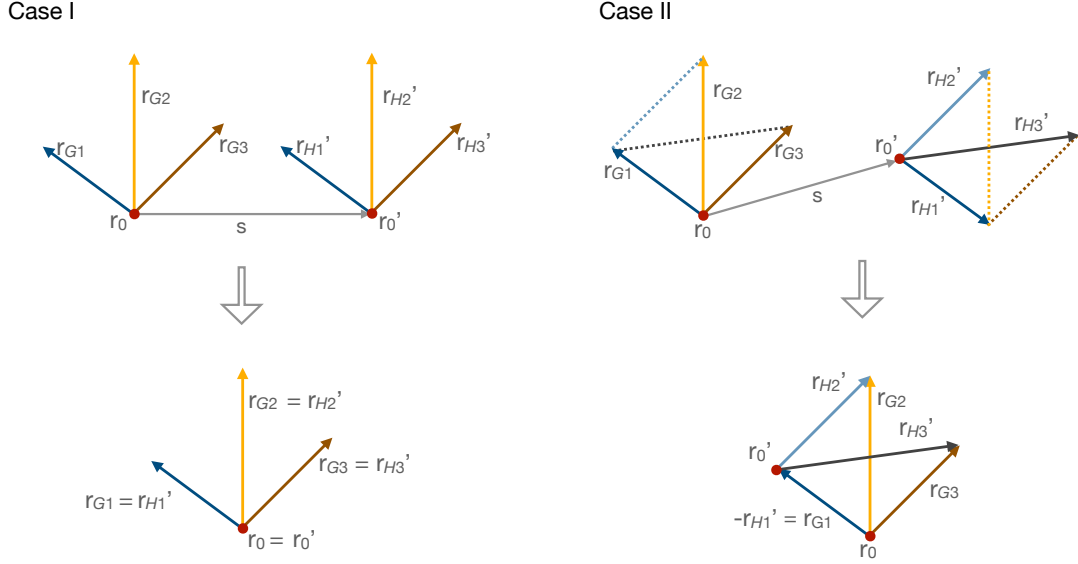


Figure 4. Covariance calculation for the 4PCF in the limit of zero separation (*i.e.* where ξ becomes a Dirac delta function). **Left column:** In Case I, this limit implies that the two tetrahedra overlap at their origin with $\mathbf{s} \rightarrow 0$, $\mathbf{r}'_1 \rightarrow \mathbf{r}_{G1}$, $\mathbf{r}'_2 \rightarrow \mathbf{r}_{G2}$, and $\mathbf{r}'_3 \rightarrow \mathbf{r}_{G3}$. **Right column:** the same limit in Case II implies that the two tetrahedra also overlap but with one of the primary vertices sitting on an endpoint from the other family. Consequently, we find $\mathbf{s} \rightarrow \mathbf{r}_{G1}$, $\mathbf{s} \rightarrow -\mathbf{r}'_{H1}$, $\mathbf{s} \rightarrow \mathbf{r}'_{H2} - \mathbf{r}_{G2}$, and $\mathbf{s} \rightarrow \mathbf{r}'_{H3} - \mathbf{r}_{G3}$.

to be zero unless the three vectors \mathbf{s} , \mathbf{r}_{Gi} , and \mathbf{r}'_{Hi} form a closed triangle, coinciding with our delta function assumption.⁶ This result is unsurprising because the Dirac delta function can be written as an integral of a product of spherical Bessel functions. It is interesting to consider the physical picture (cf. Fig. 4). When the correlation functions approach delta functions in case II, the two tetrahedra also overlap but with their primary vertices sitting on the endpoint of that side, in particular, that side of the tetrahedra must have the same length as the separation vector of each family.

Notably, Case I and Case II have similar mathematical structure, with essentially no differences induced by distinguishing between the primary vertices and the endpoints. Combining both cases allows us to recover the general form (cf. Eq. 36) including all $4! = 24$ permutation terms.⁷

5 NUMERICAL IMPLEMENTATION AND COMPARISON WITH SIMULATIONS

5.1 Implementation of the connected covariance

The ingredients for the analytic covariance calculation from Eq. (36) comprise the f -integrals, a set of coefficients including the product of \mathcal{D}_Λ^P , Wigner 3- j , Wigner 9- j symbols, and the phase. In practice, we compute all these elements using PYTHON. For efficiency, with the evaluation of the Wigner 3- j and 9- j symbols performed using the SYMPY package. We pre-compute the f -integrals for each radial bin, as well as the coupling coefficients, before assembling the covariance. These are stored in dictionary format and loaded during the calculation. To compute the f -integral, which involves fine binning in k and s , we use an analytic form for the bin-averaged spherical Bessel functions (cf. Eq. D2), which is exact and speeds up the implementation. We use 5,000 points in $k \in [10^{-4}, 5] \text{ Mpc}^{-1}h$ and 4,100 points in $s \in [10^{-5}, 10^3] h^{-1} \text{ Mpc}$ with both linearly spaced. We choose these ranges and grid sizes such that on the one hand, the arrays fit in the same memory block managed by NUMPY, and on the other hand, they cover the integration range of interest with sufficiently small grid size. Given that our aim is to measure the 4PCF up to $\ell_{\max} = 4$, we compute the f -integrals up to $\ell = 8$ (considering $L = \ell + \ell'$). To verify the numerical evaluation and implementation of the bin-averaged f -integral, we compared the resulting forms to an analytic solution for the integral of a product of three spherical Bessel functions (Fabrikant 2013), modified to accommodate for the bin-averaging. This is discussed in Appendix D.

⁶ For a similar discussion for the 3PCF covariance of the limit that ξ becomes a Dirac delta function, see §6.3 in Slepian & Eisenstein 2015a.

⁷ We additionally note that all the above derivations could be performed in the spherical harmonics basis and would have the same results. We will not repeat this derivation here.

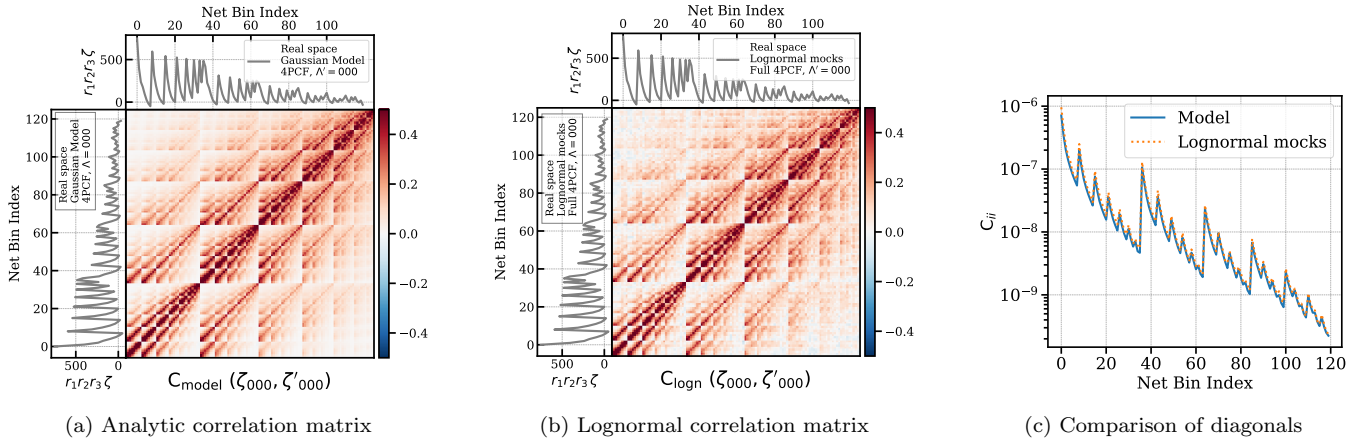


Figure 5. Comparison of the analytic and sample covariance matrices for a set of lognormal simulations. The first and second panels show the comparison of the correlation matrix (defined by $M_{ij} = C_{ij}/\sqrt{C_{ii}C_{jj}}$) for angular momenta $\{\Lambda, \Lambda'\} = \{000, 000\}$ in real space. Fig. 5a gives the model prediction for the fully-coupled 4PCF correlation matrix, and the panels above and to the left show the (disconnected) Gaussian 4PCF model in real space. The horizontal and vertical axes indicate 120 radial bins, ordered so that $r_1 < r_2 < r_3$. This gives rise to the block structure in the matrix and the saw-tooth shape of the correlation functions. Fig. 5b shows the correlation matrix estimated from 1,000 lognormal mocks, with the extended panels showing the measured full 4PCF for the lognormal mocks in real space. Fig. 5c shows a comparison of the diagonal elements of the two covariance matrices; we note the values (vertical axis) are logarithmically scaled.

5.2 Comparison with lognormal simulations

We now compare theoretical covariance to those extracted from simulations. First, we use a set of 1,000 lognormal mocks at redshift $z = 2$ with a number density of $\sim 1.5 \times 10^{-4} [h^{-1}\text{Mpc}]^{-3}$ and volume $V = 3.9 [\text{Gpc}/h]^3$.⁸ The lognormal mocks are generated using NBODYKIT (Hand et al. 2018), where the overdensity fields are evolved according to the Zel'dovich approximation (zeroth-order Lagrangian perturbation theory) (Schneider & Bartelmann 1995). We prepare mocks in both real- and redshift space in order to investigate the impact of RSD on the covariance. The input linear power spectrum is generated with the cosmological parameters $\{\Omega_m, \Omega_b h^2, h, n_s, \sigma_8\} = \{0.31, 0.022, 0.676, 0.97, 0.8\}$ with a linear bias $b_1 = 1.8$. The 4PCFs are measured using the ENCORE code⁹ at 10 radial bins centered at $r_{\text{bin}} = \{27, 41, \dots, 153\} h^{-1}\text{Mpc}$ with a bin width of $14 h^{-1}\text{Mpc}$. In this setup, these lognormal mocks have a low level of non-Gaussianity due to the high redshift and have a relatively high shot noise.

The sample covariance estimated from mock simulations is defined as

$$C_{\text{mock}} = \frac{1}{N_{\text{mock}} - 1} \sum_{i=1}^{N_{\text{mock}}} (\zeta^{(i)} - \bar{\zeta}) (\zeta^{(i)} - \bar{\zeta})^T, \quad (51)$$

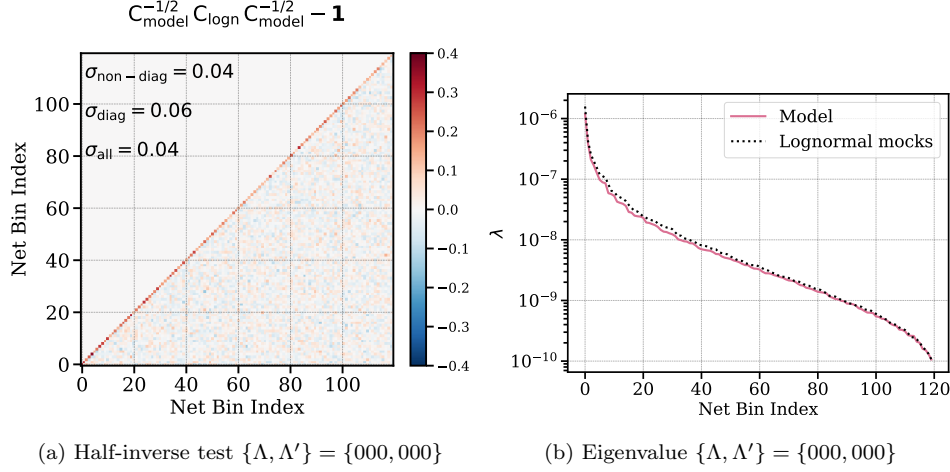
where the data vector $\zeta^{(i)}$ (with dimension N_{bins}) is the 4PCF measured from the i -th mock simulation, and $\bar{\zeta}$ is the mean over all N_{mock} realizations. Since the mean is estimated from the mocks themselves, the definition includes the prefactor $(N_{\text{mock}} - 1)^{-1}$.

When computing the f -integrals in real space, we use the same input power spectrum that was used to generate the lognormal mocks. In redshift space the power spectrum is additionally multiplied by the isotropic Kaiser factor $(b^2 + 2fb/3 + f^2/5)/b^2$, with f being the logarithmic derivative with respect to scale factor of the linear growth rate (Kaiser 1987). In both cases, we damp the power spectra by $\exp(-(k/k_0)^2)$ to avoid numerical issues, setting $k_0 = 1 [\text{Mpc}^{-1} h]$. We find that the shot noise term is sensitive to the precise form of exponential damping function. For the lognormal mocks, which feature a large shot noise, we observe better agreement between theory and simulations when the shot noise damping is not included.

Fig. 5 shows a comparison between the theoretical and sample covariance from the lognormal mocks for angular momenta $\{\Lambda, \Lambda'\} = \{000, 000\}$ in real space. The 2D plot in the first panel shows the model prediction for the fully-coupled 4PCF correlation matrix M , where the correlation matrix is the covariance matrix C normalized by its diagonal terms, *i.e.* $M_{ij} = C_{ij}/\sqrt{C_{ii}C_{jj}}$. We arrange the radial bins in the following manner: we start by fixing bins in r_1 and r_2 and loop over r_3 , then move to the next radial bin in r_2 at the same fixed r_1 and again loop over r_3 , before move to the next bin in r_1 . This is repeated until all possible radial binning combinations are explored; this specific way of arranging the bins is denoted as the net bin

⁸ While it may seem more prudent to construct simulations that match our assumption of Gaussianity, this is non-trivial, since we require a discrete density field. In principle, one could use a set of discrete particles which are assigned the Gaussian random field value as weights. However, this approach does not reproduce covariance correctly, since it puts multiple galaxies at the same position and effectively enhances the shot noise.

⁹ <https://github.com/oliverphilcox/encore>


 (a) Half-inverse test $\{\Lambda, \Lambda'\} = \{000, 000\}$

 (b) Eigenvalue $\{\Lambda, \Lambda'\} = \{000, 000\}$

Figure 6. **Left panel:** half-inverse test comparing the lognormal simulations and the analytic covariance, both of which are shown in Fig. 5. If the covariance matrices agree, both the mean and the off-diagonal elements should be noisy fluctuations around zero. For clarity, we plot only the lower triangle, and give the standard deviation for the off-diagonal elements, $\sigma_{\text{non-diag}}$, for the diagonal elements, σ_{diag} , and for all elements combined, σ_{all} . **Right panel:** comparison between the eigenvalues of the analytic covariance (solid curve) and lognormal mock covariance (dotted curve).

index. During this process we force the radial bin arrangement to be $r_1 < r_2 < r_3$. In total, we have $C_{10}^3 = 10!/(7!3!) = 120$ radial bins. The radial bin arrangement also leads to the block structure in the covariance matrix.

The second panel of Fig. 5 shows the measurement from 1000 lognormal mocks in real space with the inset showing the measurements of the full 4PCF from Gaussian mocks. Comparing the first and the second panel, we can see that the analytic covariance is able to capture the off-diagonal features. The covariance for $\{\Lambda, \Lambda'\} = \{000, 000\}$ is mostly positive as a result of the auto-covariance for the angular momenta themselves. The third panel shows a comparison of the diagonal elements of these two matrices in log-scale. The extended panels at the top and right of the first panel in Fig. 5a show the Gaussian 4PCF model in real space, where the (disconnected) Gaussian 4PCF consists of a product of two 2PCF (see appendix A in Philcox et al. (2021b) for a derivation). Since the 2PCF is approximately given by a declining power law, combination with our radial bin arrangement leads to the saw-tooth shape of the 4PCF. The extended panels at the top and right of the second panel of Fig. 5b are the measured *full* 4PCF (includes both connected and disconnected term) in real space. They both assist the visualization of the block structure of the correlation matrices.

In order to quantify the similarity between the Gaussian model prediction and the mock measurements, we perform a test, which we label as ‘the half-inverse test’. This considers the matrix

$$\mathbf{S} \equiv \mathbf{C}_{\text{model}}^{-1/2} \mathbf{C}_{\text{mock}} \mathbf{C}_{\text{model}}^{-1/2} - \mathbf{1}, \quad (52)$$

where $\mathbf{1}$ is the identity matrix. If the two covariances were identical \mathbf{S} which would vanish (Deadman et al. 2013). Fig. 6 shows the half-inverse test in the left panel, with the eigenvalues of the 4PCF covariance inferred from the model (solid blue curve) and the mocks (dotted black curve) shown in the right panel. If the analytic and sample covariance matrices agree, the half-inverse matrix should follow a Wishart distribution (Wishart 1928; Anderson 2009) and we expect the standard deviation of half-inverse matrix elements to scale as $1/\sqrt{N_{\text{mock}}} \sim 0.03$, where $N_{\text{mock}} = 1,000$ is the number of mocks. The standard deviation of the diagonal elements should be two times larger than that of the off-diagonal ones, since the expression for the variance of a Wishart distribution contains a Kronecker delta for matrix elements $i = j$.

For the lognormal mocks, the mean of the half-inverse matrix elements is $\langle \mathbf{S} \rangle = 2.3 \times 10^{-3}$, much smaller than their standard deviation. However, we observe a residual in the diagonal terms; indeed, the mean of these is 0.180. If we decompose the theoretical covariance into its diagonal eigenvalue matrix \mathbf{D} and a unitary matrix \mathbf{V} of eigenvectors, we can write $\mathbf{C}_{\text{model}}^{-1/2} = \mathbf{V} \mathbf{D}^{-1/2} \mathbf{V}^{-1}$. If the eigenbasis of the analytic covariance is close enough to the mock-estimated one, the half-inverse test reduces to the ratio between the eigenvalues of the two covariances. Here, we see that the eigenvalues of the model covariance are slightly lower than those of the mock covariance. A possible explanation for this residual is that the lognormal mocks have intrinsically high shot noise, which can generate non-Gaussian (but Poissonian) terms in the covariance that require modeling beyond the Gaussian approximation. Another possibility arises from the choice of input power spectrum. Here, we used the power spectrum which generated the lognormal mock, instead of that measured from the lognormal mocks. Due to the lognormal transformation of the density fields, and post Zel’dovich evolution, the two spectra could differ slightly.

Fig. 7 is similar to Fig. 5, but shows a comparison between the two sets of covariances in redshift space. Compared to the real space correlation matrix, we see that RSD slightly enhances the off-diagonal structure for $\{\Lambda, \Lambda'\} = \{000, 000\}$. The agreement in the diagonal elements and the half-inverse test are of the similar level compared to the real space test, with

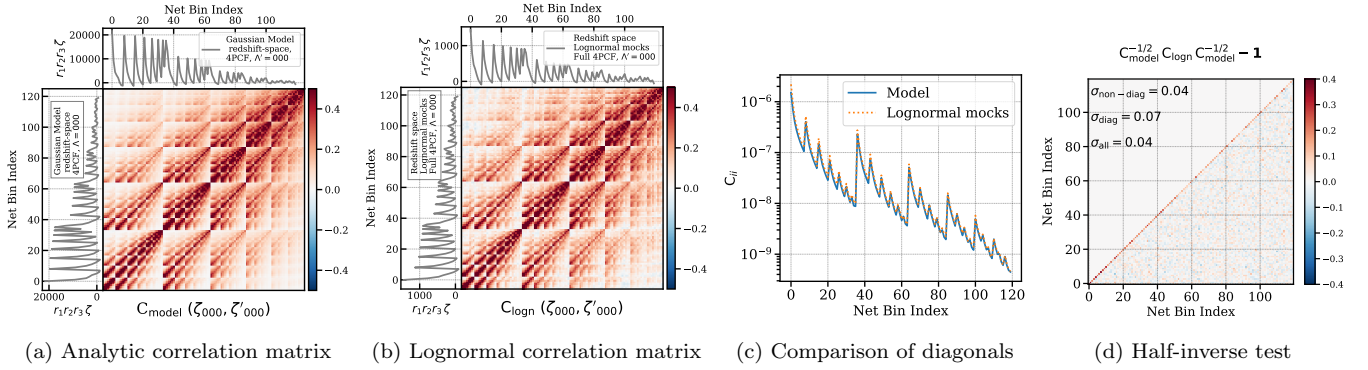


Figure 7. As Fig. 5, but comparing the analytic and lognormal covariances in redshift space. Fig. 7 gives the results of the half-inverse test in the same format as Fig. 6a. The model also works well in redshift space in that it shows comparable coupling structure for the correlation matrices and the diagonal elements of the covariances. However, we do observe a residual in the diagonal elements of the matrix for the half-inverse test.

similar diagonal residual found in the half-inverse test as well. Although our numerical implementation of the 4PCF covariance ignores higher order angular momentum contribution arising from RSD,¹⁰ this comparison shows that the RSD effect can be largely accounted for by simply modeling the covariance using an input power spectrum equal to the RSD monopole. Finally, we note that the RSD doubles the amplitude of the Gaussian 4PCF model and the full 4PCF measured from the mocks in the extended panels of Fig. 7a and Fig. 7b. These quantities are dominated by the two-point statistics and the increase in the amplitude is approximately given by the Kaiser factor to the fourth power.

5.3 Comparison with Quijote simulations

To further understand the non-Gaussianity arising from gravitational evolution and to test the validity of our Gaussian assumption, we compare the theoretical covariance formalism to the sample covariance measured from the QUIJOTE halo catalogues.¹¹ Each of the QUIJOTE simulations has a box size of $V = 1.0 [h^{-1} \text{Gpc}]^3$, a fiducial cosmology $\{\Omega_m, \Omega_b, h, n_s, \sigma_8\} = \{0.3175, 0.049, 0.6711, 0.9624, 0.834\}$, zero neutrino mass, and is at redshift $z = 0.5$ (Villaescusa-Navarro et al. 2020).

We test our algorithm on 100 QUIJOTE halo catalogues created from $1,024^3$ cold dark matter (CDM) particles. Halos are identified using a particle number cut $N_{\text{particle}} > 150$ per halo, which corresponds to $M_{\text{cut}} = 1.2 \times 10^{13} [h^{-1} M_\odot]$. This gives two times lower shot noise compared to the lognormal mocks. As before, the catalogues are prepared both in real and redshift space, and we use the same radial binning. The f -integral is constructed from the power spectrum monopole measured from the QUIJOTE halo catalogues for both real and redshift space. For this set of simulations we applied exponential damping to both the power spectrum and shot noise.

Fig. 8 shows a comparison for $\{\Lambda, \Lambda'\} = \{000, 000\}$ in real space. Again, we see a positive matrix, but this time with an enhanced off-diagonal feature, due to the lower shot noise (approximately less by a factor of two than that of the lognormal mocks). Fig. 9 gives a comparison for the cross order $\{\Lambda, \Lambda'\} = \{000, 101\}$ in real space. Again, the analytic correlation matrix is able to capture the features in the off-diagonal elements seen in the mocks. The overall negative structure in the correlation matrix is due to the anti-correlation between the 4PCF ζ_{000} and ζ_{101} . Since we correlate two different angular distributions we expect the structure of the covariance to be asymmetric. The right panel shows the diagonal elements of the cross covariance for the theoretical model and the QUIJOTE simulation; here, the model covariance slightly underpredicts the covariance diagonal at the small scales seen at the peaks of the saw-tooth shape, but overall the ratio between the sample and mock covariance oscillates around unity with a mean $\langle C_{ii}^{\text{mock}} / C_{ii}^{\text{model}} \rangle \sim 0.96$.

To quantify the similarity between the model predictions and simulations, we again utilize the half-inverse test. The left panel in Fig. 10 shows the results for $\{\Lambda, \Lambda'\} = \{000, 000\}$, while the right panel shows $\{\Lambda, \Lambda'\} = \{000, 101\}$, both of which are in real space. In order to invert the cross covariance, we build a full matrix which includes the auto-covariance $\{\Lambda, \Lambda'\} = \{000, 000\}$ and $\{\Lambda, \Lambda'\} = \{101, 101\}$, which doubles the size of the matrix. In this case, we do not observe any residuals in the diagonal of the matrix. Given 100 halo catalogues, the standard deviation is expected to be of order $1/\sqrt{100} = 0.1$, matching that found from the data.

In addition we also perform a comparison for $\{\Lambda, \Lambda'\} = \{000, 101\}$ in redshift space, shown in Fig. 11. Compared to the real space, RSD enhances the diagonals by a factor of ~ 2.3 for this cross covariance term, but its overall shape is almost unaffected. From the right panel, we see that the diagonal elements of the theoretical covariance slightly under-predict those

¹⁰ See Appendix E for a more rigorous treatment of this effect

¹¹ <https://quijote-simulations.readthedocs.io/en/latest/halos.html>

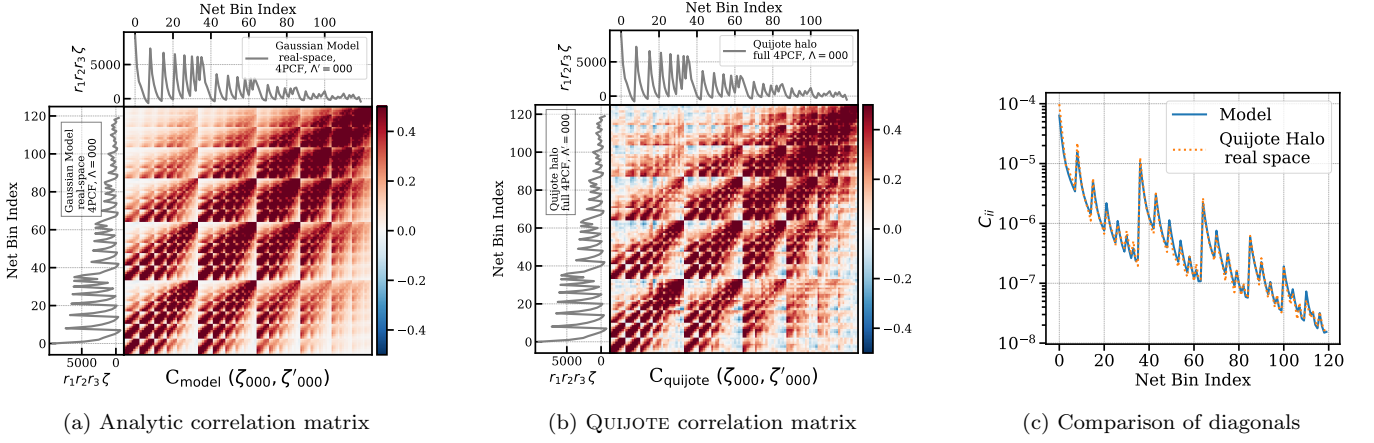


Figure 8. As Fig. 5, but for QUIJOTE halo catalogue in real space, using 1,000 simulations. For the simulations with non-negligible non-Gaussianity, the model can adequately predict various features of the correlation matrix, with a good match for the diagonal elements of the covariance as well.

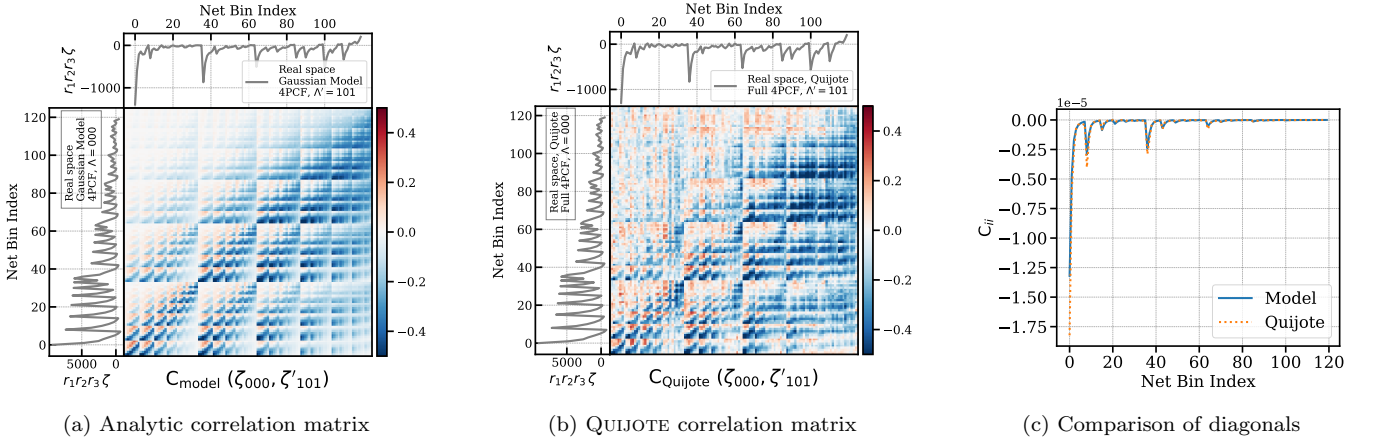


Figure 9. As Fig. 5, but for QUIJOTE halo catalogue in real space. Here, we plot the cross-covariance with angular momenta $\{\Lambda, \Lambda'\} = \{000, 101\}$.

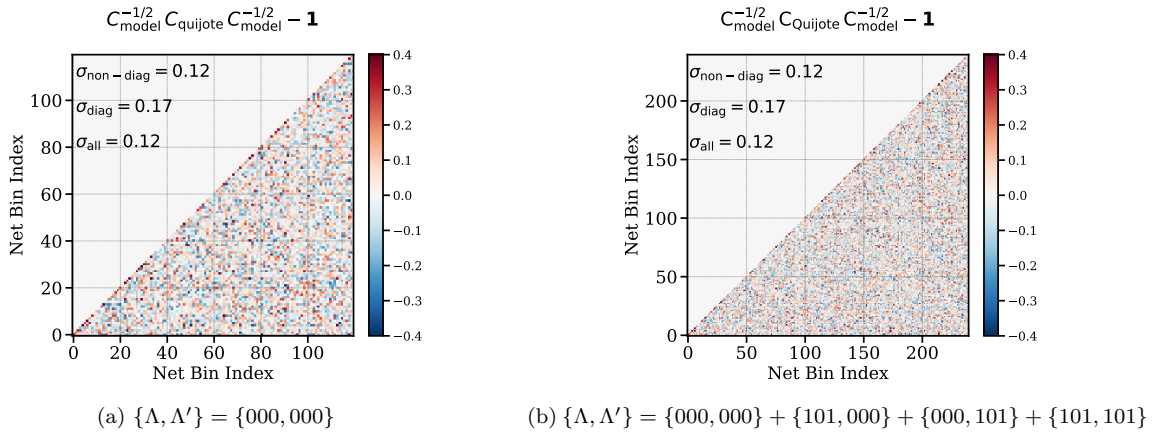


Figure 10. Half-inverse test for the analytic covariance and sample covariance of the QUIJOTE halo catalogue in real space, in the format of Fig. 6a. **Left panel:** angular momenta $\{\Lambda, \Lambda'\} = \{000, 000\}$. **Right panel:** cross-covariance with angular momenta $\{\Lambda, \Lambda'\} = \{000, 101\}$. For comparison we show the full matrix with $\{\Lambda, \Lambda'\} = \{000, 000\} + \{000, 101\} + \{101, 000\} + \{101, 101\}$. The standard deviations for respectively the off-diagonal elements, $\sigma_{\text{non-diag}}$, the diagonal elements, σ_{diag} , and all the elements, σ_{all} , are given in the insets.

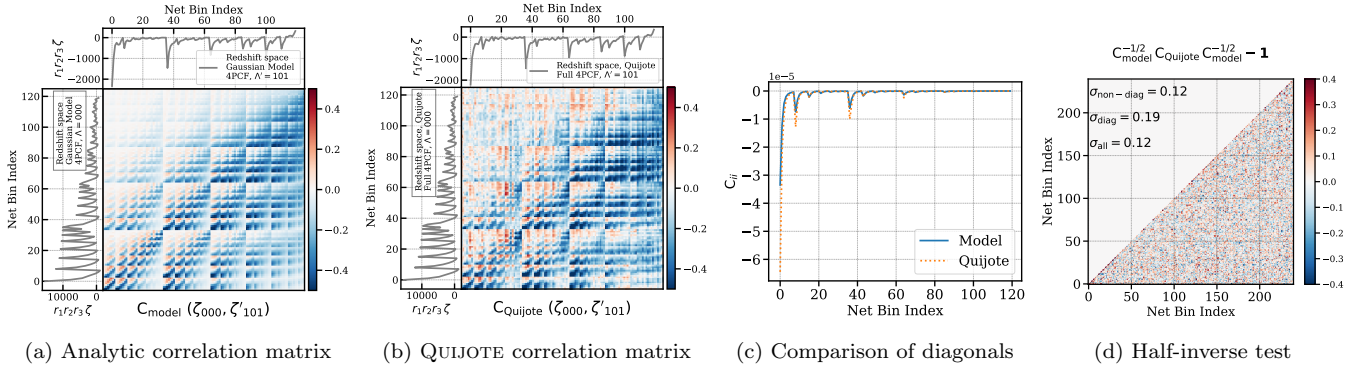


Figure 11. As Fig. 7, but for QUIJOTE halo catalogue with angular momenta $\{\Lambda, \Lambda'\} = \{000, 101\}$ including RSD. The analytic covariance well describes the structure of the sample covariance in this scenario.

estimated from QUIJOTE simulation at small scales, but the mean of the ratio is close to unity, with $\langle C_{ii}^{\text{mock}}/C_{ii}^{\text{model}} \rangle \sim 1.04$. This is also demonstrated in panel (d), showing no residual from the half-inverse test. In principle, we could extend our model to include RSD effects as described in Appendix E; we leave this effort to future work.

5.4 Comparison with the MultiDark-Patchy mocks

Finally, to test the impact of the non-uniform survey geometry, we compare our Gaussian covariance model to a set of MULTIDARK-PATCHY mocks (Kitaura et al. 2016; Rodríguez-Torres et al. 2016) produced for the Sloan Digital Sky Survey (SDSS) Baryon Oscillation Spectroscopic Survey (BOSS) Data Release (DR) 12 (Dawson et al. 2013; Alam et al. 2015). In this test, we focus on the set of PATCHY mocks that match the galaxy clustering of the BOSS Constant Stellar Mass (CMASS) Luminous Red Galaxy (LRG) sample at an effective redshift $z_{\text{eff}} = 0.57$ in the North Galactic Cap (NGC). The mock catalogues were constructed using the *Planck* cosmology $\{\Omega_m, \Omega_b, h, n_s, \sigma_8\} = \{0.307115, 0.048206, 0.6777, 0.9611, 0.8288\}$.

For simulations in a cubic box, the volume, V , entering the theoretical covariance is simply given by the box size, and the number density is the ratio between the number of particles (galaxies or halos) and the volume. For a sample with survey geometry and a radial selection function, we generalize the volume and number density estimator of Wadekar et al. (2020); Putter et al. (2012):

$$V_{\text{eff}} = \frac{[\int d^3r n^4(\mathbf{r}) w^4(\mathbf{r})]^2}{\int d^3r n^8(\mathbf{r}) w^8(\mathbf{r})}, \quad \bar{n}_{\text{eff}} = \frac{\int d^3r n^8(\mathbf{r}) w^8(\mathbf{r})}{\int d^3r n^7(\mathbf{r}) w^8(\mathbf{r})}, \quad (53)$$

where $n(\mathbf{r})$ is the number density of the sample as a function of redshift and $w(\mathbf{r})$ is the galaxy weight (including both systematic and FKP weights (Feldman et al. 1994)). To calculate this, we apply the default weights provided in the PATCHY mocks. These are given by¹²

$$w_{\text{tot}} = w_{\text{fkp}} \cdot w_{\text{veto}} \cdot w_{\text{fiber collision}}, \quad (54)$$

where the FKP weight is $w_{\text{fkp}} = (1 + 10^4 (h^{-1} \text{Mpc})^3 \cdot n(\mathbf{r}))^{-1}$, w_{veto} is a binary indicating whether the object is excluded by veto mask or not, and $w_{\text{fiber collision}}$ is a fiber collision weight. For PATCHY NGC, we obtain $\bar{n} = 3.2 \times 10^{-4} (h^{-1} \text{Mpc})^{-3}$ and $V_{\text{eff}}^{-1} = 1.9 (h^{-1} \text{Gpc})^3$. We caution however that this is only an approximation and does not fully account for the survey geometry, even for the 2PCF covariance (Wadekar et al. 2020).

The input power spectrum is measured from the PATCHY mocks then fitted using the Effective Field Theory of Large Scale Structure (EFT; Carrasco et al. 2012; Baumann et al. 2012) including one-loop bias, RSD, counterterms and infrared resummation (Senatore & Zaldarriaga 2014; Senatore 2015; Ivanov et al. 2020), implemented using the CLASS-PT code (Chudaykin et al. 2020). The 4PCF is measured from 999 PATCHY mocks with random catalogues $50\times$ larger than data, and the same radial binning scheme as before. As above, we apply an exponential damping to the power spectrum and shot noise.

In order to mitigate the window function effect, we further consider an optimization of the effective number density and survey volume. Our motivation is that increasing the number density is an approximate way to incorporate non-Gaussianity and effective volume is a leading order correction of the survey geometry. To compute this, we create a 2D grid of parameters, scanning over both the number density and the effective volume. We maximize a log-likelihood based on the Kullback-Leibler (KL) divergence using the expected Wishart distribution for mock covariances (Kullback & Leibler 1951) following O’Connell et al. (2016); Philcox et al. (2019). This has the advantage that it only requires the analytic covariance to be inverted. The

¹² <http://www.skiesanduniverses.org/page/page-3/page-15/page-9/>

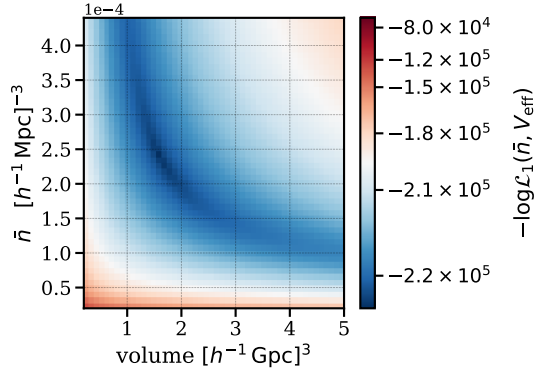


Figure 12. Log-likelihood for the parameters \bar{n} and V_{eff} obtained from fitting the analytic covariance to the sample covariance of 1,000 PATCHY mocks (including redshift-space effects and non-uniform survey geometry). The likelihood is constructed using the KL-divergence, as in Eq. 55.

log-likelihood involves both the Gaussian covariance and the sample covariance measured from PATCHY mocks:

$$-\log \mathcal{L}_1(\bar{n}, V_{\text{eff}}) = \frac{N_{\text{mock}}}{2} [\text{Tr}(\mathbf{C}_{\text{model}}^{-1}(\bar{n}, V_{\text{eff}})\mathbf{C}_{\text{mocks}}) - \log \det \mathbf{C}_{\text{model}}^{-1}(\bar{n}, V_{\text{eff}})] + \dots \quad (55)$$

As a test, we optimized the likelihood for the PATCHY NGC region using $\{\Lambda, \Lambda'\} = \{000, 000\}$. The 2D-grid was constructed using $\bar{n} \in [0.2, 4.4] \times 10^{-4} (h^{-1} \text{Mpc})^{-3}$ with an interval of $2 \times 10^{-5} (h^{-1} \text{Mpc})^{-3}$ and $V_{\text{eff}}^{-1} \in [0.2, 5] (h^{-1} \text{Gpc})^3$ in 40 volume bins. Fig. 12 shows a 2D interpolation of the log-likelihood. The degeneracy direction shows an inverse scaling relation between the number density and volume; this is as expected since lowering the number density increases the shot noise, which increases the overall amplitude of the covariance, but can be suppressed by a higher volume. For the PATCHY NGC region,¹³ the optimized number density and volume are respectively given by $\bar{n} = 2.4 \times 10^{-4} (h^{-1} \text{Mpc})^{-3}$ and $V_{\text{eff}}^{-1} = 1.57 (h^{-1} \text{Gpc})^3$.

The comparison of the correlation matrix for $\{\Lambda, \Lambda'\} = \{000, 000\}$ is shown in Fig. 13. The left and middle panels show the optimized correlation matrix from the model prediction and the covariance obtained from the PATCHY NGC mocks, respectively. The right panel shows a comparison for the diagonal elements of the analytic covariance model with and without optimization (solid red curve and dotted black curve, respectively), and the PATCHY mocks (dashed grey curve). Fig. 14 shows the half-inverse test in the left panel, with the right panel giving the covariance matrix eigenvalues predicted by the analytic model before optimization (dotted black curve), after optimization (solid red curve), and estimated from the PATCHY mocks (grey curve). Before applying the optimization, there is a clear mismatch between the theoretical prediction and the mock measurement, both in terms of its diagonal elements and the eigenvalues. The mean of the half-inverse matrix gives $\langle S \rangle = -9 \times 10^{-4}$, while the mean of the diagonal is -0.012 . The tests using the QUIJOTE mocks indicate no obvious deviations from RSD not nonlinearity, thus we expect the offset to arise due to the survey geometry. Fitting for the number density and effective volume, we find that one can moderately compensate for this effect.

To this end, we also perform a parameter fit including a total of 13 auto-covariance terms in which $\Lambda = \Lambda'$ (using those values of Λ which include at least one zero). We find the optimized number density and volume $\bar{n} = 2.0 \times 10^{-4} (h^{-1} \text{Mpc})^{-3}$ and $V_{\text{eff}}^{-1} = 1.57 (h^{-1} \text{Gpc})^3$. Fig. 15 shows a comparison of the correlation matrices estimated from the PATCHY NGC mocks and model prediction; for visibility we show 11 terms. Despite an overall good agreement between the mock correlation matrix and the model one, we find that different angular momentum orders are affected by the non-Gaussianity and survey geometry in different ways. As such, the number density and effective volume optimized for a specific angular momentum combination is not necessarily the optimal combination for the others. This indicates a fundamental limitation of the fitting approximation.

6 SUMMARY

Summary statistics, such as the N -point correlation functions, can effectively capture cosmological information from the spatial distribution of LSS. Throughout the past decades, significant work has been devoted to developing pipelines for the analysis of two-point statistics, focused primarily on the extraction of the BAO position and the growth parameter, $f\sigma_8$. The next generation of surveys, e.g. the Dark Energy Spectroscopic Instrument (DESI Collaboration et al. 2016), the Euclid satellite (Laureijs et al. 2011; Amendola et al. 2018), and the Rubin Observatory (LSST Science Collaboration et al. 2009) will map out much larger survey volumes with increased statistical power, facilitating analysis beyond the two-point function.

Higher-order statistics allow us to gain new insight into gravity-induced nonlinearities and neutrino masses, particularly in

¹³ We also performed the same fitting procedure for the SGC, obtaining $\bar{n} = 2.5 \times 10^{-4} (h^{-1} \text{Mpc})^{-3}$ and $V_{\text{eff}}^{-1} = 0.49 (h^{-1} \text{Gpc})^3$.

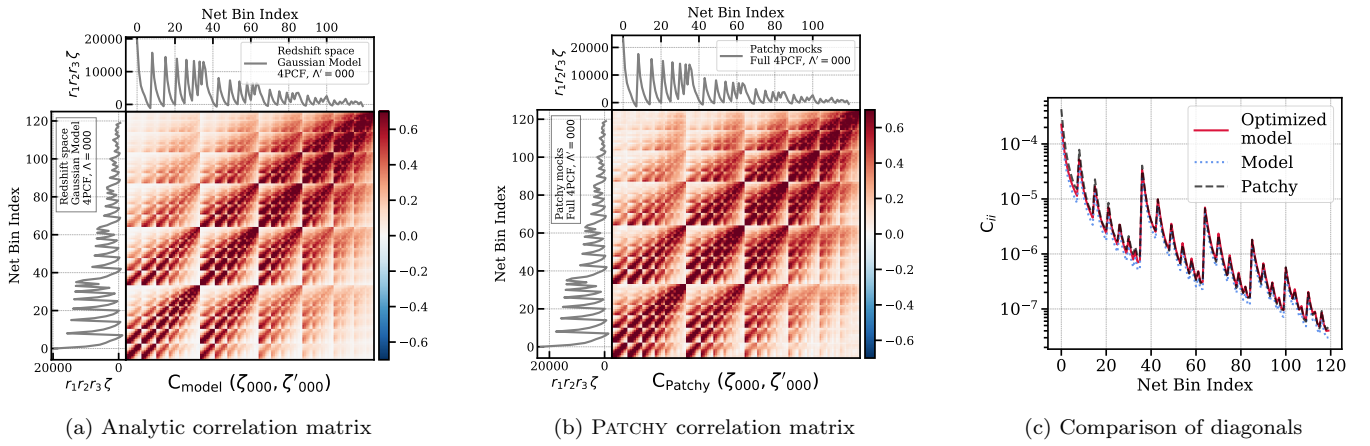


Figure 13. As Fig. 5 but for 999 PATCHY mocks. These include both RSD and survey geometry. The third panel shows a comparison of the diagonal elements for the PATCHY covariance (grey dashed curve), analytic covariance with and without optimization (red solid curve and black dotted curve, respectively).

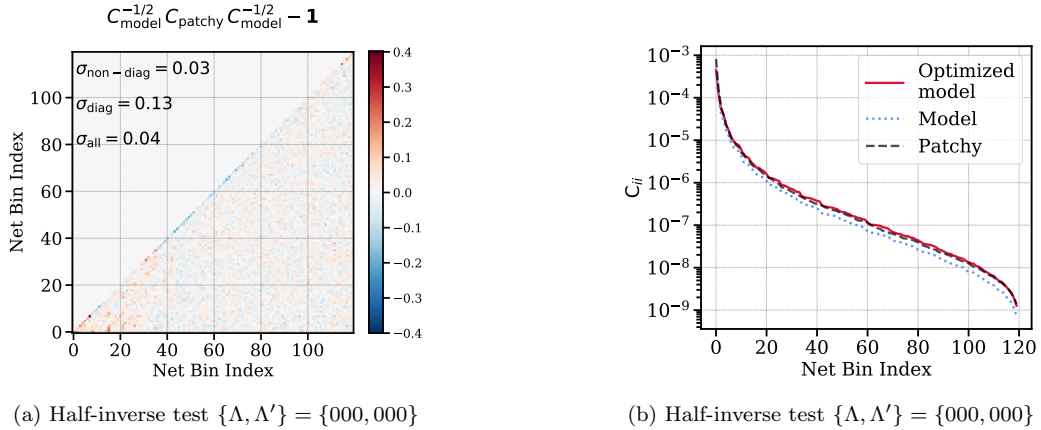


Figure 14. **Left panel:** half-inverse test for the model applied to the PATCHY NGC mocks for angular momenta $\{\Lambda, \Lambda'\} = \{000, 000\}$, as in Fig. 6a. **Right panel:** comparison of the eigenvalues for the theoretical covariance before optimization (dotted black curve), after optimization (solid red curve), and from the PATCHY mocks (dashed grey curve)

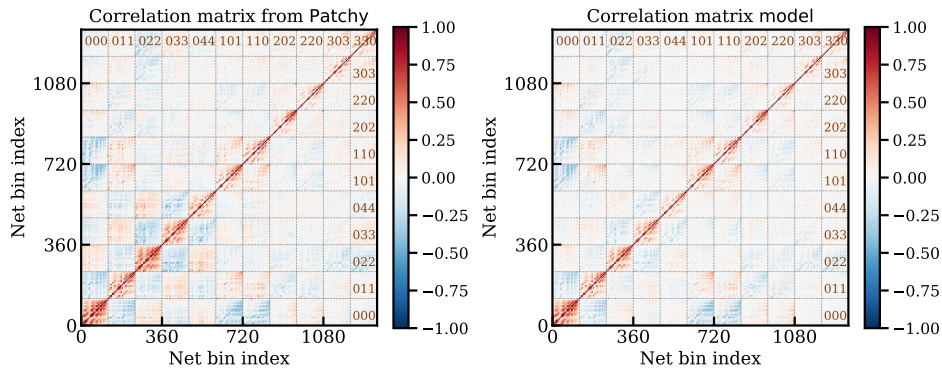


Figure 15. Comparison of correlation matrices estimated from PATCHY NGC mocks (**left**) and model (**right**). Unlike previous plots, we include 11 different choices of Λ , with each submatrix being the correlation between angular momentum sets $\{\Lambda, \Lambda'\} = \{\ell_1 \ell_2 \ell_3, \ell'_1 \ell'_2 \ell'_3\}$. The shot noise and volume entering the analytic covariance are optimized using 13 choices of Λ (those involving $\ell_i = 0$, up to $\ell_{\max} = 4$). Overall, we find reasonably good agreement between the Gaussian model and the sample covariance. We see some differences in the off-diagonal terms, and these differences increase with rising angular momenta. The diagonal terms are relatively consistent with each other, mostly as a result of the parameter fitting.

combination with two-point statistics. Further, they can be used to study scalar parity violation, which cannot be probed at all for NPCFs with $N \leq 3$. A particular challenge is that higher-order statistics usually imply high dimensionality; if one purses a simulation-based covariance estimation, a large number of mocks are required, which is computationally demanding.

In this paper we discuss an analytic approach to computing the NPCF covariance. In particular, we decompose the NPCF into the isotropic basis functions described in [Cahn & Slepian \(2020\)](#), and compute the covariance in this basis. Assuming the density field to be statistically isotropic (*i.e.* ignoring RSD), this is a natural basis to use, since it has full 3D rotational symmetry

When constructing higher-order NPCFs, it is important to subtract any contributions which also appear in the lower-order statistics, *i.e.* to use only the connected NPCF. As we have shown, the full NPCF covariance matrix can be written as a sum of two pieces, denoted as fully-coupled and partially-coupled, with only the former contributing to the covariances of connected NPCFs. We present a general formalism for the NPCF covariance under the assumption of Gaussianity, which we can further break down into basic elements as contractions between two overdensity fields. Each basic element consists of an f -integral (Eq. 29) with coefficients involving products of angular momenta and 3- j symbols multiplied by a phase. We show that the general NPCF covariance can be built directly out of these basic elements by invoking properties of the isotropic basis functions. In the $N = 4$ case, we explicitly derive the analytic form for the 4PCF covariance, introducing a diagrammatic representation to assist with understanding of the coupling structure. We also numerically implement the analytic formalism for this case.

We compare our theoretical model, which assumes Gaussianity, isotropy, and a uniform survey geometry, to simulations with various levels of realism, including the lognormal mocks, which have high redshift and high shot noise, but suppressed gravitational non-linearity, and the QUIJOTE simulations, which have low redshift and low shot noise, and include non-linear effects. One of the most interesting conclusions from these numerical tests is that, even though our naïve Gaussian model takes neither RSD nor gravitational non-Gaussianities into account, it produces a reasonably accurate estimate of the QUIJOTE covariances in real and redshift space. However, despite a good overall match for the lognormal mocks, we do observe spurious residuals via the half-inverse test. In particular, we find a residual in the diagonal elements, which is likely due to beyond-Gaussian correlators induced by shot noise effects. Finally, we also test our model using the PATCHY mocks. These have a realistic survey geometry, matching that of the BOSS DR12 CMASS sample. In this case, we found the survey geometry to have a major impact on our theoretical prediction. Since our analytic formalism does not include full treatment of the window function, we account for the geometry by fitting for the number density and the effective volume by maximizing a likelihood based on the KL-divergence. This is shown to roughly compensate for the window function. Our companion paper ([Philcox et al. 2021c](#)) shows that the theoretical covariance can be used as an important tool to facilitate data compression ([Soccimarro 2000; Taylor et al. 2013](#)), allowing a detection of gravitationally-induced non-Gaussianity from the BOSS 4PCF.

This work represents an important step along the path to constraining cosmology using higher-point functions. A number of extensions are possible, in particular, including modeling of window function effects, numerical implementation of the covariances including RSD, extension to higher-order statistics such as the 5PCF and 6PCF, and a more thorough study of the performance of the Gaussian model in the limit of high shot noise.

ACKNOWLEDGMENTS

We thank all members of the Slepian research group for useful discussions. JH thanks Hao Ding for insightful discussions. ZS thanks Simone Ferraro, Adam Ginsburg, Alex Krolewski, and Kristen Lavelle for useful discussions. OP acknowledges funding from the WFIRST program through NNG26PJ30C and NNN12AA01C, and thanks the University of Florida and the Simons Foundation for additional support.

The authors are pleased to acknowledge that the work reported on in this paper was substantially performed using the Princeton Research Computing resources at Princeton University which is consortium of groups led by the Princeton Institute for Computational Science and Engineering (PICSciE) and Office of Information Technology's Research Computing.

APPENDIX A: EXPLICIT RESULTS FOR THE GENERALIZED GAUNT INTEGRALS WITH $N = 2, 3$ AND 4

In §2.2 we discussed the generalized Gaunt integral; here, we present explicit results for $n = 2, 3$ and 4, following ([Cahn & Slepian 2020](#)). This uses the definition of Eq. (17), which includes the quantity $\mathcal{Q}^{\Lambda\Lambda'\Lambda''}$. For $n = 2$, given the definition of \mathcal{Q} in Eq. (15), we have $\Lambda \rightarrow (\ell, \ell)$, $\Lambda' \rightarrow (\ell', \ell')$, and $\Lambda'' \rightarrow (\ell'', \ell'')$. This leads to

$$\mathcal{G}^{\Lambda\Lambda'\Lambda''} = (4\pi)^{-1} \sqrt{(2\ell+1)(2\ell'+1)(2\ell''+1)} \begin{pmatrix} \ell & \ell' & \ell'' \\ 0 & 0 & 0 \end{pmatrix}^2. \quad (\text{A1})$$

This is a rescaling of the well-known result (Adams 1878) for the coefficient when a product of two Legendre polynomials is expanded into a sum over single Legendre polynomials.

For $n = 3$ the generalized Gaunt integral is given by

$$\begin{aligned} \mathcal{G}^{\Lambda\Lambda'\Lambda''} &= (4\pi)^{-3/2} \mathcal{Q}^{\Lambda\Lambda'\Lambda''} \prod_{i=1}^3 \begin{pmatrix} \ell_i & \ell'_i & \ell''_i \\ 0 & 0 & 0 \end{pmatrix} \sqrt{(2\ell_i + 1)(2\ell'_i + 1)(2\ell''_i + 1)} \\ &= (4\pi)^{-3/2} \begin{Bmatrix} \ell_1 & \ell'_1 & \ell''_1 \\ \ell_2 & \ell'_2 & \ell''_2 \\ \ell_3 & \ell'_3 & \ell''_3 \end{Bmatrix} \prod_{i=1}^3 \begin{pmatrix} \ell_i & \ell'_i & \ell''_i \\ 0 & 0 & 0 \end{pmatrix} \sqrt{(2\ell_i + 1)(2\ell'_i + 1)(2\ell''_i + 1)}, \end{aligned} \quad (\text{A2})$$

where we have used the definition of $\mathcal{C}_{000}^{\ell_i \ell'_i \ell''_i}$ (cf. Eq. 4) and $\mathcal{D}_{\ell_i \ell'_i \ell''_i}^{\text{P}}$ (cf. Eq. 12), and the quantity $\mathcal{Q}^{\Lambda\Lambda'\Lambda''}$ is given by a 9- j symbol, after summing over $m_i, m'_i,$ and m''_i (for $i = 1, 2, 3$).

For $n = 4$, expanding the $\mathcal{Q}^{\Lambda\Lambda'\Lambda''}$ quantity leads to 10 Wigner 3- j symbols, and consequently the product of two 9- j symbols. The detailed derivation of this is given in Cahn & Slepian (2020) (section 6.4 and equation 71), leading to the final result:

$$\begin{aligned} \mathcal{G}^{\Lambda\Lambda'\Lambda''} &= (4\pi)^{-2} \sqrt{(2\ell_{12} + 1)(2\ell'_{12} + 1)(2\ell''_{12} + 1)} \\ &\quad \times \prod_{i=1}^4 \sqrt{(2\ell_i + 1)(2\ell'_i + 1)(2\ell''_i + 1)} \begin{pmatrix} \ell_i & \ell'_i & \ell''_i \\ 0 & 0 & 0 \end{pmatrix} \\ &\quad \times \begin{Bmatrix} \ell_1 & \ell_2 & \ell_{12} \\ \ell'_1 & \ell'_2 & \ell'_{12} \\ \ell''_1 & \ell''_2 & \ell''_{12} \end{Bmatrix} \begin{Bmatrix} \ell_{12} & \ell_3 & \ell_4 \\ \ell'_{12} & \ell'_3 & \ell'_4 \\ \ell''_{12} & \ell''_3 & \ell''_4 \end{Bmatrix}. \end{aligned} \quad (\text{A3})$$

APPENDIX B: DERIVATION OF THE BASIC COVARIANCE ELEMENTS

B1 Real Space

Here we derive the basic covariance elements presented in §4.1. Without loss of generality we consider only the contraction between a single pair of endpoints, neglecting the subindices and denoting the positions as \mathbf{r} and \mathbf{r}' . The coupling between two endpoints across the unprimed and primed families can be expanded as:

$$\begin{aligned} \langle \delta(\mathbf{x} + \mathbf{r}) \delta(\mathbf{x} + \mathbf{s} + \mathbf{r}') \rangle &= \xi(|\mathbf{r}' + \mathbf{s} - \mathbf{r}|) = \int_{\mathbf{k}} e^{i\mathbf{k} \cdot (\mathbf{r}' + \mathbf{s} - \mathbf{r})} P(k) \\ &= (4\pi)^3 \sum_{\ell m} \sum_{\ell' m'} \sum_{LM} i^{\ell' + L - \ell} \int_{\mathbf{k}} P(k) \\ &\quad \times j_{\ell'}(kr') j_L(ks) j_{\ell}(kr) Y_{\ell' m'}^*(\hat{\mathbf{k}}) Y_{\ell' m'}(\hat{\mathbf{r}}') Y_{LM}(\hat{\mathbf{k}}) Y_{LM}^*(\hat{\mathbf{s}}) Y_{\ell m}^*(\hat{\mathbf{k}}) Y_{\ell m}(\hat{\mathbf{r}}), \end{aligned} \quad (\text{B1})$$

where, as stated in §3, we have assumed isotropy (*i.e.* that $P(\mathbf{k}) = P(k)$) in the first equality. The second equality arises from applying the plane wave expansion three times. Performing the angular integral over $\hat{\mathbf{k}}$ gives the Gaunt integral:

$$\begin{aligned} \mathcal{G}_{\ell\ell'L}^{mm'M} &\equiv \int d\Omega_{\mathbf{k}} Y_{\ell m}^*(\hat{\mathbf{k}}) Y_{\ell' m'}(\hat{\mathbf{k}}) Y_{LM}^*(\hat{\mathbf{k}}) = \sqrt{\frac{(2\ell + 1)(2\ell' + 1)(2L + 1)}{4\pi}} \begin{pmatrix} \ell & \ell' & L \\ 0 & 0 & 0 \end{pmatrix} \begin{pmatrix} \ell & \ell' & L \\ m & m' & M \end{pmatrix} \\ &= (4\pi)^{-1/2} \mathcal{D}_{\ell\ell'L}^{\text{P}} \mathcal{C}_{000}^{\ell\ell'L} \mathcal{C}_{mm'M}^{\ell\ell'L}. \end{aligned} \quad (\text{B2})$$

Inserting the definition of the f -integral, Eq. (B1) becomes

$$\begin{aligned} \langle \delta(\mathbf{x} + \mathbf{r}) \delta(\mathbf{x} + \mathbf{s} + \mathbf{r}') \rangle &= (4\pi)^3 \sum_{\ell\ell'L} \sum_{mm'M} i^{-\ell + \ell' + L} (4\pi)^{-1} f_{\ell\ell'L}(r, r', s) (4\pi)^{-1/2} \mathcal{D}_{\ell\ell'L}^{\text{P}} \mathcal{C}_{000}^{\ell\ell'L} \mathcal{C}_{mm'M}^{\ell\ell'L} \\ &\quad \times Y_{\ell m}(\hat{\mathbf{r}}) Y_{\ell' m'}(\hat{\mathbf{r}}') Y_{LM}(\hat{\mathbf{s}}) \\ &= (4\pi)^{3/2} \sum_{\ell\ell'L} i^{-\ell + \ell' + L} f_{\ell\ell'L}(r, r', s) \mathcal{D}_{\ell\ell'L}^{\text{P}} \mathcal{C}_{000}^{\ell\ell'L} \mathcal{P}_{\ell\ell'L}(\hat{\mathbf{r}}, \hat{\mathbf{r}}', \hat{\mathbf{s}}). \end{aligned} \quad (\text{B3})$$

Finally, we give expressions for the contraction of two overdensity fields from the same family. These self-coupling terms do not occur in the calculation of the covariance of the connected NPCF, but do appear if one considers a covariance which includes the disconnected piece (as in Appendix C). In this case, \mathbf{r}_i and \mathbf{r}_j denote two endpoints from the same family. As before, we apply the plane wave expansion to the exponentials in Eq. (26), then integrate over $\hat{\mathbf{k}}$ to find:

$$\begin{aligned} \langle \delta(\mathbf{x} + \mathbf{r}_i) \delta(\mathbf{x} + \mathbf{r}_j) \rangle &= \xi(|\mathbf{r}_i - \mathbf{r}_j|) = \int \frac{k^2 dk}{2\pi^2} P(k) \sum_{\ell} j_{\ell}(kr_i) j_{\ell}(kr_j) (2\ell + 1) \mathcal{L}_{\ell}(\hat{\mathbf{r}}_i \cdot \hat{\mathbf{r}}_j) \\ &= (4\pi)^{3/2} \sum_{\ell} (-1)^{\ell} \sqrt{2\ell + 1} f_{\ell\ell 0}(r_i, r_j, 0) \mathcal{P}_{\ell\ell 0}(\hat{\mathbf{r}}_i, \hat{\mathbf{r}}_j, 0). \end{aligned} \quad (\text{B4})$$

In the second line, we have written our result in terms of the $N = 3$ isotropic functions to maintain a consistent structure for all the basic elements. If one of the two overdensity fields is a primary, the expectation value is simply a 2PCF:

$$\langle \delta(\mathbf{x} + \mathbf{r}_0)\delta(\mathbf{x} + \mathbf{r}_i) \rangle |_{\mathbf{r}_0 \rightarrow 0} = \xi(|\mathbf{r}_i - \mathbf{r}_0|) |_{\mathbf{r}_0 \rightarrow 0} = (4\pi)^{3/2} f_{000}(r, 0, 0) \mathcal{P}_{000}(\hat{\mathbf{r}}, 0, 0). \quad (\text{B5})$$

B2 Redshift Space

Below, we derive the basic elements in redshift space, as a preparation for the fully-coupled covariance with RSD discussed in Appendix E. We first expand the power spectrum in terms of Legendre polynomials:

$$P(\mathbf{k}) = \sum_{\lambda} P_{\lambda}(k) L_{\lambda}(\hat{\mathbf{k}} \cdot \hat{\mathbf{n}}) = \sum_{\lambda \mu} \frac{4\pi}{2\lambda + 1} P_{\lambda}(k) Y_{\lambda \mu}^*(\hat{\mathbf{k}}) Y_{\lambda \mu}(\hat{\mathbf{n}}) \quad (\text{B6})$$

where $P_{\lambda}(k)$ is the λ -th Legendre multipole of the power spectrum (where λ is even) and $\hat{\mathbf{n}}$ is the line of sight.

The expectation value of the product of two overdensity fields now reads

$$\begin{aligned} \langle \delta(\mathbf{x} + \mathbf{r})\delta(\mathbf{x} + \mathbf{r}' + \mathbf{s}) \rangle &= \int_{\mathbf{k}} e^{i\mathbf{k} \cdot (\mathbf{r}' + \mathbf{s} - \mathbf{r})} P(\mathbf{k}) \\ &= \int_{\mathbf{k}} e^{i\mathbf{k} \cdot (\mathbf{r}' + \mathbf{s} - \mathbf{r})} \sum_{\lambda \mu} \frac{4\pi}{2\lambda + 1} P_{\lambda}(k) Y_{\lambda \mu}^*(\hat{\mathbf{k}}) Y_{\lambda \mu}(\hat{\mathbf{n}}) \\ &= \int \frac{d\hat{\mathbf{k}}}{4\pi} \int \frac{k^2 dk}{2\pi^2} (4\pi)^3 \sum_{\ell \ell' L} \sum_{m m' M} i^{\ell' + L - \ell} j_{\ell'}(kr') j_{\ell''}(ks) j_{\ell}(kr) Y_{\ell' m'}^*(\hat{\mathbf{k}}) Y_{LM}(\hat{\mathbf{k}}) Y_{\ell m}^*(\hat{\mathbf{k}}) \\ &\quad \times Y_{\ell' m'}(\hat{\mathbf{r}}') Y_{LM}(\hat{\mathbf{s}}) Y_{\ell m}(\hat{\mathbf{r}}) \sum_{\lambda \mu} \frac{4\pi}{2\lambda + 1} P_{\lambda}(k) Y_{\lambda \mu}^*(\hat{\mathbf{k}}) Y_{\lambda \mu}(\hat{\mathbf{n}}). \end{aligned} \quad (\text{B7})$$

We can perform an angular integral over $\hat{\mathbf{k}}$:

$$\begin{aligned} \int d\hat{\mathbf{k}} Y_{\ell m}^*(\hat{\mathbf{k}}) Y_{\ell' m'}^*(\hat{\mathbf{k}}) Y_{LM}^*(\hat{\mathbf{k}}) Y_{\lambda \mu}^*(\hat{\mathbf{k}}) &= \sum_{\bar{L}} (-1)^{\bar{M}} \mathcal{G}_{mm' \bar{M}}^{\ell \ell' \bar{L}} \mathcal{G}_{-M M \mu}^{\bar{L} L \lambda} \\ &= (4\pi)^{-1} \sum_{\bar{L}} (-1)^{\bar{M}} \mathcal{D}_{\ell \ell' L \lambda}^{\bar{P}} (2\bar{L} + 1) \mathcal{C}_{mm' \bar{M}}^{\ell \ell' \bar{L}} \mathcal{C}_{-M M \mu}^{\bar{L} L \lambda} \mathcal{C}_{000}^{\ell \ell' \bar{L}} \mathcal{C}_{000}^{\bar{L} L \lambda} \\ &= (4\pi)^{-1} \mathcal{D}_{\ell \ell' L \lambda}^{\bar{P}} \mathcal{C}_{mm' m'' \mu}^{\ell \ell' L \lambda} \mathcal{C}_{0000}^{\ell \ell' L \lambda}; \end{aligned} \quad (\text{B8})$$

because of the additional l.o.s. direction $\hat{\mathbf{n}}$, we need to consider isotropic functions with four arguments:

$$\mathcal{P}_{\ell \ell' L \lambda}(\hat{\mathbf{r}}, \hat{\mathbf{r}}', \hat{\mathbf{s}}, \hat{\mathbf{n}}) = \sum_{mm' M \mu} \mathcal{C}_{mm' M \mu}^{\ell \ell' L \lambda} Y_{\ell m}(\hat{\mathbf{r}}) Y_{\ell' m'}(\hat{\mathbf{r}}') Y_{LM}(\hat{\mathbf{s}}) Y_{\lambda \mu}(\hat{\mathbf{n}}). \quad (\text{B9})$$

To incorporate the power spectrum multipole decomposition, we extend the definition of the f -integral as follows:

$$f_{\ell_1 \ell_2 \ell_3}^{\lambda}(r_1, r_2, r_3) = \int \frac{k^2 dk}{2\pi^2} P_{\lambda}(k) j_{\ell_1}(kr_1) j_{\ell_2}(kr_2) j_{\ell_3}(kr_3). \quad (\text{B10})$$

The redshift space basic covariance element can thus be written:

$$\langle \delta(\mathbf{x} + \mathbf{r})\delta(\mathbf{x} + \mathbf{r}' + \mathbf{s}) \rangle = (4\pi)^2 \sum_{\ell \ell' L \lambda} i^{-\ell + \ell' + L} \frac{1}{2\lambda + 1} \mathcal{D}_{\ell \ell' L \lambda}^{\bar{P}} \mathcal{C}_{0000}^{\ell \ell' L \lambda} f_{\ell \ell' L}^{\lambda}(r, r', s) \mathcal{P}_{\ell \ell' L \lambda}(\hat{\mathbf{r}}, \hat{\mathbf{r}}', \hat{\mathbf{s}}, \hat{\mathbf{n}}). \quad (\text{B11})$$

APPENDIX C: PARTIALLY-COUPLED 4PCF COVARIANCE

C1 Fully-Coupled and Partially-Coupled Covariances

In §4.2 we presented the fully-coupled covariance, which is the part of relevance for the connected NPCF estimator. As before, the connected estimator is obtained by subtracting the disconnected piece from full estimator as in Eq. (21). This feature is now included in the ENCORE code, and is discussed at length in our companion paper Philcox et al. (2021b). For completeness however, we will discuss in this section how one may estimate the partially-coupled covariance.

We first sketch our reasoning for ignoring the partially-coupled terms in the connected 4PCF covariance. Following the definition of our estimator, the fully-coupled covariance can be written as

$$\begin{aligned} \text{Cov}^{\text{fc}}(\mathbf{R}, \mathbf{R}') &\equiv \text{Cov}(\hat{\zeta}_{\text{c}}, \hat{\zeta}_{\text{c}}) \\ &= \text{Cov}(\hat{\zeta}, \hat{\zeta}) - \text{Cov}(\hat{\zeta}_{\text{dc}}, \hat{\zeta}) - \text{Cov}(\hat{\zeta}, \hat{\zeta}_{\text{dc}}) + \text{Cov}(\hat{\zeta}_{\text{dc}}, \hat{\zeta}_{\text{dc}}), \end{aligned} \quad (\text{C1})$$

where the the first term in the second equality, the covariance of the full estimator, is simply the covariance obtained from all combinations of eight overdensity fields. We use $\langle \delta\delta\delta\delta \rangle$ to denote the full estimator; given the symmetry, any one of the overdensity fields can be thought of as a primary vertex, with the position of its neighbours fixed relative to the primary. As

before, the covariance of the full estimator consists of both fully- and partially-coupled parts. Below, we give an example of a contraction that leads to a partially-coupled term (here with angle brackets representing spatial integrals rather than statistical expectations):

$$\text{Cov}(\hat{\zeta}, \hat{\zeta}) \rightarrow \langle \overline{\delta \delta} \overline{\delta \delta} \rangle \langle \overline{\delta' \delta' \delta' \delta'} \rangle.$$

The disconnected estimator is represented by $\langle \delta \delta \rangle \langle \delta \delta \rangle$. Again, we know the relative position between overdensity fields appears within a $\langle \dots \rangle$ integral, but the relative position between two $\langle \dots \rangle$ is free. This leads us to consider only the self-coupling contractions within an integral such as $\langle \overline{\delta \delta} \rangle \langle \delta \delta \rangle$; this contraction is, by definition, a 2PCF. Contractions such as $\langle \delta \delta \rangle \langle \delta \delta \rangle$ must be integrated over the unfixed pair separation vector, resulting in an additional volume factor V^{-1} , which leads to a strong suppression. Below, we list the contractions that contribute to the partially-coupled covariance at leading order:

$$\begin{aligned} \text{Cov}(\hat{\zeta}_{\text{dc}}, \hat{\zeta}) &\rightarrow \langle \overline{\delta \delta} \rangle \langle \delta \delta \rangle \langle \overline{\delta' \delta' \delta' \delta'} \rangle \\ \text{Cov}(\hat{\zeta}, \hat{\zeta}_{\text{dc}}) &\rightarrow \langle \overline{\delta \delta} \rangle \langle \delta \delta \rangle \langle \overline{\delta' \delta' \delta' \delta'} \rangle \\ \text{Cov}(\hat{\zeta}_{\text{dc}}, \hat{\zeta}_{\text{dc}}) &\rightarrow \langle \overline{\delta \delta} \rangle \langle \delta \delta \rangle \langle \overline{\delta' \delta' \delta' \delta'} \rangle. \end{aligned}$$

After counting the permutations, we find 72 terms, in each case, all of which cancel. This leads only corrections of $\mathcal{O}((r_c^3/V)^2)$ and higher, where $r_c \sim 100 h^{-1} \text{Mpc}$ is the correlation length. This correction is typically $\sim 0.1\%$ and hence can be neglected when comparing to the measurements from the mock simulations with box length of $L_{\text{box}} \sim \mathcal{O}(1) h^{-1} \text{Gpc}$. We thus conclude that the fully coupled covariance does represent that of the connected 4PCF in the large-volume limit.

C2 Analytic Form

For completeness, we also derive analytic expressions for the partially-coupled covariance. These contributions are composed of similar structures to the basic elements shown in §4.1 and can be divided into four pieces as shown in Fig. C1. All terms involve a self-coupling, *i.e.* the contraction of overdensity fields within a primed or unprimed family. As a result, the basis function will end up with one of the angular momenta being zero, with the other two equal. This implies that the partially-coupled covariance can be fully characterized just by ℓ and ℓ' . The fundamental idea of the derivation is similar to that underlying the fully-coupled covariance derivation. First, identify the basic elements that contribute to the given cases. Second, apply a rotational average over the three direction vectors $\hat{\mathbf{r}}$, $\hat{\mathbf{r}}'$, and $\hat{\mathbf{s}}$ and reorder the permuted coordinates into canonical ordering. Third, project the covariance onto the isotropic basis, picking out the terms proportional to $\mathcal{P}_\Lambda(\hat{\mathbf{R}})$ and $\mathcal{P}_{\Lambda'}(\hat{\mathbf{R}}')$. Here we necessarily need to introduce both permutations G and H because self-contraction breaks the symmetry of the coupling structure. As before, we restrict G to cyclic permutations, allowing H to explore all possibilities.

Case I The partially-coupled covariance in this case contains the self-contraction between primary vertices, \mathbf{r}_0 and \mathbf{r}'_0 , and endpoints of their own family (see Fig. C1). This can be expressed as

$$\begin{aligned} I_1(\mathbf{R}, \mathbf{R}'; \mathbf{s}) &= \langle \delta(\mathbf{x} + \mathbf{r}_0) \delta(\mathbf{x} + \mathbf{r}_{G1}) \rangle \langle \delta(\mathbf{x} + \mathbf{s} + \mathbf{r}'_0) \delta(\mathbf{x} + \mathbf{s} + \mathbf{r}'_{H1}) \rangle |_{\mathbf{r}_0=0, \mathbf{r}'_0=0} \\ &\times \langle \delta(\mathbf{x} + \mathbf{r}_{G2}) \delta(\mathbf{x} + \mathbf{s} + \mathbf{r}'_{H2}) \rangle \langle \delta(\mathbf{x} + \mathbf{r}_{G3}) \delta(\mathbf{x} + \mathbf{s} + \mathbf{r}'_{H3}) \rangle. \end{aligned} \quad (\text{C2})$$

Inserting the definition of the basic elements defined in §4.1, we find

$$\begin{aligned} I_1(\mathbf{R}, \mathbf{R}'; \mathbf{s}) &= \sum_{G,H} (4\pi)^{3/2} f_{000}(r_{G1}, 0, 0) \mathcal{P}_{000}(\hat{\mathbf{r}}_{G1}, 0, 0) (4\pi)^{3/2} f_{000}(0, r'_{H1}, 0) \mathcal{P}_{000}(0, \hat{\mathbf{r}}'_{H1}, 0) \\ &\times (4\pi)^{3/2} \sum_{\ell_{G2} \ell'_{H2} L_2} i^{-\ell_{G2} + \ell'_{H2} + L_2} f_{\ell_{G2} \ell'_{H2} L_2}(r_{G2}, r'_{H2}, \mathbf{s}) \mathcal{D}_{\ell_{G2} \ell'_{H2} L_2}^{\text{P}} \mathcal{C}_0^{\ell_{G2} \ell'_{H2} L_2} \mathcal{P}_{\ell_{G2} \ell'_{H2} L_2}(\hat{\mathbf{r}}_{G2}, \hat{\mathbf{r}}'_{H2}, \hat{\mathbf{s}}) \\ &\times (4\pi)^{3/2} \sum_{\ell_{G3} \ell'_{H3} L_3} i^{-\ell_{G3} + \ell'_{H3} + L_3} f_{\ell_{G3} \ell'_{H3} L_3}(r_{G3}, r'_{H3}, \mathbf{s}) \mathcal{D}_{\ell_{G3} \ell'_{H3} L_3}^{\text{P}} \mathcal{C}_{000}^{\ell_{G3} \ell'_{H3} L_3} \mathcal{P}_{\ell_{G3} \ell'_{H3} L_3}(\hat{\mathbf{r}}_{G3}, \hat{\mathbf{r}}'_{H3}, \hat{\mathbf{s}}). \end{aligned} \quad (\text{C3})$$

Given that the sum of the orbital angular momentum must be an even number, $\ell_{G2} = \ell'_{H2}$ and $\ell_{G3} = \ell'_{H3}$, thus the sum reduces to one over ℓ, ℓ', ℓ'' with $\mathcal{L} = (\ell, \ell)$, $\mathcal{L}' = (\ell', \ell')$, $\mathcal{L}'' = (L, L)$. As a reminder, the coefficients \mathcal{C} and \mathcal{D}^{P} are given in Eq. (4) and Eq. (12), respectively. Integrating over \mathbf{s} we find

$$\begin{aligned} \int \frac{d^3 \mathbf{s}}{V} I_1(\mathbf{R}, \mathbf{R}'; \mathbf{s}) &= \sum_{G,H} \sum_{\mathcal{L}_G, \mathcal{L}'_H} \int \frac{s^2 ds}{V} \xi(r_{G1}) \xi(r'_{H1}) (4\pi)^4 \sum_{\ell \ell' L} (-1)^{\ell + \ell' + L} f_{\ell \ell' L}(r_{G2}, r'_{H2}, s) f_{\ell \ell' L}(r_{G3}, r'_{H3}, s) \\ &\times (\mathcal{D}_{\ell \ell' L}^{\text{P}})^2 (\mathcal{C}_{000}^{\ell \ell' L})^2 \mathcal{Q}^{(\ell \ell')(\ell \ell')(\mathcal{L} \mathcal{L})} \mathcal{D}_{\mathcal{L} \mathcal{L}}^{\text{P}} \mathcal{C}_{00}^{\mathcal{L} \mathcal{L}} \mathcal{P}_{\mathcal{L}_G}(\hat{\mathbf{r}}_{G1}, \hat{\mathbf{r}}_{G2}, \hat{\mathbf{r}}_{G3}) \mathcal{P}_{\mathcal{L}'_H}(\hat{\mathbf{r}}'_{H1}, \hat{\mathbf{r}}'_{H2}, \hat{\mathbf{r}}'_{H3}), \end{aligned} \quad (\text{C4})$$

where the rotational average over $d\mathcal{S}$ gives a factor of 4π , following our normalization convention. \mathcal{L}_G has one angular momentum of zero with the other two equal; the same goes for \mathcal{L}'_H . Expressing the two-argument isotropic basis functions in terms of those

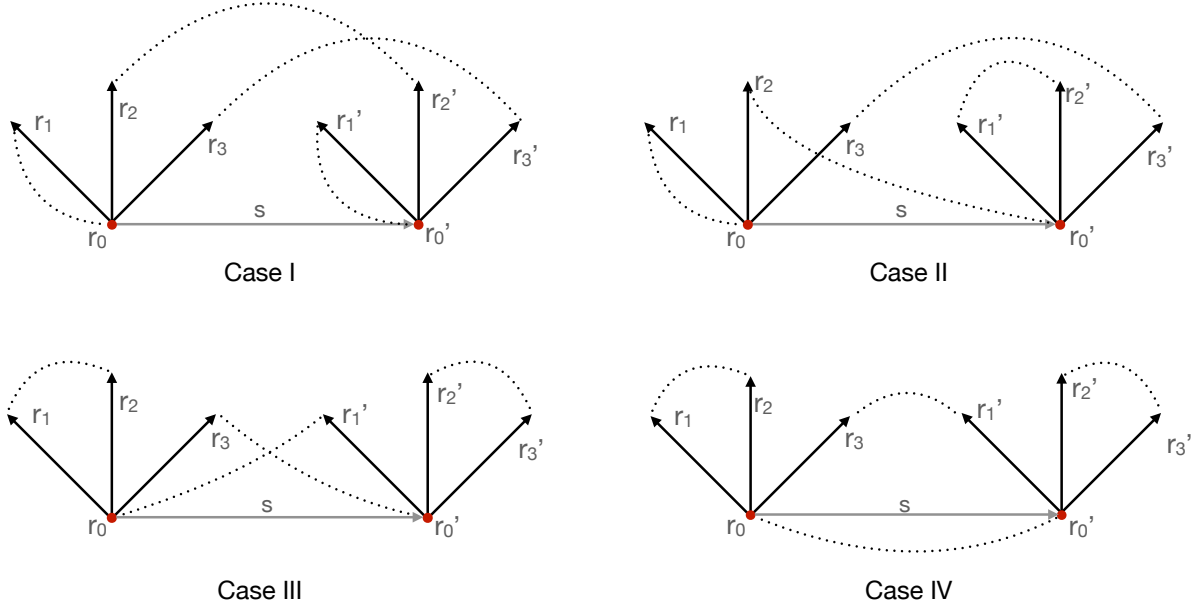


Figure C1. Diagrams for the partially-coupled covariance. This Figure is analogous to Fig. 2, but gives the terms necessary to model the *disconnected* 4PCF covariance.

with three arguments, for example, $\mathcal{P}_{\ell\ell}(\hat{\mathbf{r}}_{G2}, \hat{\mathbf{r}}_{G3}) = (4\pi)^{1/2} \mathcal{P}_{0\ell\ell}(\hat{\mathbf{r}}_{G1}, \hat{\mathbf{r}}_{G2}, \hat{\mathbf{r}}_{G3})$, we obtain an additional 4π . We now insert the definition of the generalized Gaunt integral for $N = 2$ (cf. Eq. A1), giving

$$\int \frac{d^3\mathbf{s}}{V} I_1(\mathbf{R}, \mathbf{R}'; \mathbf{s}) = \sum_{G,H} \sum_{\mathcal{L}_G, \mathcal{L}'_H} \int \frac{s^2 ds}{V} \xi(r_{G1}) \xi(r'_{H1}) (4\pi)^4 \sum_{\ell\ell'L} (-1)^{\ell+\ell'} f_{\ell\ell'L}(r_{G2}, r'_{H2}, s) f_{\ell\ell'L}(r_{G3}, r'_{H3}, s) \\ \times \sqrt{(2\ell+1)(2\ell'+1)(2L+1)} \begin{pmatrix} \ell & \ell' & L \\ 0 & 0 & 0 \end{pmatrix}^2 \mathcal{P}_{\mathcal{L}_G}(\hat{\mathbf{r}}_{G1}, \hat{\mathbf{r}}_{G2}, \hat{\mathbf{r}}_{G3}) \mathcal{P}_{\mathcal{L}'_H}(\hat{\mathbf{r}}'_{H1}, \hat{\mathbf{r}}'_{H2}, \hat{\mathbf{r}}'_{H3}). \quad (\text{C5})$$

Using Eq. (19), we may restore the arguments to canonical order:

$$\mathcal{P}_{\mathcal{L}_G}(\hat{\mathbf{R}}_G) = \sum_J \mathcal{B}_{\mathcal{L}_G, J}^{G-1} \mathcal{P}_J(\hat{\mathbf{R}}), \quad \mathcal{P}_{\mathcal{L}'_H}(\hat{\mathbf{R}}'_H) = \sum_{J'} \mathcal{B}_{\mathcal{L}'_H, J'}^{H-1} \mathcal{P}_{J'}(\hat{\mathbf{R}}'). \quad (\text{C6})$$

In this case, $\mathcal{B}_{\mathcal{L}_G, J}^{G-1}$ and $\mathcal{B}_{\mathcal{L}'_H, J'}^{H-1}$ are given by products of Kronecker deltas since one of the angular momenta is zero. Since the partially-coupled covariance always leads to products of two f -integrals, it is useful to introduce the g -integral, defined by:

$$\int s^2 ds f_{\ell\ell\lambda}(r_1, r_2, s) f_{\ell'\ell'\lambda}(r'_1, r'_2, s) \\ = \int \frac{k^2 dk}{(2\pi)^3} j_\ell(kr_1) j_\ell(kr_2) j_{\ell'}(kr'_1) j_{\ell'}(kr'_2) P^2(k) \equiv g_{\ell\ell\ell'\ell'}(r_1, r_2, r'_1, r'_2). \quad (\text{C7})$$

It is worth noting that, unlike the f -integral, the g -integral has dimensions of volume. The coefficient $(2\pi)^{-3}$ appears due to the definition of the f -integral, together with the coefficient in the identity for the integral of two sBFs:

$$\int s^2 ds j_\lambda(sa) j_\lambda(sb) = \frac{\pi}{2ab} \delta_D(a-b). \quad (\text{C8})$$

Together with the relation:

$$\sum_L (2L+1) \begin{pmatrix} \ell & \ell' & L \\ 0 & 0 & 0 \end{pmatrix}^2 = 1, \quad (\text{C9})$$

we find the final expression for the partially-coupled covariance Case I:

$$\text{Cov}_{\Lambda, \Lambda'}^{(\text{pc}), \text{I}} = \sum_{G,H} \sum_{\mathcal{L}_G, \mathcal{L}'_H} \frac{(4\pi)^4}{V} (-1)^{\ell+\ell'} \sqrt{(2\ell+1)(2\ell'+1)} \xi(r_{G1}) \xi(r'_{H1}) g_{\ell\ell\ell'\ell'}(r_{G2}, r_{G3}, r'_{H2}, r'_{H3}) \mathcal{B}_{\mathcal{L}_G, \Lambda}^{G-1} \mathcal{B}_{\mathcal{L}'_H, \Lambda'}^{H-1}. \quad (\text{C10})$$

Here we keep the inverse reordering coefficient to make clear that the partially-coupled covariance only contributes to the collection of the three angular momenta with the following form $\{\Lambda, \Lambda'\} = \{0\ell\ell, 0\ell'\ell'\} + 8 \text{ perms.}$

Case II In this case, only one of the primary vertices is connected intra-family-wise (as shown in Fig. C1). It can happen that the primary vertex of the primed tetrahedron is coupled to an unprimed vertex, or the other way around. By symmetry, we need only discuss one of the two possibilities. The contraction of the eight overdensity fields can be expressed as

$$I_{\text{II}}(\mathbf{R}, \mathbf{R}'; \mathbf{s}) = \langle \delta(\mathbf{x} + \mathbf{r}_0) \delta(\mathbf{x} + \mathbf{r}_{G1}) \rangle \langle \delta(\mathbf{x} + \mathbf{r}_{G2}) \delta(\mathbf{x} + \mathbf{s} + \mathbf{r}'_0) \rangle |_{r_0=r'_0=0} \\ \times \langle \delta(\mathbf{x} + \mathbf{s} + \mathbf{r}'_{H1}) \delta(\mathbf{x} + \mathbf{s} + \mathbf{r}'_{H2}) \rangle \langle \delta(\mathbf{x} + \mathbf{r}_{G3}) \delta(\mathbf{x} + \mathbf{s} + \mathbf{r}'_{H3}) \rangle. \quad (\text{C11})$$

In terms of the basic elements, $I_{\text{II}}(\mathbf{R}, \mathbf{R}'; \mathbf{s})$ becomes

$$I_{\text{II}}(\mathbf{R}, \mathbf{R}'; \mathbf{s}) \\ = \sum_{G,H} (4\pi)^{3/2} f_{000}(r_{G1}, 0, 0) \mathcal{P}_{000}(\hat{\mathbf{r}}_{G1}, 0, 0) \\ \times (4\pi)^{3/2} \sum_{\ell'_{H1}} (-1)^{\ell'_{H1}} f_{\ell'_{H1} \ell'_{H1} 0}(r'_{H1}, r'_{H2}, 0) \sqrt{2\ell'_{H1} + 1} \mathcal{P}_{\ell'_{H1} \ell'_{H1} 0}(\hat{\mathbf{r}}'_{H1}, \hat{\mathbf{r}}'_{H2}, 0) \\ \times (4\pi)^{3/2} \sum_{\ell_{G2}} (-1)^{\ell_{G2}} f_{\ell_{G2} 0 \ell_{G2}}(r_{G2}, 0, s) \sqrt{2\ell_{G2} + 1} \mathcal{P}_{\ell_{G2} 0 \ell_{G2}}(\hat{\mathbf{r}}_{G2}, 0, \hat{\mathbf{s}}) \\ \times (4\pi)^{3/2} \sum_{\ell_{G3} \ell'_{H3} L_3} i^{-\ell_{G3} + \ell'_{H3} + L_3} f_{\ell_{G3} \ell'_{H3} L_3}(r_{G3}, r'_{H3}, s) \mathcal{D}_{\ell_{G3} \ell'_{H3} L_3}^{\text{P}} \mathcal{C}_{000}^{\ell_{G3} \ell'_{H3} L_3} \mathcal{P}_{\ell_{G3} \ell'_{H3} L_3}(\hat{\mathbf{r}}_{G3}, \hat{\mathbf{r}}'_{H3}, \hat{\mathbf{s}}). \quad (\text{C12})$$

Averaging over $d\mathcal{S}$ involves only two angular momenta, ℓ_{G2} and L_3 , enforcing $\ell_{G2} = L_3 \equiv \ell$. Similarly, averaging over $d\mathcal{R}$ involves just ℓ_{G2} and ℓ_{G3} and sets $\ell_{G2} = \ell_{G3} \equiv \ell$. Finally, since $\hat{\mathbf{r}}'_{H1}$ and $\hat{\mathbf{r}}'_{H2}$ are already combined into an isotropic function, the integration over $d\mathcal{R}'$ effectively involves only $\hat{\mathbf{r}}'_{H3}$ and will result in $\ell'_{H3} = 0$. The imaginary phase also becomes unity.

Using the definition given in Eq. (C7), we have

$$\int s^2 ds f_{\ell 0 \ell}(r_{G2}, 0, s) f_{\ell 0 \ell}(r_{G3}, r'_{H3}, s) = g_{\ell 0 \ell}(r_{G2}, 0, r_{G3}, r'_{H3}); \quad (\text{C13})$$

in this case, the g -integral can be reduced to an f -integral. The final form of Case II reads:

$$\text{Cov}_{\Lambda, \Lambda'}^{(\text{pc}), \text{II}} = \sum_{G,H} \sum_{\mathcal{L}_G, \mathcal{L}'_H} \frac{(4\pi)^4}{V} (-1)^{\ell + \ell'} \xi(r_{G1}) \sqrt{(2\ell + 1)(2\ell' + 1)} f_{\ell' \ell' 0}(r'_{H1}, r'_{H2}, 0) g_{\ell 0 \ell}(r_{G2}, 0, r_{G3}, r'_{H3}) \mathcal{B}_{\mathcal{L}_G, \Lambda}^{G-1} \mathcal{B}_{\mathcal{L}'_H, \Lambda'}^{H-1}. \quad (\text{C14})$$

The case in which an unprimed primary vertex $\delta(\mathbf{r}_0)$ couples to an endpoint from the primed family $\delta(\mathbf{r}'_i)$ follows similarly.

Case III The next form to consider occurs when both the primed vertices are coupled to a vertex from the opposite family. In this case:

$$I_{\text{III}}(\mathbf{R}, \mathbf{R}'; \mathbf{s}) = \langle \delta(\mathbf{x} + \mathbf{r}_{G1}) \delta(\mathbf{x} + \mathbf{r}_{G2}) \rangle \langle \delta(\mathbf{x} + \mathbf{s} + \mathbf{r}'_{H2}) \delta(\mathbf{x} + \mathbf{s} + \mathbf{r}'_{H3}) \rangle \\ \times \langle \delta(\mathbf{x} + \mathbf{r}_0) \delta(\mathbf{x} + \mathbf{s} + \mathbf{r}'_{H1}) \rangle \langle \delta(\mathbf{x} + \mathbf{r}_{G3}) \delta(\mathbf{x} + \mathbf{s} + \mathbf{r}'_0) \rangle |_{r_0=r'_0=0}. \quad (\text{C15})$$

Naïvely, this case also involves an isotropic function of the form $\mathcal{P}_{0\ell\ell}$; however, the rotational average over the endpoint vectors forces their paired angular momenta to be zero.

Inserting our basic elements, we have:

$$I_{\text{III}}(\mathbf{R}, \mathbf{R}'; \mathbf{s}) = \sum_{G,H} (4\pi)^{3/2} \sum_{\ell_{G1}} f_{\ell_{G1} \ell_{G1} 0}(r_{G1}, r_{G2}, 0) (-1)^{\ell_{G1}} \sqrt{2\ell_{G1} + 1} \mathcal{P}_{\ell_{G1} \ell_{G1} 0}(\hat{\mathbf{r}}_{G1}, \hat{\mathbf{r}}_{G2}, 0) \\ \times (4\pi)^{3/2} \sum_{\ell'_{H1}} f_{\ell'_{H1} \ell'_{H1} 0}(r'_{H1}, r'_{H2}, 0) (-1)^{\ell'_{H1}} \sqrt{2\ell'_{H1} + 1} \mathcal{P}_{\ell'_{H1} \ell'_{H1} 0}(\hat{\mathbf{r}}'_{H1}, \hat{\mathbf{r}}'_{H2}, 0) \\ \times (4\pi)^{3/2} \sum_{\ell'_{H3}} f_{0 \ell'_{H3} \ell'_{H3}}(0, r'_{H3}, s) (-1)^{\ell'_{H3}} \sqrt{2\ell'_{H3} + 1} \mathcal{P}_{0 \ell'_{H3} \ell'_{H3}}(0, \hat{\mathbf{r}}'_{H3}, \mathbf{s}) \\ \times (4\pi)^{3/2} \sum_{\ell_{G3}} f_{0 \ell_{G3} \ell_{G3}}(0, r_{G3}, s) (-1)^{\ell_{G3}} \sqrt{2\ell_{G3} + 1} \mathcal{P}_{0 \ell_{G3} \ell_{G3}}(0, \hat{\mathbf{r}}_{G3}, \mathbf{s}). \quad (\text{C16})$$

In this case, the rotation average over $d\mathcal{R}$ will leave only the $\ell_{G3} = 0$ term since $\hat{\mathbf{r}}_{G1}$ and $\hat{\mathbf{r}}_{G2}$ are already combined into an isotropic function. Similarly, averaging over $d\mathcal{R}'$ will force $\ell'_{H3} = 0$, allowing us to simplify $\ell_{G1} \equiv \ell$ and $\ell'_{H1} \equiv \ell'$. Therefore, the two f -integrals associated with ℓ_{G3} and ℓ'_{H3} are given by

$$\int s^2 ds f_{000}(0, r_{G3}, s) f_{000}(0, r'_{H3}, s) = g_{0000}(0, r_{G3}, 0, r'_{H3}), \quad (\text{C17})$$

where we have used the identity for the integral of a product of two sBFs given in Eq. (C8). The final form of Case III reads:

$$\text{Cov}_{\Lambda, \Lambda'}^{(\text{pc}), \text{III}} = \sum_{G,H} \sum_{\mathcal{L}_G, \mathcal{L}'_H} \frac{(4\pi)^4}{V} (-1)^{\ell + \ell'} \sqrt{(2\ell + 1)(2\ell' + 1)} f_{\ell 0 0}(r_{G1}, r_{G2}, 0) f_{\ell' \ell' 0}(r'_{H1}, r'_{H2}, 0) g_{0000}(0, r_{G3}, 0, r'_{H3}) \mathcal{B}_{\mathcal{L}_G, \Lambda}^{G-1} \mathcal{B}_{\mathcal{L}'_H, \Lambda'}^{H-1} \quad (\text{C18})$$

Case IV Finally, consider the direct contraction between two primary vertices, accompanied by the contraction of two endpoints from each family

$$I_{IV}(\mathbf{R}, \mathbf{R}'; \mathbf{s}) = \langle \delta(\mathbf{x} + \mathbf{r}_0) \delta(\mathbf{x} + \mathbf{s} + \mathbf{r}'_0) \rangle |_{r_0=r'_0=0} \times \langle \delta(\mathbf{x} + \mathbf{r}_{G1}) \delta(\mathbf{x} + \mathbf{r}_{G2}) \rangle \langle \delta(\mathbf{x} + \mathbf{s} + \mathbf{r}'_{H2}) \delta(\mathbf{x} + \mathbf{s} + \mathbf{r}'_{H3}) \rangle \langle \delta(\mathbf{x} + \mathbf{r}_{G3}) \delta(\mathbf{x} + \mathbf{s} + \mathbf{r}'_{H1}) \rangle. \quad (\text{C19})$$

As before, inserting the basic elements leads to

$$I_{IV}(\mathbf{R}, \mathbf{R}'; \mathbf{s}) = \sum_{G,H} (4\pi)^{3/2} f_{000}(0, 0, s) \mathcal{P}_{000}(0, 0, \hat{\mathbf{s}}) \times (4\pi)^{3/2} \sum_{\ell_{G1}} (-1)^{\ell_{G1}} f_{\ell_{G1}\ell_{G1}0}(r_{G1}, r_{G2}, 0) \sqrt{2\ell_{G1} + 1} \mathcal{P}_{\ell_{G1}\ell_{G1}0}(\hat{\mathbf{r}}_{G1}, \hat{\mathbf{r}}_{G2}, 0) \times (4\pi)^{3/2} \sum_{\ell'_{H1}} (-1)^{\ell'_{H1}} f_{0\ell'_{H2}\ell'_{H2}}(0, r'_{H2}, r'_{H3}) \sqrt{2\ell'_{H2} + 1} \mathcal{P}_{0\ell'_{H2}\ell'_{H2}}(0, \hat{\mathbf{r}}'_{H2}, \hat{\mathbf{r}}'_{H3}) \times (4\pi)^{3/2} \sum_{\ell_{G3}\ell'_{H1}L_3} i^{-\ell_{G3} + \ell'_{H1} + L_3} f_{\ell_{G3}\ell'_{H1}L_3}(r_{G3}, r'_{H1}, s) \mathcal{D}_{\ell_{G3}\ell'_{H1}L_3}^{\text{P}} \mathcal{P}_{\ell_{G3}\ell'_{H1}L_3}(\hat{\mathbf{r}}_{G3}, \hat{\mathbf{r}}'_{H1}, \hat{\mathbf{s}}), \quad (\text{C20})$$

simplifying $\ell_{G1} \equiv \ell$ and $\ell'_{H2} \equiv \ell'$. We can see that the rotational average over $d\mathcal{S}$ forces $L_3 = 0$ and thus $\ell_{G3} = \ell'_{H1}$. Moreover, since $\hat{\mathbf{r}}_{G1}$ and $\hat{\mathbf{r}}_{G2}$ are already in an isotropic configuration in $\mathcal{P}_{\ell\ell 0}(\hat{\mathbf{r}}_{G1}, \hat{\mathbf{r}}_{G2}, \hat{\mathbf{r}}_{G3})$, the only allowed values of ℓ_{G3} and ℓ'_{H1} are zero. It follows that the isotropic functions reduce to constants: $\mathcal{P}_{\ell_{G3}\ell'_{H1}L_3}(\hat{\mathbf{r}}_{G3}, \hat{\mathbf{r}}'_{H1}, \hat{\mathbf{s}}) = (4\pi)^{-3/2}$ and $f_{\ell_{G3}\ell'_{H1}L_3}(r_{G3}, r'_{H1}, s) = f_{000}(r_{G3}, r'_{H1}, s)$. Integrating over s and using Eq. (C7) we find

$$\int s^2 ds f_{000}(0, 0, s) f_{000}(r_{G3}, r'_{H1}, s) = g_{0000}(0, 0, r_{G3}, r'_{H1}), \quad (\text{C21})$$

The final form of Case IV is given by

$$\text{Cov}_{\Lambda, \Lambda'}^{(\text{pc}), \text{IV}} = \sum_{G,H} \sum_{\mathcal{L}_G, \mathcal{L}'_H} \frac{(4\pi)^4}{V} (-1)^{\ell + \ell'} \sqrt{(2\ell + 1)(2\ell' + 1)} f_{\ell\ell 0}(r_{G1}, r_{G2}, 0) f_{0\ell'\ell'}(0, r'_{H2}, r'_{H3}) g_{0000}(0, 0, r_{G3}, r'_{H1}) \mathcal{B}_{\mathcal{L}_G, \Lambda}^{G-1} \mathcal{B}_{\mathcal{L}'_H, \Lambda'}^{H-1}. \quad (\text{C22})$$

APPENDIX D: ANALYTIC SOLUTION FOR INTEGRAL OF PRODUCT OF THREE SPHERICAL BESSEL FUNCTIONS

When radial binning is included, the f -integral is evaluated with the bin-averaged sBFs:

$$f_{\ell_1 \ell_2 \ell_3}(r_1, r_2, r_3) = \int \frac{k^2 dk}{2\pi^2} P(k) \bar{j}_{\ell_1}(k; r_1) \bar{j}_{\ell_2}(k; r_2) j_{\ell_3}(k; r_3), \quad (\text{D1})$$

where the bin-averaged sBFs are defined as:

$$\bar{j}_{\ell_i}(k; r_i) = \frac{\int r^2 dr j_{\ell_i}(kr_i) \Theta(r_i)}{\int r^2 dr \Theta(r_i)}. \quad (\text{D2})$$

Here $\Theta(r_i)$ is a binning function equal to unity within bin r_i and zero elsewhere.

In order to check the evaluation and implementation of the f -integral, we compare the numerical result to an analytic form with bin-averaged sBFs derived using Fabrikant (2013), Eq. (24):

$$I_e(p, q, m, n, \ell; a, b, c) = \int_0^\infty \exp(-pk) k^q j_m(ak) j_n(bk) j_\ell(ck) dk. \quad (\text{D3})$$

For this test, we make use of Eq. (26) in Fabrikant (2013), which provides an explicit solution for Eq. (D3) with $p = 1$, $q = 2$, and $m = n = \ell = 0$, and thus of $f_{000}(a, b, c)$, when the power spectrum is replaced by a power law damped by an exponential:

$$I_{\text{exp}}(1, 2, 0, 0, 0; a, b, c) = \frac{1}{4abc} \left(-T_{++++}^{abc} + T_{-+++}^{abc} + T_{+--+}^{abc} + T_{++--}^{abc} \right). \quad (\text{D4})$$

Here, we have introduced the notation that $T_{\pm\pm\pm\pm}^{abc} \equiv \tan^{-1}[(\pm a \pm b \pm c)/p]$. In practice the sBFs with arguments a and b are bin-averaged, and can be written as

$$\bar{j}_0(ak) = \frac{3}{k(a_{\text{max}}^3 - a_{\text{min}}^3)} [a_{\text{max}}^2 j_1(a_{\text{max}} k) - a_{\text{min}}^2 j_1(a_{\text{min}} k)], \quad (\text{D5})$$

where the recurrence relation (Rayleigh's formula) gives

$$j_1(xk) = -\frac{1}{k} \frac{d}{dx} j_0(xk) \quad (\text{D6})$$

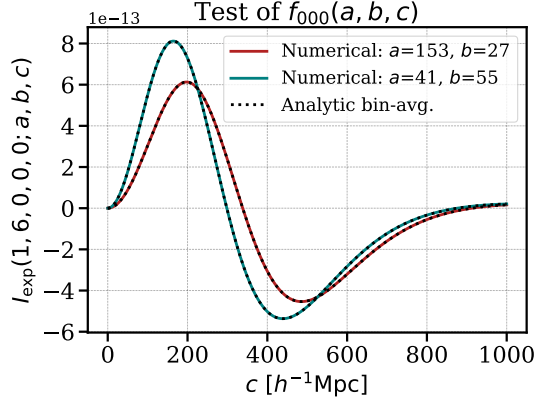


Figure D1. Comparison of the numerical and analytic implementations of the bin-averaged f -integral, setting $\ell_1 = \ell_2 = \ell_3 = 0$, and using a damped power-law power spectrum. We evaluate the integral at radial bin centers a and b as given in the legend, and their units are $h^{-1}\text{Mpc}$.

Replacing the sBF with the bin-averaged one given by Eq. (D5) and inserting the result into Eq. (D4) (setting $q = 6$ in order to use the analytic solution), we have

$$\begin{aligned}
& I_{\text{exp}}(1, 6, 0, 0, 0; a, b, c) \\
&= \int_0^\infty \exp(-k) k^6 \bar{j}_0(ak) \bar{j}_0(bk) j_0(ck) dk \\
&= \frac{3}{a_{\text{max}}^3 - a_{\text{min}}^3} \frac{3}{b_{\text{max}}^3 - b_{\text{min}}^3} \left[a_{\text{max}}^2 b_{\text{max}}^2 \frac{d}{da_{\text{max}}} \frac{d}{db_{\text{max}}} I_{\text{exp}}(1, 2, 0, 0, 0; a_{\text{max}}, b_{\text{max}}, c) \right. \\
&\quad - a_{\text{min}}^2 b_{\text{max}}^2 \frac{d}{da_{\text{min}}} \frac{d}{db_{\text{max}}} I_{\text{exp}}(1, 2, 0, 0, 0; a_{\text{min}}, b_{\text{max}}, c) \\
&\quad - a_{\text{max}}^2 b_{\text{min}}^2 \frac{d}{da_{\text{max}}} \frac{d}{db_{\text{min}}} I_{\text{exp}}(1, 2, 0, 0, 0; a_{\text{max}}, b_{\text{min}}, c) \\
&\quad \left. + a_{\text{min}}^2 b_{\text{min}}^2 \frac{d}{da_{\text{min}}} \frac{d}{db_{\text{min}}} I_{\text{exp}}(1, 2, 0, 0, 0; a_{\text{min}}, b_{\text{min}}, c) \right]. \tag{D7}
\end{aligned}$$

In the above equation we obtain four types of terms, differing by their lower or upper bounds in a or b . Next, we focus on the general form $\frac{d}{da} \frac{d}{db} I_{\text{exp}}(\dots)$:

$$\frac{d}{da} \frac{d}{db} I_{\text{exp}}(\dots) = \frac{d}{da} \frac{d}{db} \left[\frac{1}{4abc} \left(-T_{++++}^{abc} + T_{-+++}^{abc} + T_{+--+}^{abc} + T_{+---}^{abc} \right) \right]. \tag{D8}$$

Due to the symmetry of these expressions, in what follows we may focus on just the first term T_{++++}^{abc} .

$$\begin{aligned}
& \frac{d}{da} \frac{d}{db} \left(\frac{1}{4abc} T_{++++}^{abc} \right) \\
&= \frac{d}{da} \frac{d}{db} \left(\frac{1}{4abc} \tan^{-1}[(c+b+a)/p] \right) \\
&= \frac{1}{4a^2 b^2 c} \left(\tan^{-1}[(c+b+a)/p] - \frac{a+b}{p} \frac{1}{(a+b+c)^2/p^2 + 1} - \frac{ab}{p^3} \frac{2(a+b+c)}{((a+b+c)^2/p^2 + 1)^2} \right), \tag{D9}
\end{aligned}$$

This form remains the same for the rest of the $T_{\pm\pm\pm\pm}^{abc}$ terms, except for the signs. Inserting Eq. (D9) into Eq. (D7) we obtain the final result shown in Fig. D1 (dotted black curves) after integrating over c . As an example, we evaluate the integral for two cases $a = 153 h^{-1}\text{Mpc}$, $b = 27 h^{-1}\text{Mpc}$ and $a = 41 h^{-1}\text{Mpc}$, $b = 55 h^{-1}\text{Mpc}$. In both cases the numerical implementation and the analytic solution display excellent agreement.

APPENDIX E: GAUSSIAN NPCF COVARIANCES INCLUDING RSD

Here we extend our general expression for the real-space covariance to include RSD. As a preparation for the derivation, we extend the \mathcal{Q} quantity to involve four angular momenta:

$$\mathcal{Q}^{\Lambda\Lambda'\Lambda''\Lambda'''} = \prod_{i=1}^N \sum_{m_i m'_i M_i \mu_i} C_{m_i m'_i M_i \mu_i}^{\ell_i \ell'_i L_i \lambda_i} C_M^\Lambda C_{M'}^{\Lambda'} C_{M''}^{\Lambda''} C_{M'''}^{\Lambda'''}, \tag{E1}$$

where the C_M^A coefficient is defined in Eq. (2) with

$$\mathcal{H}^{\Lambda\Lambda'\Lambda''\Lambda'''} = (4\pi)^{-N/2} \left[\prod_{i=1}^N \mathcal{D}_{\ell_i \ell'_i \ell''_i \ell'''_i}^P \mathcal{C}_{0000}^{\ell_i \ell'_i \ell''_i \ell'''_i} \right] \mathcal{Q}^{\Lambda\Lambda'\Lambda''\Lambda'''}. \quad (\text{E2})$$

Furthermore, averaging over isotropic functions of four arguments gives

$$\begin{aligned} & \int d\mathcal{R} d\mathcal{R}' d\mathcal{S} d\mathcal{N} \prod_{i=1}^N \mathcal{P}_{\ell_i \ell'_i \ell''_i \ell'''_i \lambda_i}(\hat{\mathbf{r}}_i, \hat{\mathbf{r}}'_i, \hat{\mathbf{s}}, \hat{\mathbf{n}}) \\ &= (4\pi)^{-N} \sum_{\mathcal{L}\mathcal{L}'\Lambda''\Lambda'''} \mathcal{Q}^{\mathcal{L}\mathcal{L}'\Lambda''\Lambda'''} \mathcal{D}_{\Lambda''}^P \mathcal{C}_0^{\Lambda''} \mathcal{D}_{\Lambda'''}^P \mathcal{C}_0^{\Lambda'''} \mathcal{P}_{\mathcal{L}}(\hat{\mathbf{R}}^{(N)}) \mathcal{P}_{\mathcal{L}'}(\hat{\mathbf{R}}'^{(N)}). \end{aligned} \quad (\text{E3})$$

For the fully-coupled covariance including RSD we start from Eq. (33) and Eq. (B11):

$$\begin{aligned} & \sum_{\Lambda, \Lambda'} \mathcal{E}(\Lambda') \text{Cov}_{\Lambda, \Lambda'}(R, R') \mathcal{P}_{\Lambda}(\hat{\mathbf{R}}) \mathcal{P}_{\Lambda'}(\hat{\mathbf{R}}') \\ &= \int \frac{d^3 \mathbf{s}}{V} (4\pi)^{2N} \sum_G \prod_{i=0}^{N-1} \sum_{\ell_{G_i} \ell'_i \ell''_i \ell'''_i} \frac{1}{2\lambda_i + 1} i^{-\ell_{G_i} + \ell'_i + L_i} \\ & \quad \times \mathcal{D}_{\ell_{G_i} \ell'_i \ell''_i \ell'''_i}^P \mathcal{C}_{0000}^{\ell_{G_i} \ell'_i \ell''_i \ell'''_i} \int_{\ell_{G_i} \ell'_i \ell''_i \ell'''_i}^{\lambda_i} (r_{G_i}, r'_i, s) \mathcal{P}_{\ell_{G_i} \ell'_i \ell''_i \ell'''_i}(\hat{\mathbf{r}}_{G_i}, \hat{\mathbf{r}}'_i, \hat{\mathbf{s}}, \hat{\mathbf{n}}) |_{r_0=r'_0=0}. \end{aligned} \quad (\text{E4})$$

Next, we apply the rotational average over $\hat{\mathbf{r}}$, $\hat{\mathbf{r}}'$, $\hat{\mathbf{s}}$, and $\hat{\mathbf{n}}$ ¹⁴:

$$\begin{aligned} & \sum_{\Lambda, \Lambda'} \mathcal{E}(\Lambda') \text{Cov}_{\Lambda, \Lambda'}(R, R') \mathcal{P}_{\Lambda}(\hat{\mathbf{R}}) \mathcal{P}_{\Lambda'}(\hat{\mathbf{R}}') \\ &= \int \frac{s^2 ds}{V} (4\pi)^{3N/2} \sum_G \prod_{i=0}^{N-1} \sum_{\ell_{G_i} \ell'_i \ell''_i \ell'''_i} \frac{1}{2\lambda_i + 1} i^{-\ell_{G_i} + \ell'_i + L_i} \mathcal{H}^{\mathcal{L}_G \mathcal{L}' \Lambda'' \Lambda'''} \\ & \quad \times \int_{\ell_{G_i} \ell'_i \ell''_i \ell'''_i}^{\lambda_i} (r_{G_i}, r'_i, s) \mathcal{D}_{\Lambda''}^P \mathcal{C}_0^{\Lambda''} \mathcal{D}_{\Lambda'''}^P \mathcal{C}_0^{\Lambda'''} \mathcal{P}_{\mathcal{L}_G}(\hat{\mathbf{R}}_G^{(N)}) \mathcal{P}_{\mathcal{L}'}(\hat{\mathbf{R}}'^{(N)}) |_{r_0=r'_0=0}; \end{aligned} \quad (\text{E5})$$

as before, going from $\hat{\mathbf{R}}_G^{(N)} \rightarrow \hat{\mathbf{R}}_G$ leads to a factor of $(4\pi)^{-1/2}$, which is cancelled with the normalization factor arising from $d\mathcal{S}$. Next, we use the reordering coefficient to restore the canonical ordering of the arguments, and project both sides onto the isotropic basis $\mathcal{P}_{\Lambda}(\hat{\mathbf{R}})$ and $\mathcal{P}_{\Lambda'}(\hat{\mathbf{R}}')$. This yields the final form:

$$\begin{aligned} & \text{Cov}_{\Lambda, \Lambda'}(R, R') \\ &= (4\pi)^{3N/2} \int \frac{s^2 ds}{V} \sum_G \sum_{\mathcal{L}_G \Lambda'' \Lambda'''} \prod_{i=0}^{N-1} \left[\frac{1}{2\lambda_i + 1} \int_{\ell_{G_i} \ell'_i \ell''_i \ell'''_i}^{\lambda_i} (r_{G_i}, r'_i, s) \right] (-1)^{[-\Sigma(\Lambda) - \Sigma(\Lambda') + \Sigma(\Lambda'')]/2} \\ & \quad \times \mathcal{B}_{\mathcal{L}_G, \Lambda}^{G-1} \mathcal{H}^{\mathcal{L}_G \Lambda'' \Lambda'''} \mathcal{D}_{\Lambda''}^P \mathcal{C}_0^{\Lambda''} \mathcal{D}_{\Lambda'''}^P \mathcal{C}_0^{\Lambda'''} |_{r_{G0}=r'_{0}=0}. \end{aligned} \quad (\text{E6})$$

REFERENCES

- Adams J. C., 1878, Proceedings of the Royal Society of London Series I, 27, 63
 Agarwal N., Desjacques V., Jeong D., Schmidt F., 2021, *J. Cosmology Astropart. Phys.*, 2021, 021
 Alam S., et al., 2015, *The Astrophysical Journal Supplement Series*, 219, 12
 Alam S., et al., 2020, arXiv e-prints, p. arXiv:2011.05771
 Amendola L., et al., 2018, *Living Reviews in Relativity*, 21, 2
 Anderson T., 2009, An Introduction to Multivariate Statistical Analysis, 3rd Ed.. Wiley India Pvt. Limited, <https://books.google.com/books?id=1iFOCgAAQBAJ>
 Aviles A., Banerjee A., Niz G., Slepian Z., 2021, Clustering in Massive Neutrino Cosmologies via Eulerian Perturbation Theory (arXiv:2106.13771)
 BOSS Collaboration et al., 2017, *MNRAS*, 470, 2617
 Barreira A., 2019, *Journal of Cosmology and Astroparticle Physics*, 2019, 008–008
 Bartolo N., Bellini E., Bertacca D., Matarrese S., 2013, *J. Cosmology Astropart. Phys.*, 2013, 034
 Baumann D., Nicolis A., Senatore L., Zaldarriaga M., 2012, *Journal of Cosmology and Astroparticle Physics*, 2012, 051–051
 Cahn R. N., Slepian Z., 2020, Isotropic N -Point Basis Functions and Their Properties (arXiv:2010.14418)
 Carrasco J. J. M., Hertzberg M. P., Senatore L., 2012, *Journal of High Energy Physics*, 2012
 Chen X., 2010, *Advances in Astronomy*, 2010, 1–43
 Chen X., Huang M.-x., Kachru S., Shiu G., 2007, *Journal of Cosmology and Astroparticle Physics*, 2007, 002–002
 Chiang C.-T., Wagner C., Schmidt F., Komatsu E., 2014, *Journal of Cosmology and Astroparticle Physics*, 2014, 048–048
 Chudaykin A., Ivanov M. M., 2019, *J. Cosmology Astropart. Phys.*, 2019, 034
 Chudaykin A., Ivanov M. M., Philcox O. H., Simonović M., 2020, *Physical Review D*, 102

¹⁴ The rotational average over $\hat{\mathbf{n}}$ is justified as the isotropic 4PCF must be invariant under rotations.

- DESI Collaboration et al., 2016, arXiv e-prints, p. [arXiv:1611.00036](https://arxiv.org/abs/1611.00036)
- DLMF, *NIST Digital Library of Mathematical Functions*. <http://dlmf.nist.gov/>
- Dawson K. S., et al., 2013, *AJ*, **145**, 10
- Deadman E., Higham N. J., Ralha R., 2013, in Manninen P., Öster P., eds, Applied Parallel and Scientific Computing. Springer Berlin Heidelberg, Berlin, Heidelberg, pp 171–182
- Dizgah A. M., Lee H., Schmittfull M., Dvorkin C., 2020, *Journal of Cosmology and Astroparticle Physics*, 2020, 011–011
- Dodelson S., Schneider M. D., 2013, *Physical Review D*, 88
- Eisenstein D. J., Seo H.-J., Sirko E., Spergel D. N., 2007, *ApJ*, **664**, 675
- Fabrikant V. I., 2013, *Quarterly of Applied Mathematics*, **71**, 573
- Feldman H. A., Kaiser N., Peacock J. A., 1994, *ApJ*, **426**, 23
- Fry J. N., Gaztanaga E., 1993, *ApJ*, **413**, 447
- Gil-Marín H., Percival W. J., Verde L., Brownstein J. R., Chuang C.-H., Kitaura F.-S., Rodríguez-Torres S. A., Olmstead M. D., 2017, *MNRAS*, **465**, 1757
- Grieb J. N., Sánchez A. G., Salazar-Albornoz S., Dalla Vecchia C., 2016, *Monthly Notices of the Royal Astronomical Society*, **457**, 1577–1592
- Gualdi D., Gil-Marín H., Verde L., 2021, arXiv e-prints, p. [arXiv:2104.03976](https://arxiv.org/abs/2104.03976)
- Hahn C., Villaescusa-Navarro F., Castorina E., Scoccimarro R., 2020, *J. Cosmology Astropart. Phys.*, 2020, 040
- Hand N., Feng Y., Beutler F., Li Y., Modi C., Seljak U., Slepian Z., 2018, *The Astronomical Journal*, **156**, 160
- Ivanov M. M., Simonović M., Zaldarriaga M., 2020, *Journal of Cosmology and Astroparticle Physics*, 2020, 042–042
- Jasche J., Lavaux G., 2019, *A&A*, **625**, A64
- Jasche J., Wandelt B. D., 2013, *Monthly Notices of the Royal Astronomical Society*, **432**, 894–913
- Kaiser N., 1987, *MNRAS*, **227**, 1
- Kamalinejad F., Slepian Z., 2020, A Non-Degenerate Neutrino Mass Signature in the Galaxy Bispectrum ([arXiv:2011.00899](https://arxiv.org/abs/2011.00899))
- Kitaura F.-S., et al., 2016, *MNRAS*, **456**, 4156
- Kofman L., 1991, *Physica Scripta Volume T*, **36**, 108
- Komatsu E., et al., 2003, *The Astrophysical Journal Supplement Series*, **148**, 119–134
- Kullback S., Leibler R. A., 1951, *The Annals of Mathematical Statistics*, **22**, 79
- LSST Science Collaboration et al., 2009, LSST Science Book, Version 2.0 ([arXiv:0912.0201](https://arxiv.org/abs/0912.0201))
- Laureijs R., et al., 2011, arXiv e-prints, p. [arXiv:1110.3193](https://arxiv.org/abs/1110.3193)
- Li Y., Singh S., Yu B., Feng Y., Seljak U., 2019, *J. Cosmology Astropart. Phys.*, 2019, 016
- Linde A., Mukhanov V., 1997, *Physical Review D*, **56**, R535–R539
- Massara E., Villaescusa-Navarro F., Ho S., Dalal N., Spergel D. N., 2021, *Phys. Rev. Lett.*, **126**, 011301
- Mehrem R., Londergan J. T., Macfarlane M. H., 1991, *Journal of Physics A Mathematical General*, **24**, 1435
- O’Connell R., Eisenstein D. J., 2019, *MNRAS*, **487**, 2701
- O’Connell R., Eisenstein D., Vargas M., Ho S., Padmanabhan N., 2016, *MNRAS*, **462**, 2681
- O’Connell R., Eisenstein D., Vargas M., Ho S., Padmanabhan N., 2016, *Monthly Notices of the Royal Astronomical Society*, **462**, 2681–2694
- Padmanabhan N., White M., Cohn J. D., 2009, *Phys. Rev. D*, **79**, 063523
- Pearson D. W., Samushia L., 2018, *MNRAS*, **478**, 4500
- Peebles P. J. E., 1978, in Longair M. S., Einasto J., eds, Vol. 79, Large Scale Structures in the Universe. p. 217
- Percival W. J., et al., 2014, *MNRAS*, **439**, 2531
- Philcox O. H. E., Eisenstein D. J., 2019, *Monthly Notices of the Royal Astronomical Society*, **490**, 5931–5951
- Philcox O. H. E., Slepian Z., 2021, Efficient Computation of N-point Correlation Functions in D Dimensions ([arXiv:2106.10278](https://arxiv.org/abs/2106.10278))
- Philcox O. H. E., Eisenstein D. J., O’Connell R., Wiegand A., 2019, *Monthly Notices of the Royal Astronomical Society*, **491**, 3290–3317
- Philcox O. H. E., Massara E., Spergel D. N., 2020a, *Phys. Rev. D*, **102**, 043516
- Philcox O. H. E., Eisenstein D. J., O’Connell R., Wiegand A., 2020b, *MNRAS*, **491**, 3290
- Philcox O. H. E., Hou J., Slepian Z., Cahn R. N., Eisenstein D. J., 2021b, 4PCF BOSS
- Philcox O. H. E., Slepian Z., Hou J., Warner C., Cahn R. N., Eisenstein D. J., 2021a, encore: Estimating Galaxy N-point Correlation Functions in $O(N^2)$ Time
- Philcox O. H. E., Ivanov M. M., Zaldarriaga M., Simonović M., Schmittfull M., 2021c, *Phys. Rev. D*, **103**, 043508
- Portillo S. K. N., Slepian Z., Burkhart B., Kahraman S., Finkbeiner D. P., 2018, *ApJ*, **862**, 119
- Putter R. d., Wagner C., Mena O., Verde L., Percival W. J., 2012, *Journal of Cosmology and Astroparticle Physics*, 2012, 019–019
- Rodríguez-Torres S. A., et al., 2016, *Monthly Notices of the Royal Astronomical Society*, **460**, 1173–1187
- Ruggeri R., Castorina E., Carbone C., Sefusatti E., 2018, *Journal of Cosmology and Astroparticle Physics*, 2018, 003–003
- Samushia L., Slepian Z., Villaescusa-Navarro F., 2021, arXiv e-prints, p. [arXiv:2102.01696](https://arxiv.org/abs/2102.01696)
- Schmidt F., Elsner F., Jasche J., Nguyen N. M., Lavaux G., 2019, *Journal of Cosmology and Astroparticle Physics*, 2019, 042–042
- Schmittfull M., Dizgah A. M., 2021, *Journal of Cosmology and Astroparticle Physics*, 2021, 020
- Schmittfull M., Feng Y., Beutler F., Sherwin B., Chu M. Y., 2015, *Phys. Rev. D*, **92**, 123522
- Schmittfull M., Baldauf T., Zaldarriaga M., 2017, *Phys. Rev. D*, **96**, 023505
- Schneider P., Bartelmann M., 1995, *MNRAS*, **273**, 475
- Scoccimarro R., 2000, *ApJ*, **544**, 597
- Scoccimarro R., Colombi S., Fry J. N., Frieman J. A., Hivon E., Melott A., 1998, *ApJ*, **496**, 586
- Scoccimarro R., Zaldarriaga M., Hui L., 1999, *The Astrophysical Journal*, **527**, 1–15
- Sefusatti E., Scoccimarro R., 2005, *Phys. Rev. D*, **71**, 063001
- Seljak U., Aslanyan G., Feng Y., Modi C., 2017, *J. Cosmology Astropart. Phys.*, 2017, 009
- Sellentin E., Heavens A. F., 2016, *MNRAS*, **456**, L132
- Senatore L., 2015, *Journal of Cosmology and Astroparticle Physics*, 2015, 007–007
- Senatore L., Zaldarriaga M., 2014, Redshift Space Distortions in the Effective Field Theory of Large Scale Structures ([arXiv:1409.1225](https://arxiv.org/abs/1409.1225))
- Slepian Z., Eisenstein D. J., 2015a, *Monthly Notices of the Royal Astronomical Society*, **454**, 4142–4158

- Slepian Z., Eisenstein D. J., 2015b, [Monthly Notices of the Royal Astronomical Society: Letters](#), 455, L31–L35
- Slepian Z., Eisenstein D. J., 2018, [Monthly Notices of the Royal Astronomical Society](#), 478, 1468–1483
- Slepian Z., et al., 2017, [Monthly Notices of the Royal Astronomical Society](#), 468, 1070–1083
- Sugiyama N. S., Saito S., Beutler F., Seo H.-J., 2020a, [MNRAS](#), 497, 1684
- Sugiyama N. S., Saito S., Beutler F., Seo H.-J., 2020b, [Monthly Notices of the Royal Astronomical Society](#), 501, 2862–2896
- Taylor A., Joachimi B., 2014, [Monthly Notices of the Royal Astronomical Society](#), 442, 2728–2738
- Taylor A., Joachimi B., Kitching T., 2013, [Monthly Notices of the Royal Astronomical Society](#), 432, 1928–1946
- Villaescusa-Navarro F., et al., 2020, [ApJS](#), 250, 2
- Wadekar D., Ivanov M. M., Scoccimarro R., 2020, [Physical Review D](#), 102
- White M., 2015, [MNRAS](#), 450, 3822
- Wishart J., 1928, *Biometrika*, 20A, 32
- de Belsunce R., Senatore L., 2019, [Journal of Cosmology and Astroparticle Physics](#), 2019, 038–038
- eBOSS Collaboration et al., 2021, [Phys. Rev. D](#), 103, 083533